TU WIEN

DISSERTATION

Experimental Investigation of Free Surface Oscillation in the Draft Tube of Hydraulic Machines

carried out for the purpose of obtaining the degree of
Doctor technicae (Dr.techn.),
submitted at TU Wien, Faculty of Mechanical and Industrial Engineering,
by

Dipl.-Ing. Anton Maly BSc
Matr.Nr. 0728033

under the supervision of

Univ.Prof. Dipl.-Ing. Dr.-Ing. Christian Bauer
Ass.Prof. Dipl.-Ing. Dr.techn. Klaus Käfer
Institute of Energy Systems and Thermodynamics
Research Unit of Fluid Flow Machinery

Vienna, October 22, 2019

reviewed by

Ao.Univ.Prof.Dipl.-Ing.Dr.techn.	Ao.Univ.Prof.Dipl.-Ing.Dr.techn.
Reinhard Willinger	Reinhard Prenner
Institute of Energy Systems and Thermodynamics	Institute of Hydraulic Engineering and Water Resources Management

Danksagung

An erster Stelle möchte ich mich bei meinen Betreuern Herrn Univ.Prof. Dipl.-Ing. Dr.-Ing Christian Bauer und Ass.Prof. Dipl.-Ing. Dr.techn. Klaus Käfer bedanken, welche immer ein offenes Ohr, sowie Ratschläge und auch das eine oder andere ermutigende Wort für mich hatten, wenn es nötig war.

Des Weiteren möchte ich mich bei Ao.Univ.Prof.Dipl.-Ing.Dr.techn. Reinhard Willinger und Ao.Univ.Prof.Dipl.-Ing.Dr.techn. Reinhard Prenner für das Interesse an meiner Arbeit und die Begutachtung bedanken.

Danke auch an meine Kollegen in der Werkstätte für die handwerkliche Unterstützung und an alle Kollegen im Assistentenzimmer und generell am Getreidemarkt - für alle konstruktiven oder Gedanken zerstreuenden Gespräche und Diskussionen.

Zu guter Letzt gebührt mein Dank meinen Eltern, meiner Schwester und meiner ganzen Familie - Ihr habt immer an mich geglaubt und mich stets unterstützt. Danke **auch an dich liebe** Kerstin und danke an unsere Tochter, euch ist beiden nicht bewusst wie oft Ihr mich zum Schmunzeln bringt oder mir einfach durch eure Anwesenheit Kraft gegeben habt. Danke, dass Ihr mit mir durchs Leben geht.

Kurzfassung

Die Aufgaben und Anforderungen an Kraftwerke und das Stromnetz ändern sich. Der Stromkonsum steigt stetig und die sogenannten "neuen" erneuerbaren Energiequellen, welche starken Fluktuationen unterliegen, gewinnen immer mehr an Bedeutung. Es wird prognostiziert, dass dieser Trend langfristig anhält. Daher werden ein hoher Grad an Flexibilität und die Gewährleistung der Versorgungssicherheit Hauptanforderungen an Kraftwerke und das gesamte Versorgungssystem sein.Schon jetzt werden Wasserkraftwerke zur Netzstabilisierung herangezogen. Aufgrund der genannten Entwicklungen wird von einem steigenden Bedarf an diesen Netzdienstleistungen ausgegangen. Eine dieser Regelaufgaben ist die Blindleistungskompensation und Regulierung des Phasenwinkels. Hierfür werden Wasser- kraftwerke mit Synchronmaschinen im sogenannten Phasenschieber-Betrieb betrieben. Dabei wird das Wasser aus dem Laufrad entfernt und es rotiert in Luft über einer freien Wasseroberfläche. Derselbe Zustand ergibt sich, wenn die Maschine im Standby betrieben wird oder beim Anfahrvorgang im Pumpenbetrieb. Während diesem Betriebszustand kann es zur Anregung einer Oszillation an der freien Wasseroberfläche im Saugrohrkonus kommen. Die vorliegende Arbeit beschäftigt sich mit der experimentellen Erforschung dieses Phänomens.

Im Zuge dieser Arbeit wurden Modellversuche im hydraulischen Labor des Instituts für Energietechnik und Thermodynamik an der TU Wien durchgeführt. Die untersuchte Modell-Pumpturbine ist mit einem Acrylglaskonus ausgerüstet. Dadurch bietet sich die Möglichkeit für optische Betrachtungen und Untersuchungen im Saugrohrkonus. Zusätzlich zur Standardinstrumentierung sind hochfrequente Drucksensoren an unterschiedlichen Messebenen und -stellen installiert. Die Untersuchungen erfolgen für beide Laufraddrehrichtungen, verschiedene Wasserniveaus im Saugrohr und unterschiedliche densimetrische Froudezahlen.

Zur Bestimmung der Amplitude werden Hochgeschwindigkeits-Kameraaufnahmen durchgeführt und die Aufnahmen analysiert. Die Frequenz der Oberflächenoszillation im eingeschwungenen Zustand wird mittels der Drucksignale und FFT detektiert. Die gemessenen Daten ermöglichen die Feststellung von generellen Trends, Abhängigkeiten sowie Einflussfaktoren auf die Bewegung der freien Wasseroberfläche. Des Weiteren wird die Oberflächenoszillation qualitativ beschrieben und Vergleichsmessungen an einem zweiten Konus getätigt. Im letzten Kapitel wird ein analytisches Modell zur Beschreibung der Winkelgeschwindigkeiten und Frequenzen präsentiert. Es separiert die einzelnen Vorgänge und gibt die Abhängigkeiten sowie das Verhalten qualitativ wieder.

Abstract

Driven by policy, environment protection aspects and to ensure the security of supply the requirements on the power plants and the power grid are changing. On the one hand electricity consumption is always growing and on the other hand so called new renewable energy sources are used as electricity source for an increasing amount. This trend is predicted to continue. Due to these facts, flexibility and ensuring the security of supply will be main requirements on power plants and the electricity system.

Hydro power plants already provide balancing services to the power grid and the amount is expected to increase in the near future. One service is the compensation of reactive power. Therefore, hydro power units equipped with synchronous machines are operated in so called synchronous condenser mode. Hence the runner is dewatered and rotates in air above a free surface. Similar conditions occur, if the machine is operated in standby or during pump start up procedure.

With runner rotating in air above the depressed water at the draft tube, a free surface oscillation is excited under some conditions. This thesis deals with the experimental investigation of this flow phenomenon.

Therefore, model tests are executed at the hydraulic laboratory of the Institute of Energy Systems and Thermodynamics at TU Wien. Investigated model pump-turbine is equipped with a draft tube cone made of acrylic glass for optical investigations. Fast response pressure transducers are installed at different planes and positions in addition to the standard instrumentation. The machine setup and measurement conditions aim on the investigation of the free surface oscillation and shall prevent other influences.

The experiments are performed for both runner rotation directions, for different initial water levels at the draft tube and different densimetric Froude numbers. High speed camera recordings are conducted and the amplitude of the water formation is determined by post processing the captured data. The frequency of the free surface oscillation in periodic state is extracted out of the pressure signals. Hence general trends and dependencies are identified by means of the acquired data. Furthermore, the behaviour of the free surface oscillation at the draft tube is described in a qualitative way and comparative experiments are performed with a second draft tube cone made of steel.

An analytical approach is presented in the last chapter, describing the angular velocity and frequency of the free surface oscillation. It aims at the separation of the single processes and representing the qualitative behaviour and dependencies.

Contents

Nomenclature

Acronyms

Symbol	Description	Unit
ADC	Analog digital converter	-
CMOS	complementary metal–oxide–semiconductor	-
DSF	Demand Side Flexibility	-
DT	draft tube cone	-
DTFoot	draft tube foot	-
OECD	Organisation for Economic Co-operation and Development	-
fps	frames per second	-
FFT	Fast Fourier Transformation	-
FSO	free surface oscillation	-
IET	Institute of Energy systems and Thermodynamics	-
LDA	Laser Doppler Anemometry	-
PLEF	Pentalateral Energy Forum	-
PIV	Particle Image Velocimetry	-
prim	priming chamber / vaneless space	-
Pt	Platin	-
PV	Photovoltaic	-
RES	Renewable energy sources	-
ROI	region of interest	-
rpm	revolutions per minute	-
SC	spiral case	-
SiC	runner side chamber	-
TR	tailrace	-
S.I.	International system of units - in French: Système international (d'unités)	-

Latin characters

Symbol	Description	Unit
A	Amplitude of free surface oscillation	m
A_{pp}	Peak to peak amplitude of free surface oscillation	m
c	velocity of free surface	$\mathrm{m\,s^{-1}}$
c_F	friction coefficient	-
c_T	torque coefficient	-
C	characteristic velocity	$\mathrm{m\,s^{-1}}$
D_1	diameter of runner high pressure side	m
D_2	diameter of runner low pressure side	m
E	specific energy	$\mathrm{J\,kg^{-1}}$
Ek	Ekman number	-
e_r	random measurement error	
e_s	systematic measurement error	
$e_{s,k}$	known systematic measurement error	
$e_{s,u}$	unknown systematic measurement error	
f	frequency	Hz
Fd	densimetric Froude number	-
Fr	Froude number	-
g	gravity constant	$\mathrm{m\,s^{-2}}$
H	head	m
h_1	height of rotationally axis symmetric draft tube part	m
h_2	total height of draft tube	m
L	characteristic geometrical parameter	m
Ma	Mach number	-
n	runner speed	$\mathrm{s^{-1}}$
n	number of measured values	-
n_q	specific speed	rpm
N_{QE}	speed factor according IEC 60193	-
$NPSH$	net positive suction head	m
P	real power	W
Q	discharge	$\mathrm{m^3\,s^{-1}}$
Q	reactive power	V A
r	radius	m
Re	Reynolds number	-
S	apparent power	V A
T	periodic time	s
T	shaft torque	N m
T	temperature	K
t_i	timestamp	s
u	circumferential velocity	$\mathrm{m\,s^{-1}}$

U	circumferential velocity of disc	m s^{-1}
u_2	circumferential velocity at runner low pressure side	m s^{-1}
u_r	random measurement uncertainty	
u_s	systematic measurement uncertainty	
v	propagation velocity of plane wave	m s^{-1}
w	relative velocity of excited water mass	m s^{-1}
X	measurement quantity	
x	measurement value	
x_E	corrected measurement value	
x_t	true value	
Y	target value	
z	z-coordinate	m

Greek characters

Symbol	Description	Unit
γ	specific heat ratio	-
κ	z-coordinate normalized by diameter of runner low pressure side	-
λ	wavelength	m
μ	expected value	
ν	kinematic viscosity	$\text{m}^2\,\text{s}^{-1}$
ϕ	phase angle	rad
φ	polar angle	°
ρ	density	kg m^{-3}
τ	time-constant	s
θ	opening angle of draft tube	°
ω	angular frequency	rad s^{-1}
Ω	angular velocity	rad s^{-1}

Subscript characters

Symbol	Description	Unit
A	air flow	-
f	fluid	-
fs	free surface	-
FSO	free surface oscillation	-
$crit$	critical value	-
ini	initial value	-
px	pixel	-
R	runner	-
max	maximum value	-
W	water flow	-

CHAPTER 1

Introduction

This chapter provides a brief overview of current trends in the energy market both globally and in the European Union. Arising challenges are discussed and the current situation on the electricity generation is explained. Furthermore, a short overview of the main components of a hydro power machine unit is given. The last section deals with the research objectives of this thesis.

1.1   Energy supply

World wide electricity demand and consequently electricity generation is continuously increasing in the last decades. In 2016 generated electricity reaches an amount of 25 million GWh, more than a half produced by thermal power plants primary using coal and gas. The third largest electricity source is hydro power - supplying more than 15% of electricity generation as illustrated in Figure 1.1. Furthermore, hydro power is the leading renewable energy source (RES) world wide as depicted in Figure 1.2. The trend of electricity generation from renewables in OECD-countries shows an increasing amount of electricity generated by wind power in the last 20 years. In the OECD-trend about 23% of electricity is generated by wind and solar photovoltaic. In the European Union more than a half of electricity generation from RES is supplied by wind and solar photovoltaic in 2016. However, in EU-28 only 25% of electricity is generated by renewable energy sources. [29]
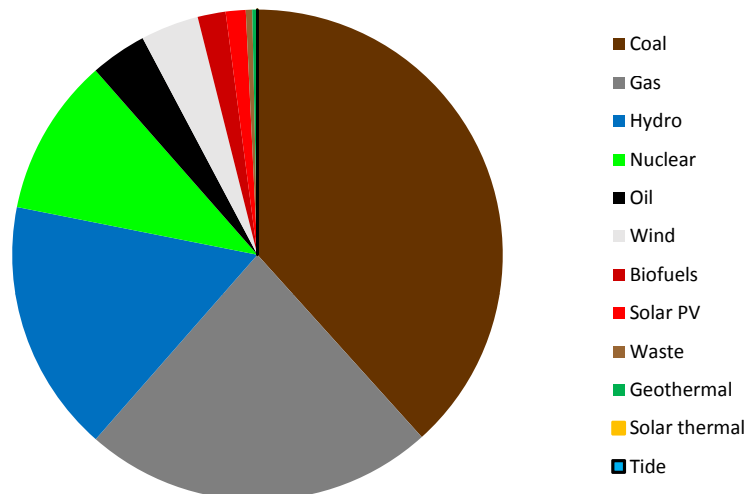

Figure 1.1: Electricity generation in OECD countries in the year 2016; data from [29]

Till 2050 the European Union aims to reduce greenhouse gas emission by 80-95% referencing to the level of 1990. Electricity supply plays an increasing role in achieving this ambitious goal. This leads to a doubling of the share of electricity in final energy demand up to 39%, even taking high efficiency scenarios as a basis. As a result the power system is forced to undergo structural changes with high needs for balancing capacity, storage and grid investments. Some scenarios expect wind power to generate more electricity than any other technology in the European Union by 2050. Due to increasing contribution of intermittent renewable energy sources - flexible generation, storage and a well developed demand management is needed more than ever before. [20]
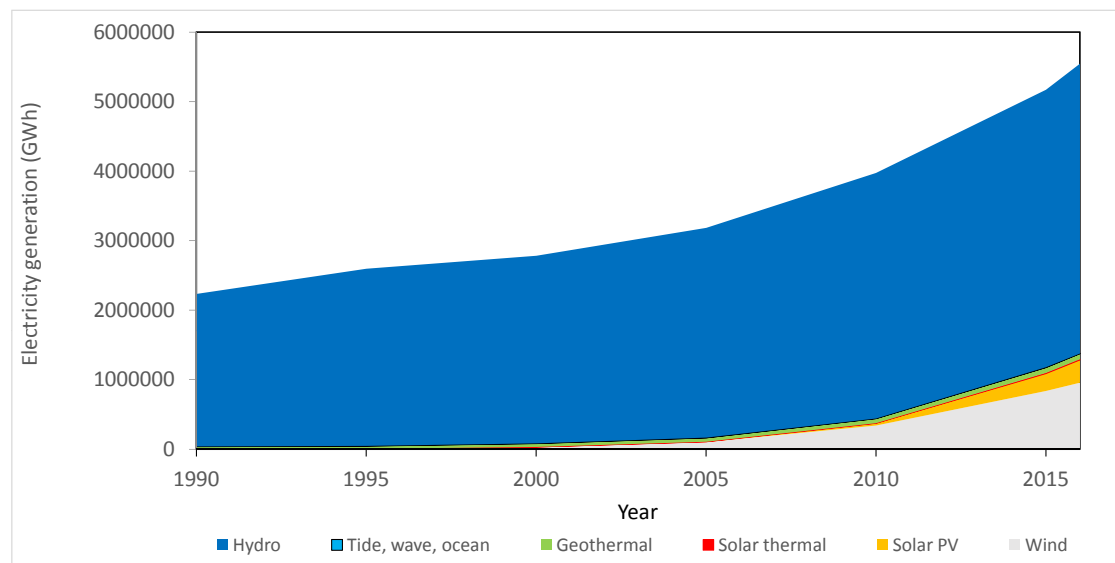
Figure 1.2: Mix of renewable energy sources in OECD countries till 2016; data from [29]

Instead of generated electricity the installed capacity is decisive for considerations regarding energy supply and power grid. For example, a wind park in Austria generates the same amount of GWh per year as a run-of-river plant on the Danube. However, the installed capacity of the run-of-river power plant is 300MW and the wind park capacity is more than 900MW. [5]

An increasing amount of so called new renewables is not only expected for the European Union. In the new policy scenario mentioned in [28] the installed power capacity of these electricity sources increases rapidly world wide. Solar PV is even expected to overtake thermal power plant using coal as energy source. [28]
This trend seems to be necessary in order to achieve decarbonization and scenarios tend to become real. Hence by citing [28]: *"Flexibility is the new watchword for power systems"*.

In the PLEF region (Central Western Europe - AT, BE, CH, DE, FR, LU, NL) Belgium and France currently (2018/19) tend to generate adequacy problems in serving their electricity demand and in ensuring the security of electricity supply. In the near future (2023/24) the situation in Germany, Luxembourg and the Netherlands is also expected to be tightened. Firstly, the whole region is affected to provide energy due to interconnectors and secondly, the economic model of Demand Side Flexibility (DSF) can improve the situation. [50]

Some events in the early past should be mentioned when talking about security of electricity supply:

Worst case scenario of a blackout happened in August 2003 in North America affecting Ontario in Canada, almost the entire state of New York and some parts of Michigan, Ohio and Pennsylvania. In total 63 GW were interrupted and 531 generating units at 261 power plants tripped from Eastern Interconnection of North America system. One key event were significant reactive power problems.[8], [4], [52]

Another blackout occured in Italy in September 2003 triggered by a tree flashover at an important connection line between Italy and Switzerland. Due to too large phase angle difference the connection was not allowed to be re-established by the automatic breaker control. As a consequence, other interconnections tripped due to overload and a nationwide blackout happened. [51], [12], [7]

All mentioned scenarios, considerations and events - whether national or international and whether the driving factor is supply security or environment protection respective reducing greenhouse gas - have one thing in common: the electricity supply system needs to get more flexible and necessity (but also effort) of power regulation and grid stabilization will increase.

In other words:*"The electricity sector is experiencing its most dramatic transformation since its creation more than a century ago"* [28].

1.2   Hydro power

In this section a rough overview is given and main components are depicted. For further details and more information it is referenced to literature - for example [23], [34], [33].

Hydro power processes potential energy of water into electrical energy. Potential energy results from geodetic difference in the altitude between headwater and tailwater. Run-of-river plants have a height difference of only a few meters in comparison to head of storage power plants, which is up to 1000 m high. Headwater is guided to the hydraulic machine by pipes, tunnels and shafts.

Depending on the application, different types of turbines are used. Basically they are split up in impulse and reaction turbines. The most common impulse turbine is *Pelton*; the most common reaction turbines are *Francis* and *Kaplan* turbines - all named after their developers. This thesis deals with the Francis type. All main parts of an exemplary machine unit are illustrated in Figure 1.3.

After water passes headwater sided shut-off device it is distributed uniformly over the circumference by the spiral case and guided to the runner by stay and guide vanes. The guide vanes are used for discharge regulation and mainly define the absolute flow angle at the runner inlet. At the runner most of the potential energy is converted into kinetic energy and the fluid is deflected and accelerated. After

passing the runner water flows through the draft tube, where it is decelerated due to cross-section expansion and finally guided to tail water. At the runner kinetic energy is transformed into mechanical energy and the runner is set into rotation. In last consequence the generator, connected to runner by turbine shaft, converts mechanical into electric energy. Used generators are synchronous or asynchronous ones, sometimes equipped with a frequency converter to adjust speed in a limited range.

In case of a pump storage power plant the previously described process is also reversible executed. Therefore, a pump is used as additional hydraulic machine or the turbine is designed as so called *pump-turbine*, which can be operated in pump and turbine mode.
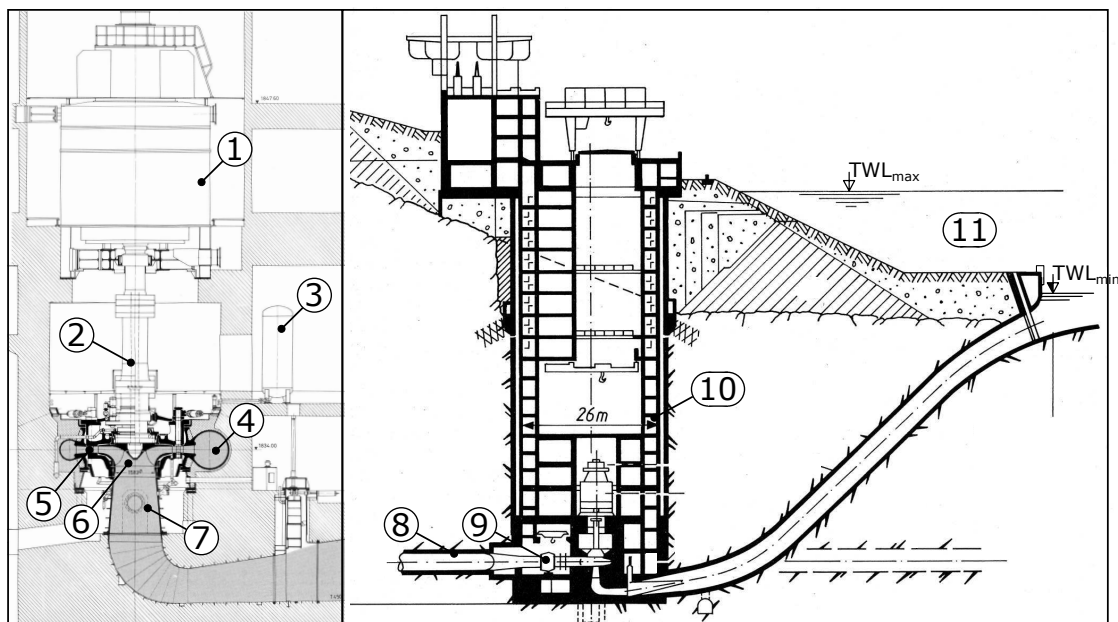

Figure 1.3: Main components of typical Francis or radial pump-turbine machine unit: 1 generator, 2 turbine shaft, 3 pressure air system, 4 spiral case, 5 stay and guide vanes, 6 runner, 7 draft tube, 8 penstock, 9 shut-off device, 10 powerhouse, 11 tailwater; (Illustration reproduced from [34])

1.3   Research objectives and motivation

Previously described growing demand of flexibility, power management and grid services lead to a rising number of start/stops. Furthermore, machine units are operated for an increasing amount in standby and regulation mode. In principle hydro power units are well suited for that [25]. They cover a wide power range, are very flexible in operation and allow short switching times in comparison to other types of power plants. Moreover, hydro power only depends on the weather

(rainfall) on long term, it is well predictable, manageable and one of the oldest and well developed renewable energy sources. Hence it is suitable for future challenges.

One of the previously mentioned regulation modes is synchronous condenser mode - described in section 2.1. In order to operate a machine unit at synchronous condenser mode, in standby or for pump start up the runner is dewatered. Therefore the water level is depressed beneath the runner by pressurized air and runner rotates above a free surface. During this operation conditions a free surface oscillation is excited under some conditions.

Especially the standby operation and synchronous condenser mode can last for long time periods. In recent time this operating conditions gain in importance, but appearing flow phenomena are not completely investigated (see section 2.2 State of research). Some statements are conflicting and some investigations have been conducted before the availability of digital measurement technology.

Future research of the Institute of Energy Systems and Thermodynamics will focus on start/stop and regulation modes in regards of effects onto hydraulic machines. In the past few years reseach has been done on the lifetime, fatigue analyses and the behavior of Francis and pump-turbines operated under off design conditions [18], [32]. Furthermore, the application of hydro power in order to balance volatile renewable ewnergy source has been studied [36]. This thesis shall build a basis for further experimental, analytical and numerical investigations of the synchronous condenser mode and the appearing free surface oscillation with future focus on appearing problems in dewatered operation. This will allow further considerations on stresses and operating behaviour of radial turbines. Actually occurring free surface oscillation shall be investigated from a scientific point of view.

The research objectives of this thesis shall be:

- Model pump-turbine at hydraulic laboratory of IET - TU Wien operated with depressed water level under different operating parameters shall be investigated;

- amplitude and frequency of free surface oscillation has to be detected and investigated;

- the general behaviour and occurring flow phenomena shall be described;

- a simplified analytical approach has to be developed to interpret the experimental results; and

- influence parameters as well as main flow processes shall be identified.

CHAPTER 2

Theoretical background

Chapter 2 deals with the theoretical background of this thesis. First, the synchronous condenser mode and the reactive power regulation by means of a synchronous machine is described.

Then the state of research is presented. All required dimensionless numbers are defined in general notation with a special focus on the densimetric Froude number Fd.

Finally, theoretical considerations of the measurement uncertainties are mentioned and the systematic and random measurement uncertainties are defined.

2.1 Synchronous condenser mode

A hydro power unit mainly consists of an electric and a hydraulic machine. The synchronous condenser mode primarily affects the synchronous generator of the machine unit. From the point of view of the hydraulic machine hydro power units are operated in synchronous condenser mode under same conditions as in stand-by mode or if operated as spinning reserve. Due to additional mechanical inertia (spinning reserve) the power system is more stable when system loads vary quickly [25]. Basically hydro power units operated in synchronous condenser mode are used for power factor regulation.

Low power factor results in negative effects on voltage control and system operation costs. It reduces generator, cable, transformer and transmission line capacity. Additional low voltage and voltage swings at remote load side are caused by low power factor. [25]
The power factor is defined as ratio of real power P in kW to apparent power S in VA as

$$PowerFactor = \frac{P}{S} = \cos\phi \qquad (2.1)$$

which is equal to cosine of phase angle ϕ. The relation between real power P, reactive power Q and apparent power S is

$$S = \sqrt{P^2 + Q^2}. \qquad (2.2)$$

The previously mentioned phase angle ϕ is load-dependent. Capacitive load results in a leading power factor and a negative phase angle. Inductive load causes a lagging power factor and positive phase angle. In order to ensure grid stabilization, inductive reactance has to be added to a capacitive system and vice versa to achieve the required phase angle ϕ respectively power factor.

Generally, a synchronous generator can be operated in overexcitation and underexcitation. In case of overexcitation it generates reactive power and consumes reactive power if underexcited. Figure 2.1 shows a capability curve of a synchronous generator. Generated reactive power is limited by current limiter in overexcitation (lagging power factor). Operated with leading power factor in underexcitation amount of consumed reactive power is limited by heating limitation of stator core end packages. General range of reactive power regulation of a synchronous generator is in synchronous condenser mode wider than in generation mode. [37]
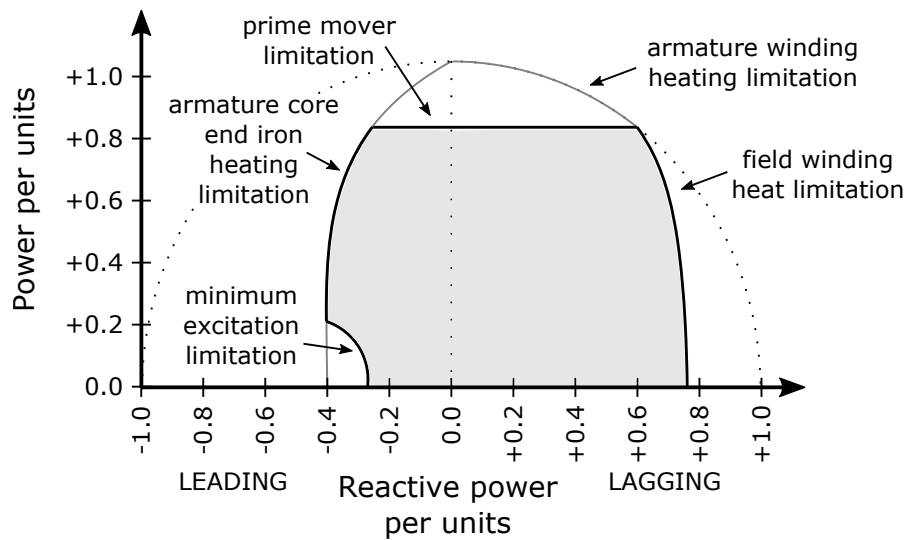
Figure 2.1: Exemplary capability curve of a synchronous generator [22]

However, if a synchronous machine is connected to an electrical system (power grid) it is supplying or absorbing reactive power. The operating regions of a synchronous machine are illustrated in Figure 2.2. It is able to provide capacitive or inductive reactance in a variable range and theoretically infinitely increments. Thus a synchronous generator is an attractive device for correction of power factor. [25]
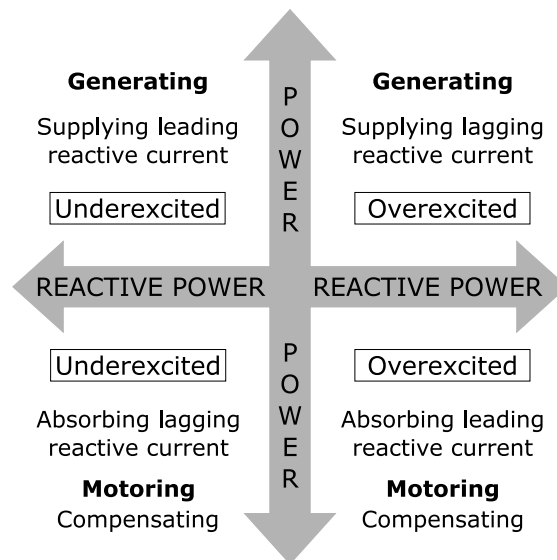

Figure 2.2: Operating regions of a synchronous machine [25]

The time period and basic suitability of a machine unit to be operated in synchronous condenser mode mainly depends on the hydraulic machine. Technical regulations or the turbine manufacturer specifies the scope of application. [37]
The synchronous machine consumes real power, if it is in operation as synchronous condenser. Consumed power is caused by mechanical, electrical, friction and windage losses. In most cases generator and runner are permanently connected. If the runner rotates in water, the power consumption is 15-20% of the rated power. If the machine is dewatered and the runner is rotating in air, the consumed power is only 2-4%. [41], [40], [37]
Due to this fact dewatering is state of the art. Therefore headwater sided valve and guide vanes are closed. In the next step water is removed from the runner. This procedure depends on the net positive suction head (NPSH) of the hydraulic machine. If NPSH < 0 (tailwater level deeper than runner level) draft tube needs to be aerated to avoid vacuum. In case of NPSH > 0 compressed air is blown into the draft tube and/or runner region. Resulting the water level is depressed below the runner and forms a free surface at the draft tube cone as illustrated in Figure 2.3.
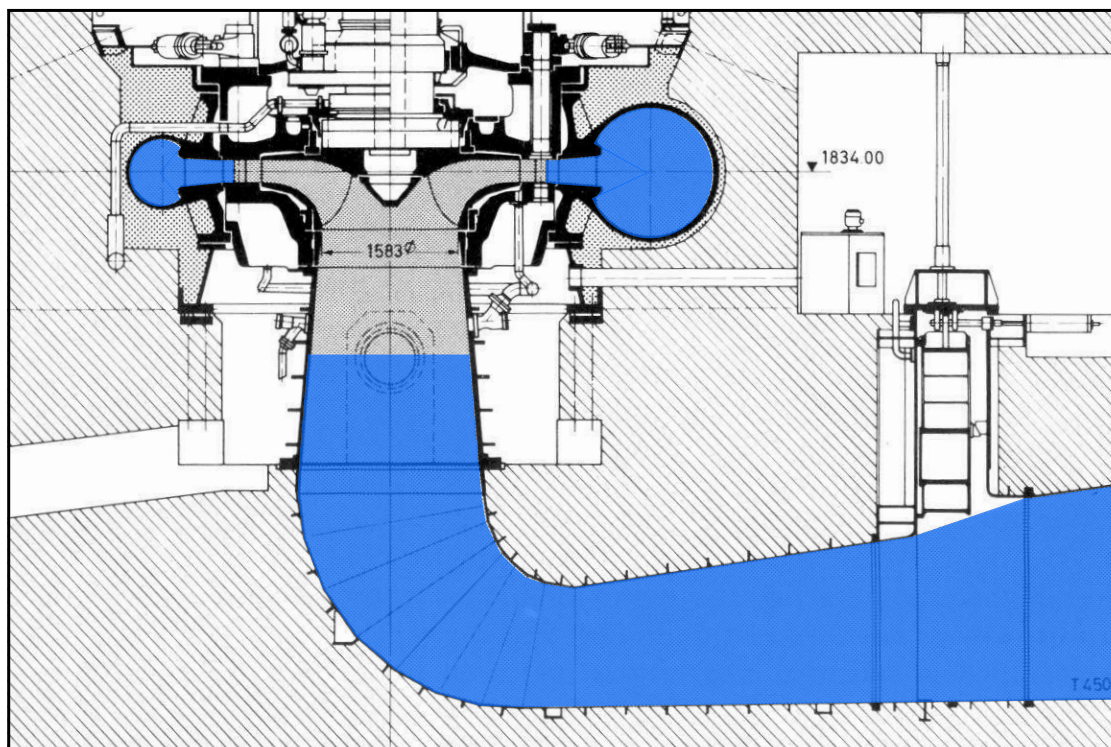

Figure 2.3: Dewatered Francis turbine and free surface below runner adapted from [34]

A characteristic oscillogram of the main parameters during the process of switching a hydropower unit to synchronous condenser mode is illustrated in [42]. High

pressure air systems are described in detail in [40] and characteristics of air system parameters are depicted as well.

The water level is monitored by minimal two level sensors. On the one hand, they are used to trigger compressed air in the dewatering process. On the other hand the sensors are used to ensure that the water level doesn't rise above a defined limit. During dewatered operation the water level in the draft tube may rise because of air diffusion. If that's the case, the upper limit sensor triggers a valve and compressed air is blown into the draft tube again.

2.2 State of research

One of the first papers dealing with hydraulic machines in synchronous condenser operation is [63]. Model tests have been conducted for a model pump-turbine operated in synchronous condenser mode. Filling up and dewatering process as well as pump start up are investigated too. Furthermore different solutions for treatment of cooling water discharge with empty and filled up spiral case are described. Investigations regarding synchronous condenser operation focus on two aspects. First discharge of cooling water is studied. Main parameter is the head of the rotating water ring between runner and guide vanes. Second aspect are pulsations triggered by the water ring. Executed measurements cover pulsations at shaft torque, guide vane torque, guide vane thrust, turbine cover pressure, spirale case pressure and radial runner thrust. Flow phenomena at the draft tube are unattended in this paper.

The motion of the free surface at the draft tube is observed in [10]. Model tests are executed with depressed tailwater level on models of pump-turbines and Francis turbines with different specific speed. Presented investigations analysed the dependency of free surface amplitude and frequency on main geometrical parameters of the draft tube and the free water level. The free water level is reported as most influencing the amplitude of the free surface motion. According to this paper the amplitude is independent of the runner rotation direction and sense of rotation is in accordance with rotation direction of the runner. The frequency of the free surface motion is reported to be constant and independent upon runner speed and water level. Furthermore a mathematical model of the rotating wave is presented.

[48] mentions the free surface motion in the draft tube of a prototype machine. The paper bases on operation experiences of 16 units of high head radial pump-turbines. The flow phenomenon occurred during start up in air as pump when runner rotation speed reaches rated speed.

Another early investigation regarding the motion of the depressed water in a draft tube in dewatered operation has been carried out by [47]. This paper presents an experimental investigation and a similarity law regarding the influence of air density and runner speed. As a result a dimensionless key figure, called *densimet-*

ric Froude number Fd is introduced. This dimensionless quantity represents the similarity concerning runner speed and air density in an effective manner.

An actual study on the motion of free water surface is presented in [54] and [57]. This study back up the use of densimetric Froude number as scaling parameter for different operation points. The interest of using this dimensionless number to study the motion in the draft tube cone is confirmed and it allows a reduction of the parameters influencing the behaviour of water surface.

Another actual investigation pointing out the importance of researching the synchronous condenser mode is presented in [59]. Prototype measurements are performed and the effects on the machine vibration, fatigue and the runner stress are studied. [55] and [56] presents experimental investigations of synchronous condenser mode. Model tests are conducted on a Francis turbine and focus on the rotating water ring between closed guide vanes and runner.

The motion of the free surface in the draft tube is often treated or considered as sloshing motion. Sloshing motions in tanks are well investigated. Experimental investigations regarding sloshing liquids in a tank are presented for example in [44], [19] and [49]. Numerical investigations relating to this topic are performed and published for example in [58]. Most of this publications focus on rectangular tanks. In [35] circular and square-base tanks are investigated and [21] deals with linear and nonlinear fluid sloshing in a circular, conical tank.

[61] and [62] present experimental and numerical investigations of the free surface flow driven by a rotating disc at the bottom of a stationary cylindrical tank. The ratio of water depth to tank radius is smaller than 0.25. Hence, the conditions are equal to shallow water. Investigations of the free surface motion in a cylindrical tank with water depth two times higher than the tank radius are presented in [45] and [46]. The flow is driven by a disc, mounted at the top of the tank and rotating in air. In [53] a quite similar setup is presented, but the flow is driven by a fan instead of a disc.

Previous treated issues are flow phenomenons in specific cases. Hydrodynamics, surface waves and rotating flow are treated in a wide range and more general way in [31] and [11]. [24] deals with internal flows and [26] with liquid sloshing.

2.3 Dimensionless numbers

Afterwards all used dimensionless numbers are listed. They are presented in general notation. Depending on specific case the characteristic parameters are defined and described later on.

- **Reynolds number** Re
  Reynolds number is defined as the ratio of inertia forces to viscous forces resulting in

$$Re = \frac{CL}{\nu} \tag{2.3}$$

  with the characteristic velocity C, characteristic length L and kinematic viscosity of fluid ν. Reynolds number is used to determine whether a flow is laminar or turbulent.

- **Ekman number** Ek
  The Ekman number provides information on the order of magnitude of the Ekman layer thickness. Ekman layer is a boundary layer in which Coriolis effect balances viscous diffusion. For small layers disturbances are able to propagate without being completely dissipated by friction losses. Hence the Ekman number Ek is the ratio of viscous forces to forces due to Coriolis effect. It is defined as

$$Ek = \frac{\nu}{\Omega D^2} \tag{2.4}$$

  where Ω is the characteristic angular velocity and D the characteristic diameter.

- **Froude number** Fr
  Fr is a dimensionless quantity used to describe free surface and open channel flows. It is defined as the square root of the ratio of inertia forces to gravity forces. Therefore the Froude number is expressed as

$$Fr = \sqrt{\frac{C^2}{gL}} = \frac{C}{\sqrt{gL}} \tag{2.5}$$

  with the characteristic velocity C, gravity constant g and characteristic length L.

- **Mach number** Ma

  The Mach number describes the ratio of flow velocity to the velocity of sound. It is primary used as criterion whether a flow medium is treated as incompressible or compressible. Assuming an ideal gas, the Mach number Ma is calculated as

  $$Ma = \frac{C}{\sqrt{\gamma R T}} \tag{2.6}$$

  with the characteristic velocity C, the specific heat ratio γ, the specific constant of gas R and the temperature of the fluid T. The denominator is equal to the speed of sound.

- **Speed factor** N_{QE}

  The speed factor allows to categorize hydraulic machines in a standardized way. According [27] speed factor is

  $$N_{QE} = n \cdot \frac{Q^{1/2}}{E^{3/4}} \tag{2.7}$$

  with nominal runner speed n, machine discharge Q and specific energy of the hydraulic machine E. All parameters are used in S.I. units.

- **Specific speed** n_q

  Although already replaced by N_{QE} historic notation n_q is still common used. It is defined as the speed of a geometrical similar machine at a head of one meter and a discharge of $1 m^3/s$. In equation

  $$n_q = n \cdot \frac{Q^{1/2}}{H^{3/4}} \tag{2.8}$$

  the nominal speed of the hydraulic machine n is used in revolutions per minute. Discharge Q and head H are used in S.I. units.

2.4 Densimetric Froude number

The densimetric Froude number is probably the most important dimensionless quantity for investigations regarding free water surface in the draft tube cone of a hydraulic machine. Therefore, this separate section is dedicated to this topic. Literature provides two related definitions. These two and the one used in this thesis are listed and discussed.

- **Densimetric Froude number** Fd_T **[47]**
  Basing on Froude number Fr (see equation 2.5), which is related to water itself, a dimensionless key figure is introduced in [47]. So called *densimetric Froude number* concerns the interaction between air and water surface depending on runner speed and density of medium. The densimetric Froude number according to referred publication is denoted as Fd_T hereinafter and defined by following equation

$$Fd_T = \sqrt{\frac{\rho_A}{\rho_W - \rho_A}} \frac{u_2}{\sqrt{gD_2}} \tag{2.9}$$

  with ρ_A and ρ_W the density of air and water, D_2 low pressure side diameter of the runner, u_2 the circumferential velocity of the runner at diameter D_2 and the constant of gravity g. As described in detail in [47] equation 2.9 is the ratio of kinetic energy of air to potential energy of water.

- **Densimetric Froude number** Fd_V **[57]**
  The use of densimetric Froude number as dimensionless number for free surface investigations is additionally confirmed and reinforced by [57]. In this publication the densimetric Froude number is defined as

$$Fd_V = \sqrt{\frac{\rho_A}{\rho_W}} \frac{\Omega_R \sqrt{D_1}}{\sqrt{g}} \tag{2.10}$$

  with density of air and water ρ_A and ρ_W, angular velocity of the runner Ω_R, D_1 high pressure side diameter of the runner and gravitational constant g.

- **Densimetric Froude number** Fd
  First definition according to [47] is mentioned in this thesis, but due to usual values of ρ_A and ρ_W (therefore $\frac{\rho_A}{\rho_W} \ll 1$) the following simplification is taken into account:

$$\sqrt{\frac{\rho_A}{\rho_W - \rho_A}} = \sqrt{\frac{\frac{\rho_A}{\rho_W}}{1 - \frac{\rho_A}{\rho_W}}} \approx \sqrt{\frac{\rho_A}{\rho_W}} \tag{2.11}$$

  As a result the densimetric Froude number Fd is hereinafter defined as

$$Fd = \sqrt{\frac{\rho_A}{\rho_W}} \frac{u_2}{\sqrt{gD_2}} \tag{2.12}$$

  with the density of air ρ_A and water ρ_W, the constant of gravity g, low pressure side diameter of the runner D_2 and u_2 the circumferential velocity

of the runner at diameter D_2. The relation between densimetric Froude number and Froude number is

$$Fd = \sqrt{\frac{\rho_A}{\rho_W}} Fr \qquad (2.13)$$

with the Froude number Fr as defined in equation 2.5.

- **Comparison and relationship** Fd_T, Fd_V, Fd
  For reasons of comparison with the literature the relationship and difference of Fd_T, Fd_V and Fd is pointed out subsequently.
  In equation 2.9 and 2.12 low pressure side diameter D_2 is used as characteristic length. In contrast 2.10 is defined by the high pressure side runner diameter D_1 (see also [47] and [57]). The extending equation 2.10 by D_2 results in

$$Fd_V = \sqrt{\frac{\rho_A}{\rho_W}} \frac{\Omega_R \sqrt{D_1}}{\sqrt{g}} = \sqrt{\frac{\rho_A}{\rho_W}} \frac{\Omega_R \sqrt{D_2}}{\sqrt{g}} \sqrt{\frac{D_1}{D_2}} \qquad (2.14)$$

which is comparable to other definitions. D_1 is the high pressure side diameter of the runner and D_2 is the low pressure side diameter. Exchanging characteristic kinematic quantity in equation 2.14 leads to

$$Fd_V = \sqrt{\frac{\rho_A}{\rho_W}} \frac{2u_2}{\sqrt{gD_2}} \sqrt{\frac{D_1}{D_2}} \qquad (2.15)$$

According to equation 2.11 density ratio is

$$\sqrt{\frac{\rho_A}{\rho_W - \rho_A}} \approx \sqrt{\frac{\rho_A}{\rho_W}} \qquad (2.16)$$

Finally the relation of Fd_T, Fd_V and Fd can be written as

$$Fd = Fd_T = \sqrt{\frac{D_2}{D_1}} \frac{Fd_V}{2} \qquad (2.17)$$

2.5 Theoretical considerations on measurement uncertainties

No measurement system behaves like a perfect one. In contrast, results of every measurement are falsified by internal and external influences. Consequently, measurement errors occur and the measurement result deviates from the real physical value in a larger or smaller dimension. For example overlaying polarization voltage influences detection electrode of electromagnetic flowmeters used for discharge measurements. [2]

According to [14] a measurement value x related to a measured quantity and explicit assigned to output of measuring instrument consists of

- true value x_t

- random measurement error e_r

- known (and determinable) systematic measurement error $e_{s,k}$ and

- unknown (and not determinable) systematic measurement error $e_{s,u}$

$$x = x_t + e_r + e_{s,k} + e_{s,u} \qquad (2.18)$$

Averaging all measurement values results in mean value $\overline{x}$

$$\overline{x} = \sqrt{\frac{1}{n}\sum_{i=1}^{n} x_i^2} \qquad (2.19)$$

with number of measured values n and single measurement values x_i. The higher the number of measurement values, the closer the mean value $\overline{x}$ gets to the expected value μ. As explained in Figure 2.4 μ differs from the true value x_t by the systematic measurement error e_s, which is the sum of known $e_{s,k}$ and unknown $e_{s,u}$ error.
In other words the random measurement error e_r would be insignificantly small for an infinit number of measured values. As it is possible to take the known systematic measurement error $e_{s,k}$ into account, the total measurement error is reduced to the unknown systematic measurement error $e_{s,u}$. [15]

Known systematic measurement errors have the same amount and algebraic sign for similar measurement conditions. For example one reason can be an exposure of measurement object by instrumentation. [2]
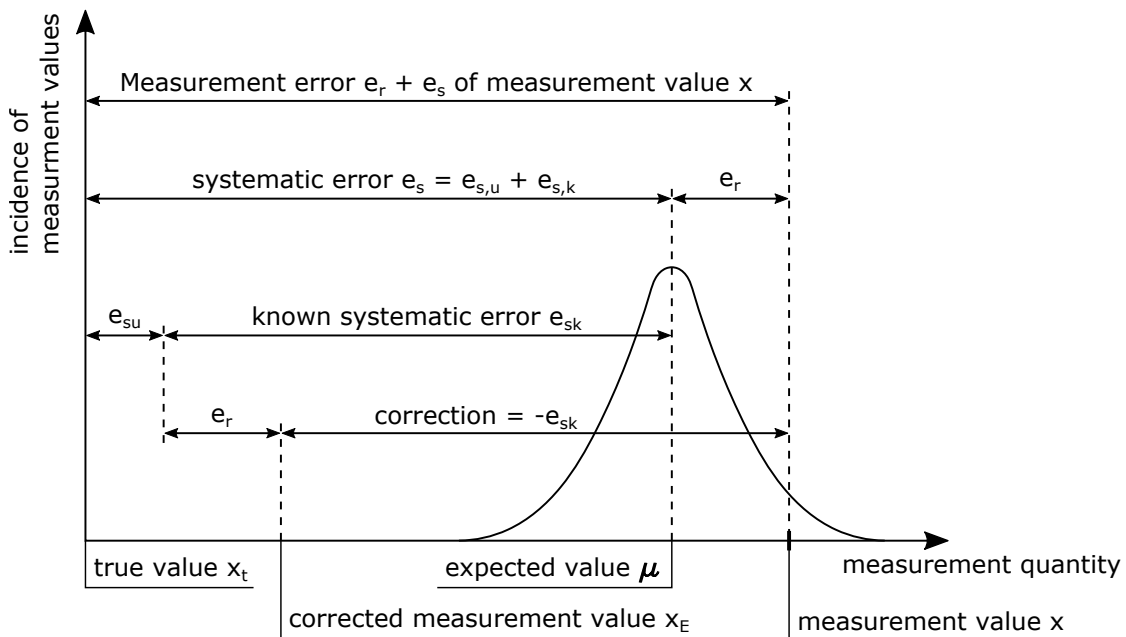That kind of errors are considered and corrected appropriatly. In literature the

Figure 2.4: Explaining schedule of measurement value and measurement errors [14]

wording *corrected measurement value* x_E is often used and according [14] defined as

$$x_E = x - e_{s,k} \tag{2.20}$$

Subsequently, known systematic errors are not explicit mentioned (but considered) and the measurement value x is understood as corrected measurement value.

Some quantities cannot be measured directly, but calculated by means of measurement quantities $X_j(j = 1, 2, \ldots, m)$. One example is the densimetric Froude number Fd. Such values are called target values Y and the functional link is so called process equation [2]

$$Y = f(X_1, X_2, \ldots, X_m) \tag{2.21}$$

with the number of measurement quantities m.

Trying to evaluate the quality of measurement a statement about measurement errors has to be done. Therefore measurement uncertainty is used as evaluation criteria.
The term *measurement uncertainty* is to be understood as an estimated value. It specifies the range in which true value X_t is within [2]. Calculation or respectively estimation of measurement uncertainty is split up in random and systematic mea-

surement errors.

Random measurement uncertainty u_r:
The random measurement uncertainty is the empirical standard deviation of the mean value and according [15] defined as

$$u_r(X_j) = u_r(\overline{x_j}) = \sqrt{\frac{1}{n(n-1)} \sum_{i=1}^{n} (x_i - \overline{x_j})^2} \tag{2.22}$$

where n is the number of measured values, x_i the number of single measurement values and $\overline{x_j}$ the mean value. For the target value Y equation is adapted and results in

$$u_r(Y) = \frac{1}{n(n-1)} \sum_{i=1}^{n} (x_{ji} - \overline{x}_j)(x_{ki} - \overline{x}_k) \tag{2.23}$$

with target function Y depending on measurement quantities X_j and X_k. [16]

Systematic measurement uncertainty u_s:
For the calculation of the systematic measurement uncertainty a rectangular distribution is assumed. In accordance with [15] u_s can be estimated as

$$u_s(X_j) = \frac{b-a}{\sqrt{12}} \tag{2.24}$$

with lower and upper limits a and b ($a < b$). They are the known limits of possible values for X_j. The constant value of the divisor results due to the assumed distribution of values.

The **Total measurement uncertainty** results from quadratic addition of both parts

$$u = \sqrt{u_s^2 + u_r^2} \tag{2.25}$$

Hence, the systematic measurement uncertainty of a measurement quantity X_j is

$$u(X_j) = \sqrt{u_s(X_j)^2 + u_r(X_j)^2} \tag{2.26}$$

with random measurement uncertainty u_r and systematic measurement uncertainty u_s. In general notation, the systematic measurement uncertainty of a target

value Y is

$$u_s(Y) = \sqrt{\sum_{j=1}^{m} \left(\frac{\partial Y}{\partial X_j} \right)^2 u(X_j)^2} \qquad (2.27)$$

according to [16] and depends on the measurement quantities as defined by functional link (equation 2.21.

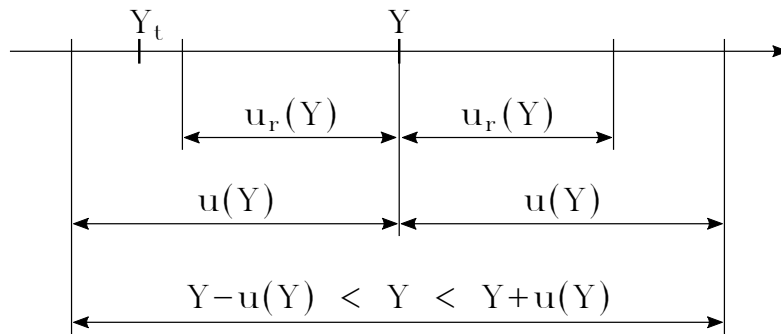The confidence range caused by measurement uncertainty of measurement value

Figure 2.5: Confidence range of target value Y

$\overline{x_j}$ regarding X_j is

$$\overline{x_j} - u(x_j) \leq \overline{x_j} \leq \overline{x_j} + u(x_j) \qquad (2.28)$$

and of the target value Y

$$Y - u(Y) \leq Y \leq Y + u(Y) \qquad (2.29)$$

which is also illustrated in Figure 2.5.

CHAPTER 3

Experimental setup

This chapter deals with the experimental setup of model tests and the measurement framework. Test facilities and the model machine used for the investigation are presented and explained with focus on essential parts for free surface oscillation. Model or rather experimental simplifications, which have to be taken into account, are discussed and settings as well as general test conditions are described. Experiments are conducted in accordance with a defined measurement procedure to ensure reproducibility. The procedure depends primarily on different reached states of free water surface. They are explained in the following. Finally, general and specific instrumentation and measurement uncertainties are delineated.

3.1 Test rig

All model tests are conducted at the test facilities of the Institute of Energy Systems and Thermodynamics (IET). Its hydraulic laboratory is part of the Science Center of TU Wien. The test rig is operated in a closed loop with the hydraulic circuit schema shown in Figure 3.1.
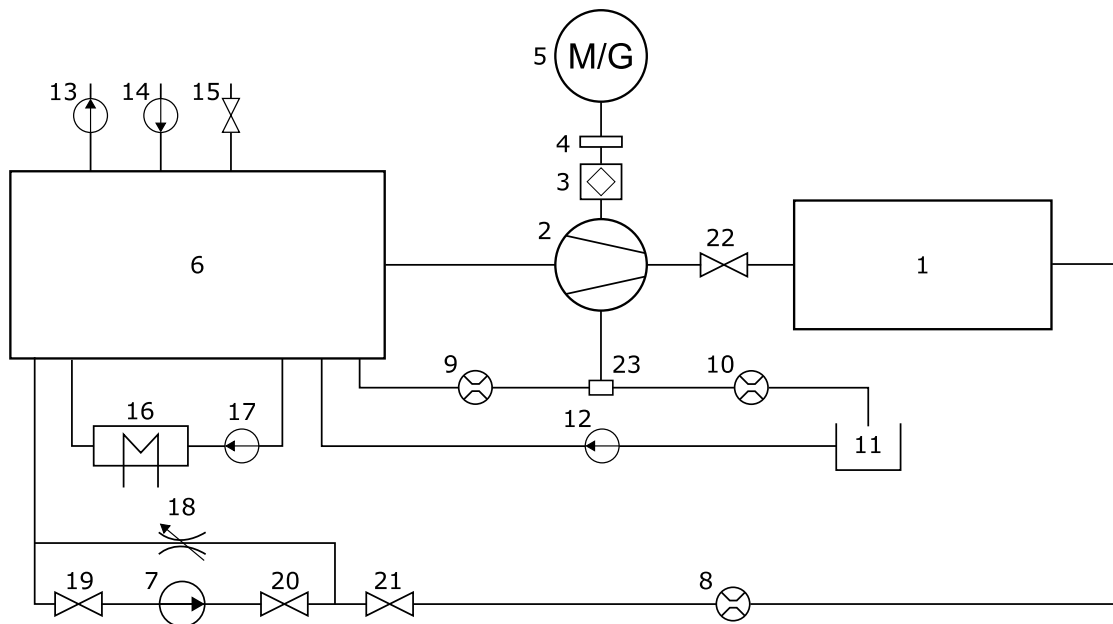

Figure 3.1: *hydraulic circuit schema:* 1 headwater vessel, 2 model machine, 3 hydrostatic bearing unit, 4 torque transducer, 5 motor generator, 6 tailwater vessel, 7 supply pump, 8 main flow meter, 9 and 10 leakage water flow meter, 11 compensation vessel, 12 compensation pump, 13 vacuum pump, 14 air compressor, 15 atmosphere valve, 16 circuit cooling, 17 cooling water pump, 18 needle valve, 19 - 21 butterfly valves, 22 spherical valve, 23 leakage water switch valve

Basically the main parts are the scale reduced model of a radial pump-turbine (2), the motor generator of the model machine (5), the headwater vessel (1) and the tailwater vessel (6). A spherical valve (22) is arranged on the headwater side at the spiral case inlet pipe to simulate start, stop or shut down conditions. The model machine itself is described in detail in section 3.2. A hydrostatic bearing unit (3) is arranged between the model pump-turbine and the torque transducer (4) to consider the torque losses due to friction in the shaft bearing. Axial thrust is also measured at the bearing unit. The instrumentation is explained in detail in section 3.4, where the main technical data are also provided.

The test rig is equipped with a $400\,kW$ motor generator (5) and a full size frequency converter for a 4-quadrant drive to adjust the runner speed. The possible speed

range is between -3000 to 3000 *rpm*. Leakage water at the headcover can be directly guided to the tailwater or flows into a compensation vessel (11) and is pumped back. In both ways, discharge is measured by flow meters (9, 10). The absolute pressure level at the low pressure side of the model machine can be regulated from 40 *mbar* to 6 *bar*. Therefore a vacuum pump (13) reduces the pressure or compressed air (14) is blown into the tailwater vessel. Using atmosphere valve (15) the low pressure side is either connected to the ambient or not. In order to ensure constant operation conditions during the experiments, the water temperature in the closed loop is regulated by a plate heat exchanger (16) installed at the tailwater vessel.
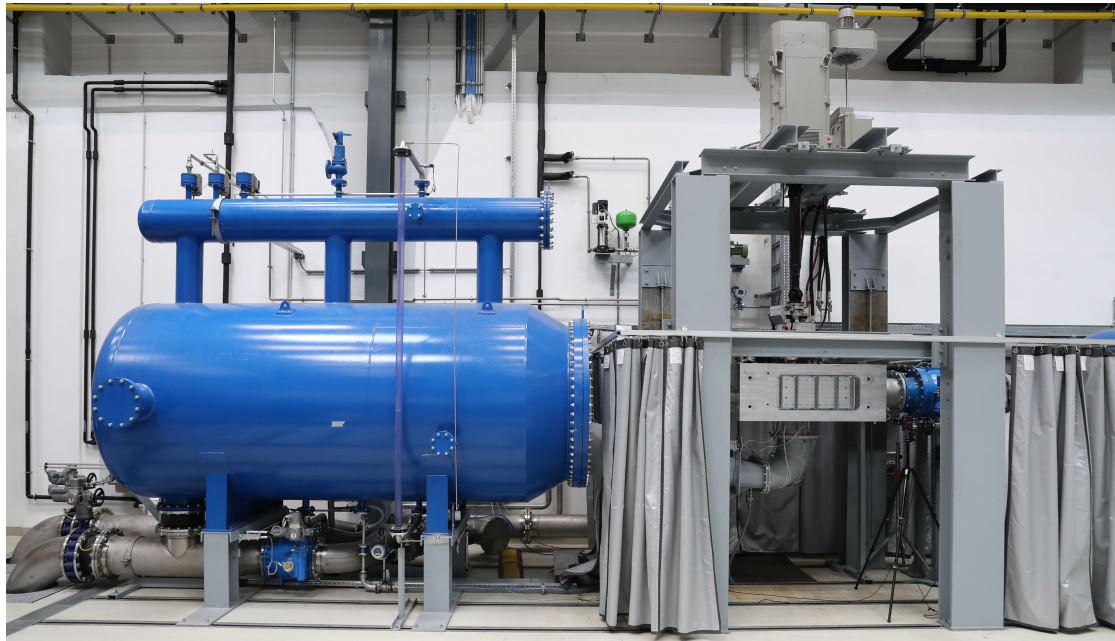

Figure 3.2: Universal test rig at hydraulic lab of Institute of Energy Systems and Thermodynamics at TU Wien

3.2   Model machine

Investigated model machine is a homologue scale reduced radial pump-turbine with a speed factor $N_{QE} = 0.126$ ($n_q = 41.8\ rpm$) in turbine mode and in pump mode $N_{QE} = 0.125$ ($n_q = 41.6\ rpm$). The specific speed N_{QE} is defined in 2.7 according to IEC 60193 [27] with runner speed n in s^{-1}, discharge Q in m^3/s and the specific hydraulic energy of the machine E in J/kg.

The model pump-turbine has 20 stay vanes and same number of guide vanes. Pump-turbine runner consists of seven runner blades with a high pressure side diameter $D_1 = 487.5\ mm$ and a low pressure side diameter $D_2 = 276.4\ mm$. In the course of the relocation of the laboratory the spiral case was newly manufactured and equipped with additional optical accesses for investigations developing on this thesis. Due to the need of better optical access for actual investigations, the steel structure of the test rig was redesigned and the spiral case is mounted hanging. This leads to less disturbing parts surrounding the draft tube cone and the low pressure side of the model machine.

One of the main machine components for the present thesis is the draft tube. It is single flow (undivided) and consists of four parts: draft tube cone, elbow, foot and tailrace. The draft tube is rotationally axis symmetric between point I and II for length $h_1 = 1.49 D_2$ as delineated in Figure 3.3. The total height h_2 is $3.16 D_2$ from the highest to the lowest point of draft tube. The streamline from point II to point IV has a length of $9.40 D_2$ and resulting total main streamline of the draft tube has a length of $10.89 D_2$. The volume of the draft tube is 522.74 litres and conical part volume is 30.76 litres (point I to II) which is a ratio of 5.9% of the total draft tube volume. The draft tube cone has an opening angle ϑ of 4.4° and a length of $1.17 D_2$.
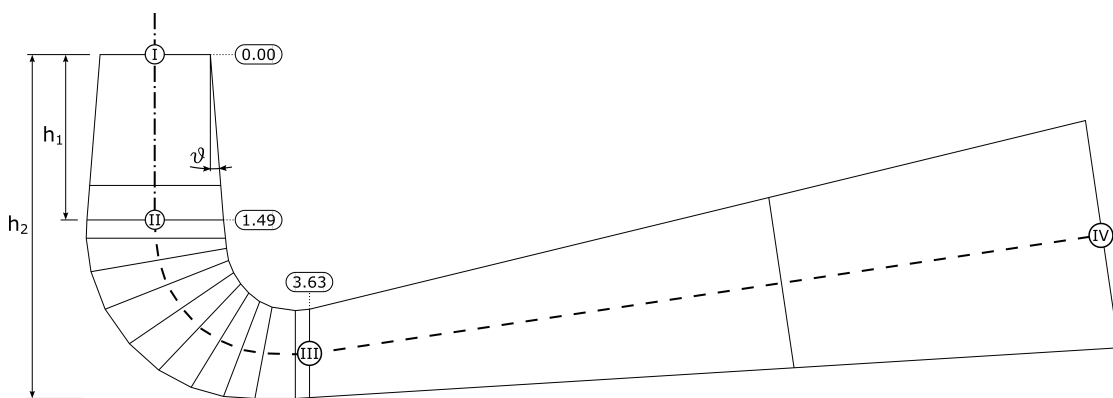

Figure 3.3: Dimensions, main streamline and contour of draft tube

Two cones are used for investigations: draft tube cone 1 is made of acrylic glass and cone 2 is made of steel and equipped with two optical accesses. Additional

information about the two draft tube cones is provided in section 3.4.2.

At the draft tube elbow an observation window is placed in the runner axis of rotation for optical observations of the runner and fluid flow from bottom view. There are also observation windows in the bottom ring, the stay vane ring and at the high pressure sided hub section of the runner. Therefore optical observations are possible at the low pressure side and from the stay vane channel to the high pressure edge of the runner. The optical accesses are used for non-invasive measurements such as PIV, LDA or high speed camera recording. As a result it is possible to investigate the flow through the stay vanes, guide vanes, the runner low pressure side and the draft tube. In Figure 3.4 the single components of the scale reduced model pump-turbine are demonstrated. Main technical data of the prototype and the model machine are listed in Table 3.1.
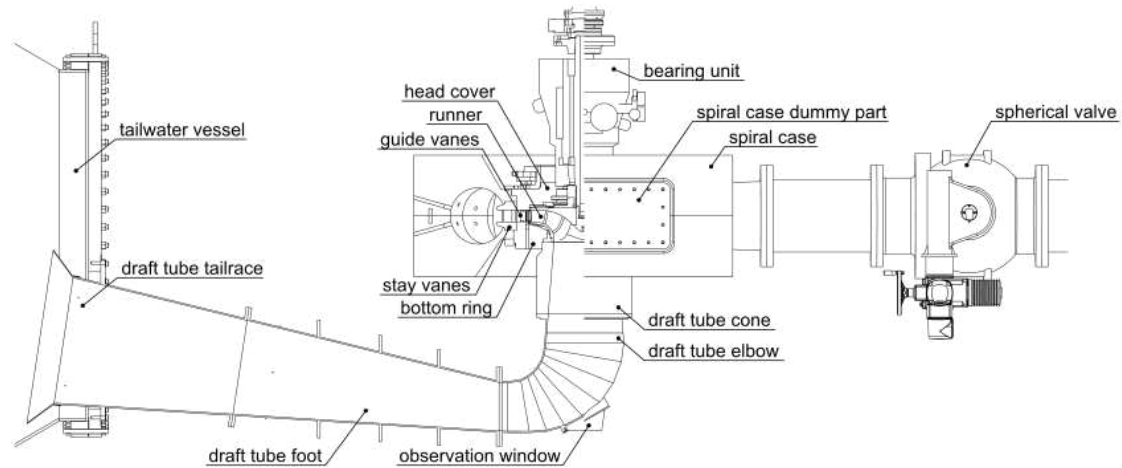

Figure 3.4: Main components of investigated model machine

Table 3.1: Main technical data of prototype and scale reduced model

	Prototype		Model	
	Pump	Turbine	Pump	Turbine
Rated head (m)	380	357.2	68.64	
Rated discharge (m^3/s)	81	72.85	0.377	
Rated power (MW)	275		0.253	
Runner diameter (m)	4.25		0.4875	
Runner speed (rpm)	400		1500	

3.3   Experimental modelling (relations and simplifications)

Experimental conditions and settings of the model pump-turbine are essential for the interpretation of the results, physical modelling and the understanding of physical relationships. The subsequent explained setting applies to all experiments, unless otherwise explicit stated.

Starting the description from the nominal high pressure side of the machine the spherical valve is closed. As a result there is no fluidic connection to the headwater vessel, which is filled up with water. Focusing on the free surface oscillation in the draft tube cone, the hydraulic flow phenomena at the high pressure side of the runner and the spiral case should be avoided. Therefore the spiral case is empty to ensure that no other influences disturb the measurements. The spiral case is connected with the draft tube by a connection pipe for pressure equalization similar to spiral case pressure relief. The different water-air regions and a simplified connection schema is illustrated in Figure 3.5.
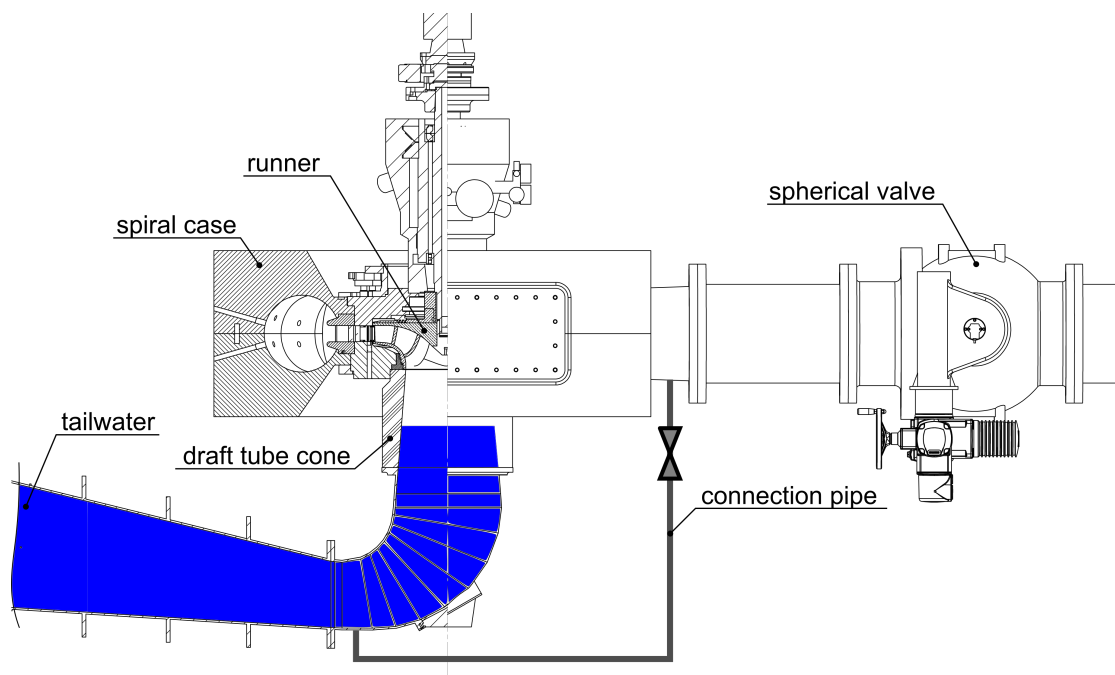

Figure 3.5: Cross section view of investigated model pump-turbine - Initial conditions of water volume and fluidic connections

As in prototype operation, the guide vanes are closed and the runner starts and rotates in air above a free water surface. Because of the empty spiral case there is no water ring as appearing in synchronous condenser mode of prototype [63], [10] and no cooling discharge through labyrinth sealing as this may cause torque fluctuations [55].

In comparison to [47] and [53] no blind plate is set at the tailrace. Trying to approximate prototype conditions, the water-volume in the draft tube is directly connected with the tailwater vessel. The atmosphere valve (15) is open and thus the tailwater is connected with the ambience. A schema of the tailwater connections and the whole closed loop is shown in Figure 3.1 (Section 3.1 Test rig). The vacuum pump (13), the compressor (14) and related valves are closed. All valves (18,19) connecting the tailwater vessel with the closed loop and other laboratory facilities are closed as well.

The draft tube cone (see section 3.2 and 3.4) is rotationally symmetric about the runner axis of rotation. The intersection point of the runner low pressure side plane and the axis of rotation is defined as the origin of coordinates. As illustrated in Figure 3.6 z-axis is directed downwards. The coordinate dimensioning for this axis is done in relation to the runner low pressure side diameter D_2. Therefore variable κ is introduced. It specifies z-coordinate as κ times D_2. The water level beneath the runner in resting state is labelled depending on factor κ with $E\kappa$ and called initial water level. For example the initial water level with z-coordinate $0.50D_2$ ($\kappa = 0.50$) is called $E0.50$.
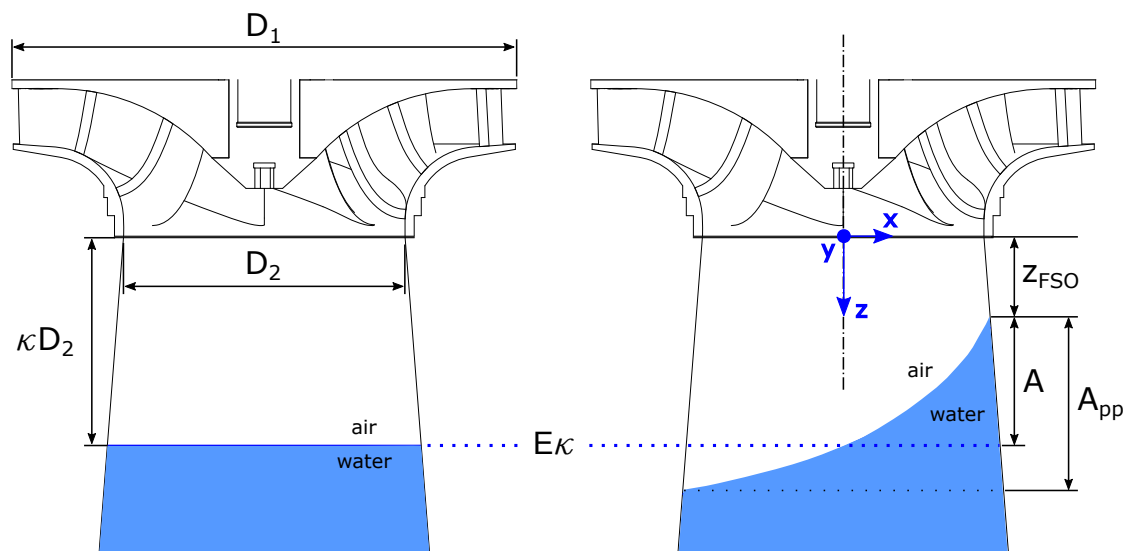

Figure 3.6: Simplified representation of draft tube cone region and illustration of coordinate system and important terms

In this thesis the term amplitude A is defined as the distance to the highest point of the free surface oscillation measured in relation to the initial water level. The highest point reached by water surface is the point with the shortest distance to the runner in an observed cross section as exemplarily shown in Figure 3.6 on the right side. This maximum reached free surface oscillation level is marked by coordinate z_{FSO}. The peak to peak amplitude A_{pp} is the level-difference between the maxima and minima of the free surface on both wall sides.

Z-coordinate was already mentioned in the text previously. In addition other cartesian and polar coordinates are defined according to Figure 3.7. A top view of the runner and the draft tube cone section is shown with cartesian coordinates (x, y) and related polar coordinate system (r, φ). Cartesian as well as polar coordinate system are coordinate systems in absolute frame of reference. Runner speed n, angular velocity of runner Ω_R and polar angle φ are positive in the same sense of rotation. By definition [27] the runner speed has a positive leading sign, if runner rotates in direction of turbine operation mode.
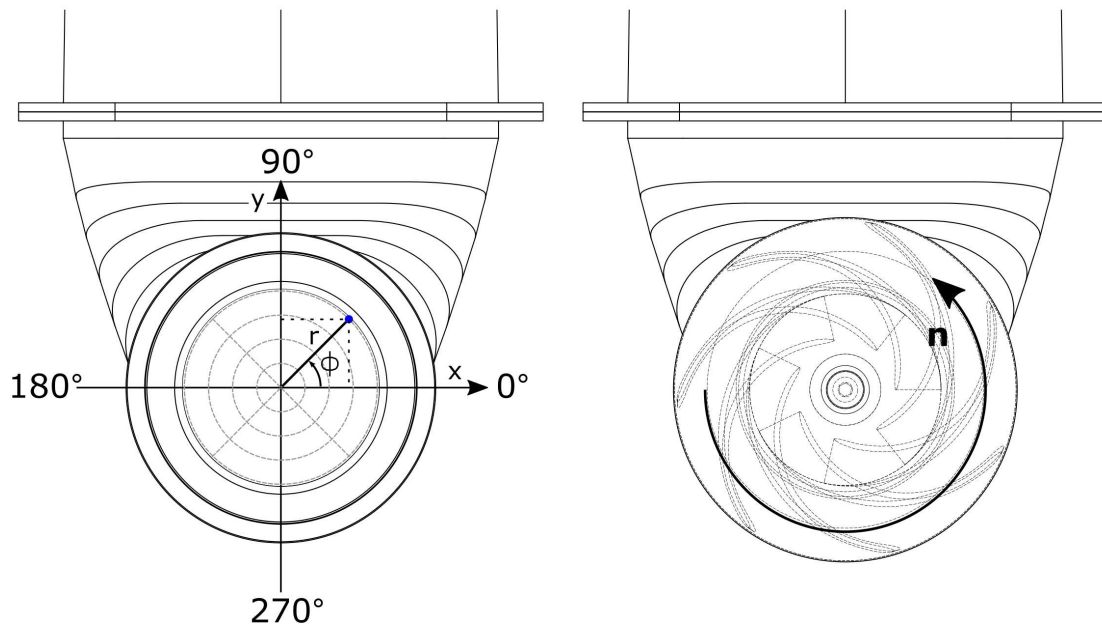
Figure 3.7: Top view of draft tube section with polar coordinate system, relating cartesian coordinates and positive direction of runner rotation

3.4 Instrumentation

This section deals with the instrumentation and setup of the scale reduced radial model pump-turbine. At first general instrumentation is described. Then technical data and settings of high speed camera recording are provided. Afterwards the fast response pressure transducer and the instrumentation of the draft tube cone are explained.

3.4.1 General instrumentation

Steady static pressure measurement sections and the installed torque transducer are shown in Figure 3.8.
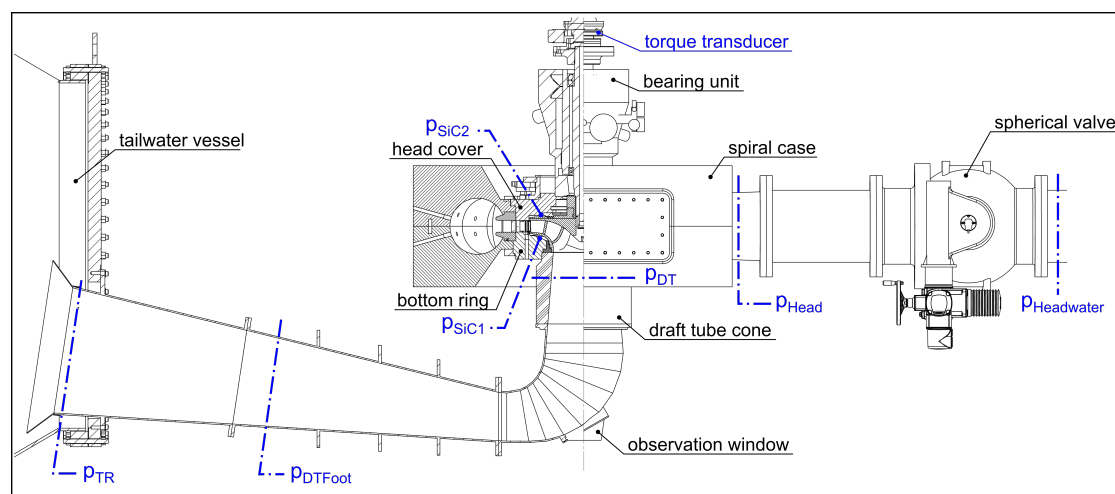

Figure 3.8: Sectional view of the model machine with steady static pressure measurement sections and torque transducer

The shaft torque measurement is conducted by a high precision torque transducer with a nominal torque of 3 kNm. The measurement frequency range is up to 6 kHz. Thus it is possible to detect even high frequency torque fluctuations and the sensor is suitable for the investigation of transient behaviours. The maximal error is $\pm$ 0.01 % of the nominal torque. As shown in Figure 3.1 the torque transducer (4) is arranged between the bearing unit (3) and the motor generator (5).

The runner speed n is measured by an optical speed rotation measuring system, which is part of the torque transducer. It uses infrared light and a metallic slotted disc with 360 mechanical increments. The pulse frequency at nominal speed is 72 kHz and the minimum rotational speed for sufficient pulse stability is two revolutions per minute. The optical speed rotation measuring system and torque transducer are one single unit. The temperatures are measured by a Pt100 resistance thermometer. The thermometer for water temperature is class A according IEC 60754 and located at the tailwater vessel near the draft tube outlet. Air temperature is measured at the draft tube cone pressure measurement plane $E0.10$ by

sensor type DIN/EN 60751 class B.

As shown in Figure 3.8 seven pressure monitoring sections are installed to evaluate the pressure conditions in the whole machine. $p_{Headwater}$ is at the headwater vessel side of the spherical valve and p_{Head} is placed at the spiral case inlet. The pressure sections p_{SiC1} and p_{SiC2} are located at the shroud and hub side chamber of the machine, beneath the runner high pressure side and the runner sealing. Three sections are used to measure the pressure distribution in the draft tube. Steady static pressure in the draft tube cone is measured at p_{DT}, located at $\kappa = 0.40$. The next measurement section downstream is p_{DTFoot} and the pressure at the tailrace of the draft tube is measured at p_{TR}. All pressure sections and technical data of the pressure transducers are listed in Table 3.2.

Table 3.2: Main technical data of steady static pressure transducers

measurement section	measurement range (bar)	max. error (% of full scale)
Headwater	-1 ... 10	0.08
Head	-1 ... 10	0.07
SiC1	-1 ... 10	0.075
SiC2	-1 ... 10	0.075
DT	-1 ... 4	0.075
DTFoot	-1 ... 10	0.075
TR	-1 ... 4	0.07

3.4.2   Draft tube cone 1 and 2

In the course of present thesis two draft tube cones are used for the model tests. Hydraulic contour is the same for both cones with an opening angle ϑ of 4.4° and a length of 324.7 mm. Mainly used cone is draft tube cone 1. The investigations presented in section 4.5 are conducted with cone 2.

Draft tube cone 1 is wholly made of acrylic glass and illustrated in Figure 3.10. In order to reduce refraction and alignment problems, the outside contour is octagonal. This cone was manufactured and used for LDA investigations in [17]. For actual investigation of free surface oscillation twelve additional measurement taps are implemented and described in section 3.4.3.
Draft tube cone 2 is made of steel with painted surface and equipped with two optical accesses. A cross sectional and a 3D view are shown in Figure 3.9. The two optical accesses are shifted by 90 degrees as illustrated. They can be closed by metallic dummy parts or in case of this investigation by acrylic parts. The inner contour of the insets is adapted to the cone contour.
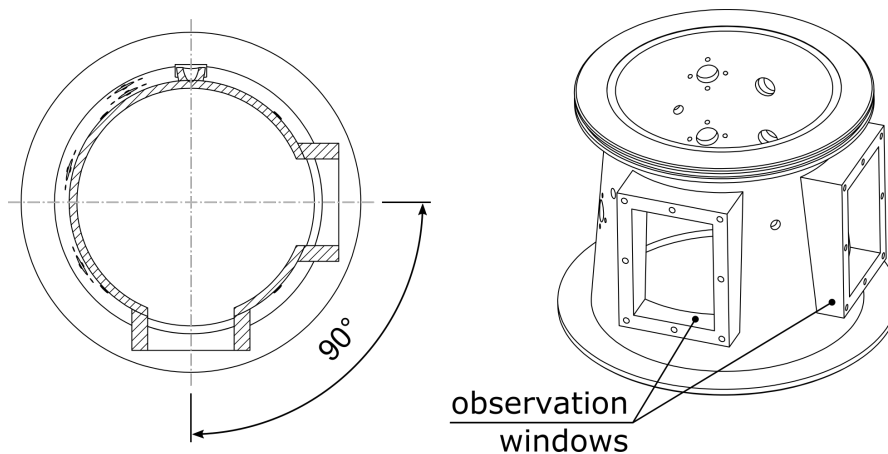

Figure 3.9: Draft tube cone 2 - cross sectional view (left) and 3D view (right)

3.4.3   Fast response pressure transducers

A cross sectional view of the radial model pump-turbine and pressure taps for fast response pressure transducers is illustrated on the right hand side of Figure 3.10. Starting from the high pressure side of the hydraulic machine, the first pressure taps are p_{SC} and three pressure taps p_{prim}. Pressure taps p_{SC} are arranged in each segment circumferential at the spiral case. The pressure taps p_{prim} are located in the vaneless space between guide vanes and runner. At the hub and shroud side chamber three pressure measurement sections p_{SiC} are implemented. p_{SiC1} and p_{SiC2} are used for steady pressure measurement with a ring manifold. p_{SiC3} is used for time resolved measurements by means of fast response pressure transducer.
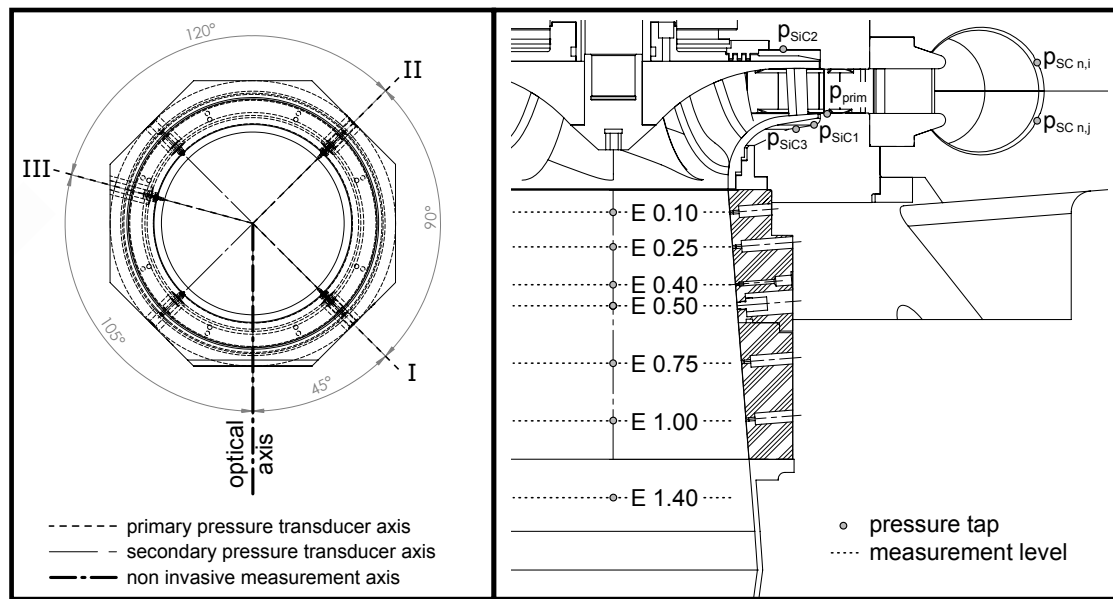
Figure 3.10: top view of draft tube cone 1 and measurement axis (left); cross section of radial model pump-turbine with pressure taps (right)

Draft tube cone 1 is equipped with fast response pressure transducers p_{DTcone} as well. Pressure taps p_{DT} at plane $E0.40$ are used to detect the steady static pressure as listed in section 3.4.1. All together seven measurement planes are defined at draft tube cone 1. The nomenclature of the planes provides information on the distance between measurement plane and the low pressure side of the runner with diameter D_2 as introduced in section 3.3 Experimental modelling (relations and simplifications). A top view of the measurement planes in the draft tube cone is illustrated on the left hand side of Figure 3.10. At $E0.25$, $E0.50$, $E0.75$ and $E1.00$ fast response pressure transducers are installed at the three primary pressure axes I, II and III. The axes are arranged asymmetrical for post processing reasons as executed in [30]. Only one fast response pressure transducer is mounted at $E0.10$ in axis I. Two fast response pressure transducers are mounted at $E1.40$ in primary and secondary axes I. The piezo resistive pressure transducers are sampled with 400 Hz. All fast response pressure transducers are flush mounted and the technical data are listed in Table 3.3.

3.4.4 High speed camera

The camera used for observation of the free water surface is a monochrome high speed camera with an active pixel sensor in CMOS technology with a sensor resolution of 1024 x 1024 pixels. The maximum frame rate is 170000 frames per second at 128 x 16 pixels and 2000 frames per second at full frame performance. Mounted camera lens has a focal length of 50mm and angle of view is 46 degree. Aperture is set as $f/2$.

Table 3.3: Main technical data of fast response pressure transducers

measurement section	measurement range (bara)	max. error (% of full scale)
SC	0 ... 10	±0.25
prim	0 ... 10	±0.25
SiC3	0 ... 10	±0.25
DTcone	0 ... 3.5	±1.0
DTcone	0 ... 7	±1.0
DTcone E0.50	0 ... 3.5	±0.1

The optical axis, as drawn in Figure 3.10 (left), defines the perspective of the high speed camera and other non-invasive measurements like LDA or PIV. The angular offset of the axis is 45 degree to primary pressure transducer axis I. The arrangement of the high speed camera and the data acquisition chain is schematically illustrated in Figure 3.11. Optical axis of the camera is arranged at an angle of 30 degree to the draft tube symmetry plane.

Main specifications of the high speed camera are listed in Table 3.4. The camera is synchronized with the fast response pressure transducers and the start of recording is triggered by the main measurement program.
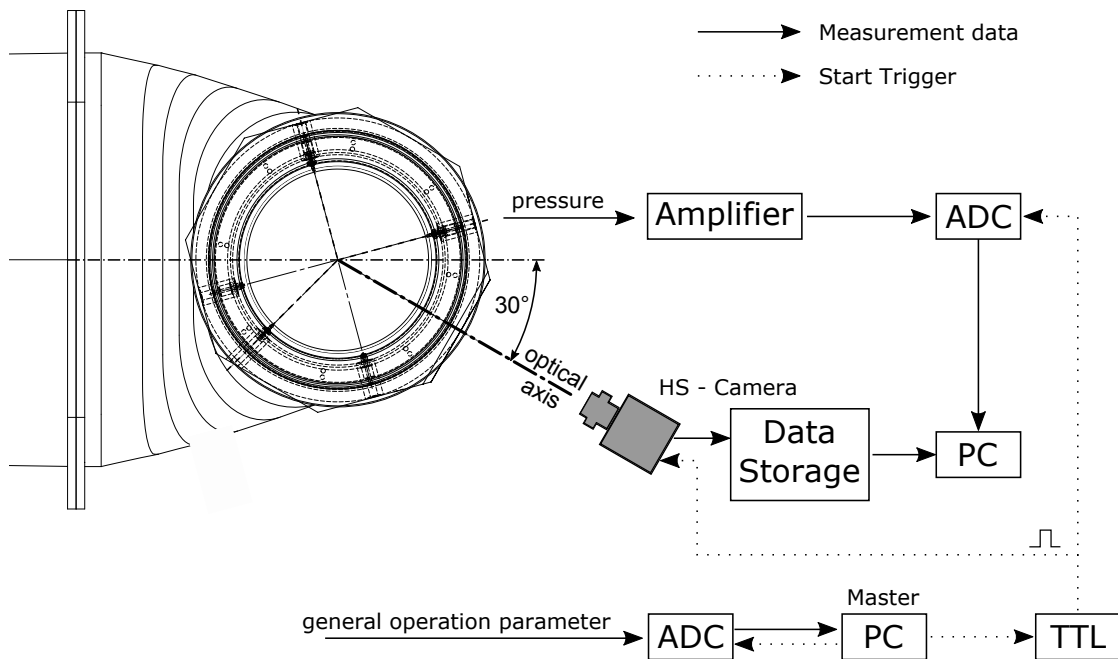

Figure 3.11: Schema of data acquisition chain and high speed camera arrangement

Table 3.4: Specifications of high speed camera

Sensor Resolution	1024 x 1024 pixels
Max. Frame Rate	2000 fps full frame
	170000 fps frame segment
Recording Color Depth	Monochrome; 12bit
Trigger Input Signal	TTL
Digital Interface	Gigabit Ether Port (1000BASE-T)

3.5   Measurement procedure

In the following chapter, the measurement procedure and data recording is described. Experiments are conducted under various operation conditions. Therefore the following parameters have been changed in course of presented investigation:

- Initial water level $E\kappa$: three different water levels are investigated. First is a typical water level $E1.00$. The second initial water level $E0.50$, which is $0.50D_2$ lower than the runner low pressure side, and third water level $E0.25$ - close to the runner.

- Direction of runner rotation: all measurements are conducted in both senses of rotation; meaning the runner rotating in turbine and pump rotation direction.

- Densimetric Froude number Fd: experiments are executed with various densimetric Froude numbers Fd - defined according to equation 2.12. Differences in definition of this dimensionless key figure should be explicitly noticed and are described in detailed in section 2.4.
  Generally Fd depends on geometrical dimension D_2, gravity constant g, the runner speed n and density ratio ρ_A/ρ_W, respectively pressure and temperature. The densimetric Froude number is set by variation of the runner speed n.
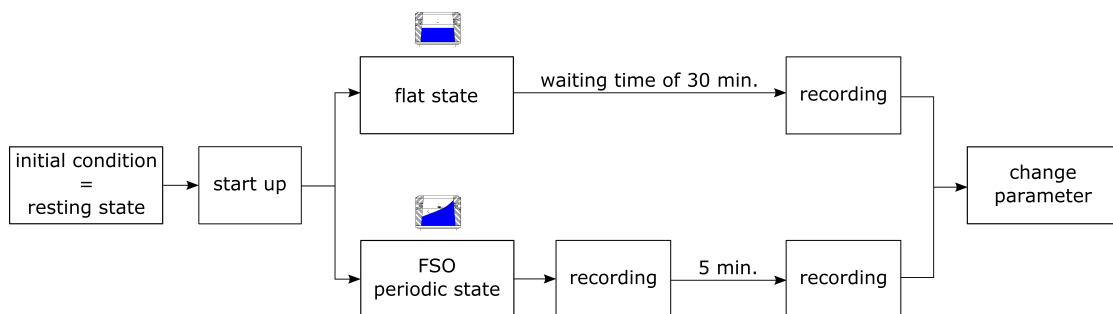

Figure 3.12: Schema of measurement procedure

The measurement procedure is illustrated in Figure 3.12. As initial condition the pressure and initial water level in the draft tube cone are set. Before machine

start up the whole test rig is in resting state. Referring on the one hand to the water volume and on the other hand to the steel structure and test facilities. For confirmation reasons one recording is done before the machine starts. During the start up the runner speed is increased with a fix ramp of 50 rpm per second to the first speed of interest for the investigations n_1. In the next step the behaviour of the free surface in the draft tube cone is observed. The start of observation is marked in Figure 3.12. Afterwards there are two possibilities: Either the free surface is staying in flat state or an oscillation of the free surface occurs.

- The first possible case is flat state:

  The water surface doesn't move in z-coordinate (direction of runner axis of rotation), but can be in rotation with angular velocity Ω_W. After a waiting time the recording of the general measurement parameters, the high speed camera recording and the pressure measurements using fast response pressure transducers is done. A waiting time of 30 minutes is defined to ensure free water surface staying in flat state and no free surface oscillation arises. The duration of waiting time was determined during pre-experiments and increased by a safety margin.

- The second and more interesting case is free surface oscillation:

  In this case free water surface is oscillating and an amplitude in direction of the runner axis of rotation can be observed. After reaching a periodic state, the recording of the general measurement parameters and synchronous starting high speed camera and pressure signal recording is conducted. Measurements are performed for all observed oscillations independent of the oscillation mode. Once first recording is completed, a similar recording is repeated after a waiting time of 5 minutes to confirm periodic state. The free surface oscillation is defined as periodic, if no changes in oscillation mode and amplitude A can be detected for a period of 60 seconds.

After this measurement cycle the runner speed is increased to the next speed of interest n_i. Depending on the occurring case, the measurement cycle starts again until the maximal runner speed of interest for the investigations n_{max} is reached. Afterwards the machine is shut down. After resting state is reached again, other initial conditions are adjusted and the whole measurement procedure starts again.

Recording: Basically one recording consists of three simultaneous measurements: the acquisition of general measurement quantities, the high speed video recording and the measurements of fast response pressure transducers, which are implemented at the draft tube cone. The main goals are firstly the optical detection of the amplitude A and secondly the identification and determination of the angular frequency ω_{FSO} of free surface oscillation in periodic state depending on the parameters listed at the beginning of this section.

When recording begins, data acquisition of general operation parameters starts first. General values, such as temperature or torque, are recorded for a period

of 60 seconds; time resolved as well as mean values. The instrumentation of all general measurement quantities is described in section 3.4.1.

The high speed camera recording and pressure measurements, done by means of fast response pressure transducers, are synchronised. Both acquisitions start with a delay of 10 seconds to general values. High speed camera recording is conducted with a frame rate of 250 frames per second. The pressure measurement has a sample rate of 400 samples per second and a duration of 50 seconds leading to a frequency resolution of 0.02 Hz at frequency spectrum. More detailed information and arrangement of the camera and the sensors is provided in section 3.4.4 and 3.4.3.

Detection of the frequency of free surface oscillation f_{FSO}**:** The frequency of free surface oscillation is identified by analysing the signals of fast response pressure transducers. Sensors are instrumented in different measurement levels and axis to detect pressure fluctuations in all areas. Including areas completely under water as well as those which are filled with air or transition areas. Transition areas are partly filled up with air and also reached by water surface. The implementation of sensors is described in detail in section 3.4.3.

Mentioned signals are transformed from time to frequency domain using *Fast Fourier Transformation* and the dominant peaks are identified. Determined angular frequencies are verified by a second method using optical evaluated signal of amplitude A. Therefore, the suitability to identify the frequency of free surface oscillation f_{FSO} is confirmed. Validation and results are described in section 4.3 and 4.2 in the next chapter.

Determination of free surface amplitude A**:** The determination of the amplitude A of free surface oscillation in periodic state is based on high speed video recording. Captured data are imported and used as input by a *LabView* program. Afterwards the images are overlayed by a coordinate system and rotational axis of symmetry is defined. In the next step the region of interest (ROI) for image analysing is specified. The high speed camera focuses on the front inner draft tube surface. The camera alignment is shown in Figure 3.11. Once the edge of water surface is specified, images are processed subsequently. The vertical movement is detected by tracking the edge of free water surface along the center line, which is projected on the focusing plane. An exemplary presentation is shown in Figure 3.13. By definition of ROI offset to coordinate origin z_{px1} is specified and has to be considered. The total coordinate z_{px} of the tracking point is the sum of z_{px1} and relative ROI coordinate z_{px2}.

$$z_{px} = z_{px1} + z_{px2} \tag{3.1}$$

The coordinate of the tracked point is saved for every image in pixel units and converted into, so called, *real world* coordinates by scaling factor known from calibration.
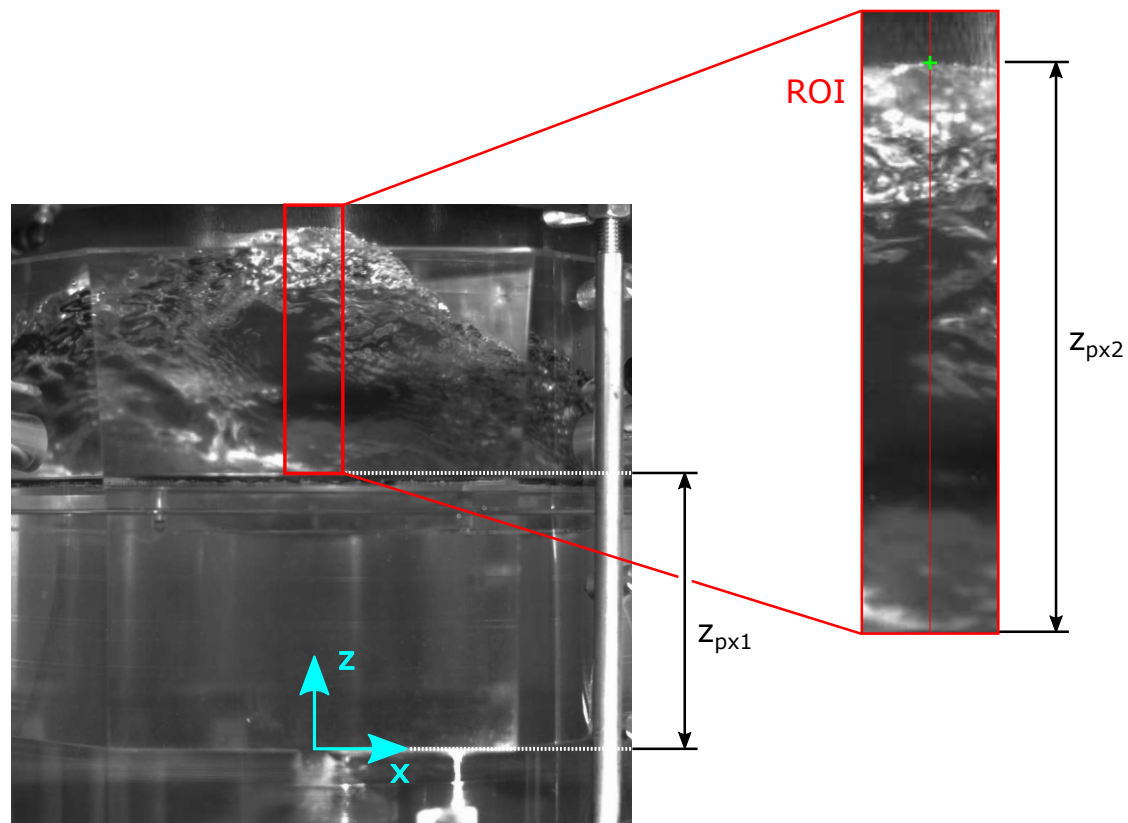
Figure 3.13: Illustration of optical amplitude determination

The amplitude of free surface oscillation A is determined by

$$A = z - z_{ini} \tag{3.2}$$

where z is the coordinate of tracked point z_{px} converted into *real world* unit and z_{ini} the coordinate of the initial water level.

Images are recorded with a frame rate of 250 fps and a resolution of 1024 x 1024 pixels. Assuming two rotations of free water surface per second (which is the expected speed range), 125 frames per revolution are recorded. As a result one image is taken every 2.88 degree of surface motion. More data of the high speed camera used are provided in section 3.4.4 and the measurement uncertainties are discussed in section 3.6.

The output of described procedure is the development of free surface oscillation amplitude A in time domain from the point of view as fixed observer in stationary frame of reference. As a result the maximum amplitude is determined for different initial water levels $E\kappa$, direction of runner rotation and Fd. Experimental results are presented in chapter 4.

3.6   Measurement uncertainties

All experimental results presented in the following chapter 4 are subject to uncertainty. The calculations are carried out in accordance with [16]. Theoretical considerations and definitions regarding the measurement uncertainty are mentioned in previous section 2.5.
Table 3.5 shows the maximum measurement uncertainties of determined quantities belonging to the free surface oscillation.

Table 3.5: Measurement uncertainties of measured quantities and calculated values

p_{DT} (bar)	θ_A (°C)	θ_W (°C)	ρ_A % of value	ρ_W % of value	n (rpm)	Fd % of value
0.0095	0.40	0.18	0.96	0.95	0.80	0.96

One measured quantity, which is not listed, is the detected amplitude of the free surface oscillation A, respectively the reached water level. In order to be able to make an assessment of the measurement uncertainty of A the uncertainty of surface edge detection has to be estimated. The conversion factor is known from in situ calibration and is between 0.229 and 0.303 millimetres per pixel. Assuming a conservative value of 10 pixels for the uncertainty of the surface edge detection results in a maximum measurement uncertainty $u_A = 3.03mm$. The uncertainty of the detected and normalized measurement values is

$$\frac{u_A}{D_2} = 0.011 \tag{3.3}$$

The frequency of the free surface oscillation is determined by analysing the signal of the fast response pressure transducers. The peaks are detected by applying Fast Fourier Transformation. The resolution of the processed frequency spectrum and consequently the measurement uncertainty of the frequency detection is 0.02 Hz .

CHAPTER 4

Experimental results

Chapter 4 deals with the results of the conducted model tests. All experiments are executed at the hydrodynamic laboratory of the Institute of Energy Systems and Thermodynamics.

First of all the behaviour of the free surface motion at the draft tube is described in a qualitative way. The results concerning the amplitude of the free surface oscillation are presented afterwards. They are illustrated for each initial water level in a dimensionless way. After comparing two detection methods, the determined frequencies of the free surface oscillation f_{FSO} in final periodic state are illustrated. Resulting characteristic and trend lines are also depicted. Next the signal characteristics are mentioned, which are described by means of some examples. Measurements with draft tube cone 2 are conducted and presented for comparison reasons as well. Finally the influence of the changed parameters are listed and summed up.

4.1 General behaviour

During its formation the observed free surface oscillation at the draft tube cone passes through several states. Starting with flat state and passing through transition states, the free surface oscillation ultimately reaches a final periodic state with an azimuthal wave number $m = 1$. Some transition states are periodic states too. Hereinafter the wording free surface oscillation stands for the final periodic state with $m = 1$ unless otherwise explicitly stated.

In section 4.4 Amplitude of the free surface oscillation the elevation of the free surface motion is presented, including even transition states. They are noticeable in Figure 4.9 at the range of densimetric Froude number $Fd = 0.12$ to 0.2 for example. Especially at these transition ranges the general behaviour of the free surface may vary. In addition, a hysteresis is observed during shut down, caused by mass inertia. The sense of rotation of the water surface is independent from the state of motion and is observed to be equal to the runner rotation direction.

Depending on the densimetric Froude number, runner rotation direction and the initial water level the shape of water surface even changes at final state. The free surface oscillation is smooth at relatively low densimetric Froude numbers Fd and initial water level $E1.00$. It becomes rougher the higher Fd and the initial water level gets. Furthermore, breaking of the surface crest as well as changes in the size of air bubbles in the water occurs. At high densimetric Froude number and increasing initial water level water droplets break away from the free surface oscillation and may hit or enter the runner. In addition, an increasing amount of water spray is recognized in the air. A qualitative categorization of these conditions is tried in [47]. The behaviour of the free water surface is categorized into 4 stages. These stages depend on the motion of the free surface, the roughness of the surface, the ratio of water drops in the air and air bubbles in the water flow. The described stages have been observed at present investigations as well.

4.2 Signal characteristics

Subsequently the characteristics of the free surface elongation signals and pressure signals are explained. They are used for the detection of the amplitude and the frequency of investigated free surface oscillation.

The elongation signals of the free surface oscillation are determined by means of high speed recordings. The measurement equipment, setup and procedure are described in sections 3.5 and 3.4. Two examples are illustrated at Figure 4.1 and 4.2. Presented signal paths show the motion of the free surface waterlevel normalized by the runner low pressure side diameter D_2. According timescale is displayed in seconds.
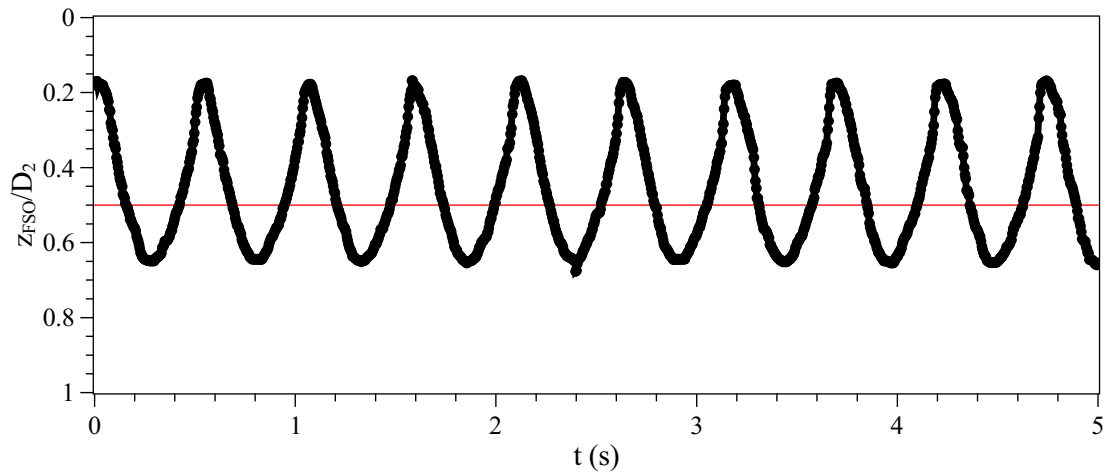
Figure 4.1: Signal of free surface oscillation (Tu - $E0.50$; $Fd = 0.214$)

As one can see, the free surface oscillation is periodic. Depicted horizontal red line symbolizes the initial water level. Hence the asymmetry of water propagation in vertical direction (z-axis) is clearly recognizable. The increase of water level due to the oscillation of free surface is higher than the decrease. This is caused by the conical shape of the draft tube, by the rotation of water and centrifugal forces. The increase of the free surface motion is steeper than the decrease. Generally, it can be noticed that the troughs are wider than the peaks and the main shape of the motion is reproduced by the signal very well.
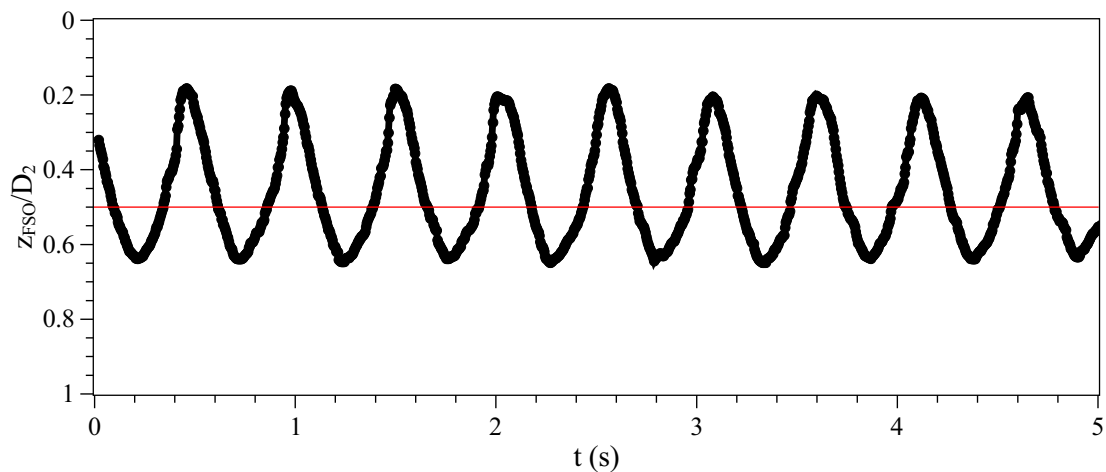

Figure 4.2: Signal of free surface oscillation (Tu - $E0.50$; $Fd = 0.275$)

Figure 4.1 shows the signal of the free surface motion for an initial water level $E0.50$, densimetric Froude number $Fd = 0.214$ and runner rotating in turbine rotation direction. Almost none deviation of maximum reached water level is detected. In contrast, at Figure 4.2 a variation of maximum reached water level is present - even if not very minted. The regarding free surface oscillation occurs at $Fd = 0.275$ with the same initial water level and sense of rotation.

An exemplary frequency spectrum of pressure signals at measurement levels $E0.10$, $E0.25$, $E0.75$, $E1.00$ and $E1.40$ is illustrated in Figure 4.3. Each signal is normalized by its corresponding maximum amplitude. The pressure signals are detected for runner rotating in turbine rotation direction at a densimetric Froude number $Fd = 0.214$ and an initial water level $E0.50$. The resolution of presented spectrum is $0.02Hz$.
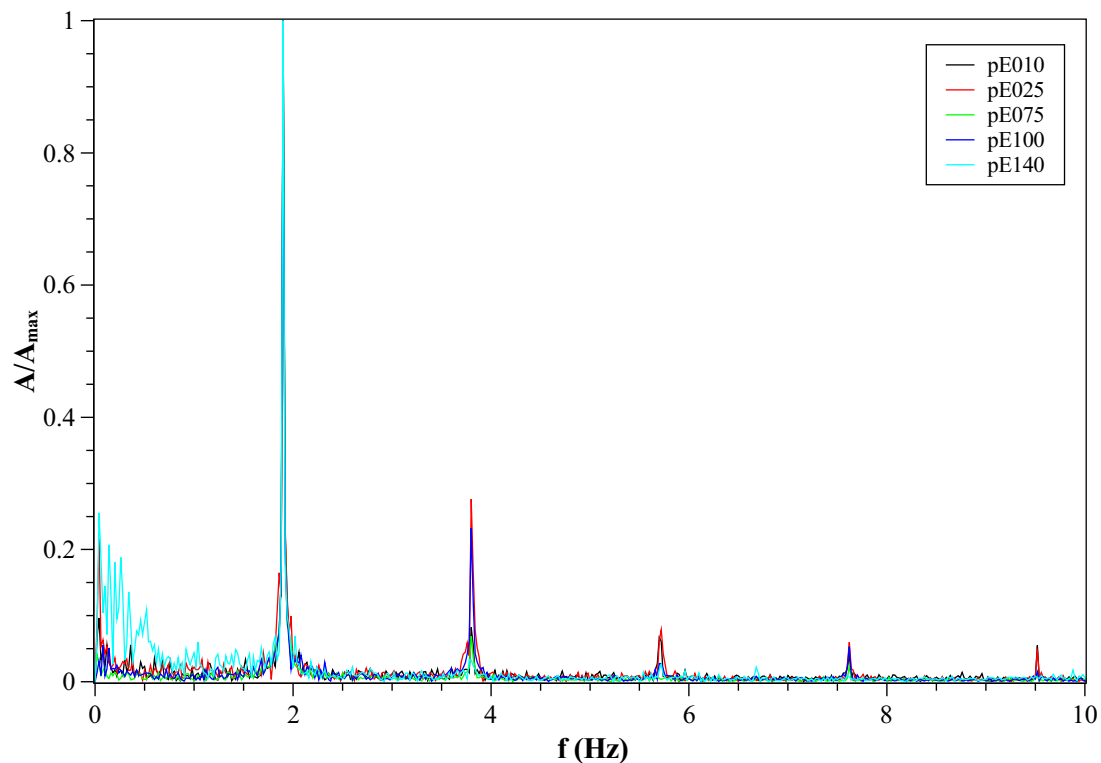

Figure 4.3: Normalized frequency spectrum of pressure signals (Tu - $E0.50$; $Fd = 0.214$)

A very clear and well defined dominant peak is detected at a frequency of $f = 1.9Hz$. This peak is caused by the free surface oscillation. The other illustrated peaks are caused by harmonic frequencies.
Aforesaid dominant peak is detected at all measurement levels independent of the

fluid. It is detectable in air and in water, as well as at region of mixed or changing fluid. Measurement level $E1.40$ is the deepest one, but the frequency of free surface oscillation is even detected at this level. Only the amount of lower frequency ranges is a bit more remarkable, possibly due to vibrations or influence of the tailwater.

Two exemplary pressure signals of the fast response pressure transducers are presented in Figure 4.4. The transducers are mounted in primary axis I at measurement levels $E0.25$ and $E0.75$. The illustrated signals are detected with an initial water level $E0.50$ at the same conditions as previously described frequency spectrum (see Figure 4.3). The signal is normalized by its mean value and a time period of 10 seconds is illustrated.
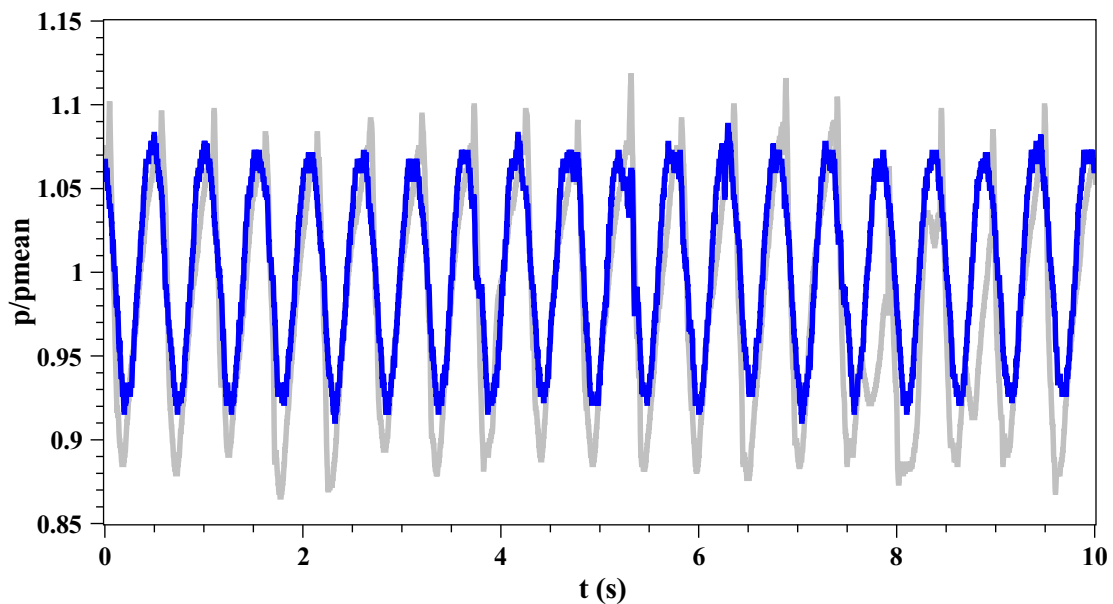
Figure 4.4: Normalized pressure signal at $E0.25$ (gray) and $E0.75$ (blue)

The frequency of the free surface oscillation is clearly determinable by means of shown signals. But actually it is not possible to determine the amplitude of the free surface oscillation directly by using the pressure signal. As already pointed out in Figure 4.3 the detected frequencies are similar and independent of the measurement level. The determined amplitude of the pressure signal is a little higher for transducer positioned at $E0.25$.

A comparison of pressure signals and elongation signal of the free surface motion is provided in Figure 4.5. The illustrated measurement results are for runner rotating in turbine sense of rotation at $Fd = 0.214$ and initial water level $E0.50$. The normalized pressure signals are the same as in Figure 4.4. A shift of phase

is noticeable between the pressure signals and the presented free surface motion recorded by the high speed camera. This is caused by the angular offset between non-invasive measurement axis and primary pressure transducer axis I. The alignment of high speed camera and pressure transducers is shown in Figure 3.11 and 3.10. The coherence of the pressure signals and the elongation signal of water level motion is corroborated.
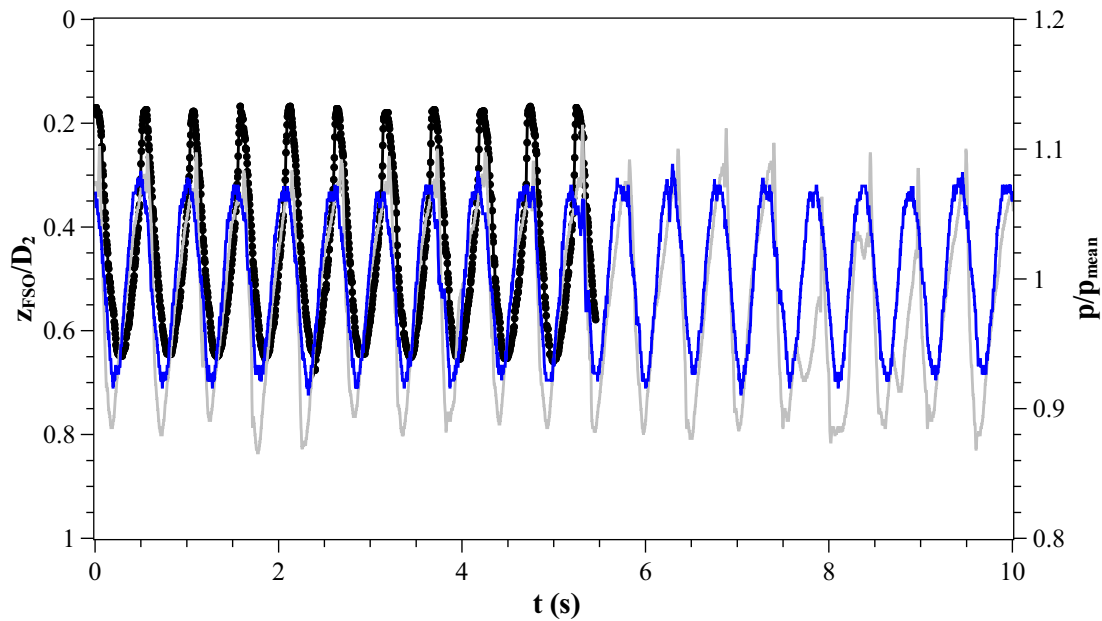
Figure 4.5: Pressure signals at $E0.25$ (gray) and $E0.75$ (blue) compared with elongation of free surface oscillation

The measured signals of the shaft torque do not show any specificity. Frequency analyses show no dominant peaks and no fluctuations are detected in an unusual amount. Due to the machine setup no hydraulic flow phenomena occur at the high pressure side. However, there is no influence of the free surface oscillation on the shaft torque signal identified by executed investigations.

4.3   Frequency of the free surface oscillation

The frequency of the free surface oscillation f_{FSO} is important for characterisation, identification and understanding of this phenomena. Measurements provide a basis for the analytical interpretation (see 5 Analytical modelling) and first applicable laws can be determined.

The draft tube cone of the model machine is equipped with fast responding piezoresistive pressure transducers described in detail in section 3.4 Instrumentation. In order to determine f_{FSO}, the pressure signal in time domain is transformed into frequency domain by means of FFT. An exemplary diagram is shown in Figure 4.3 with runner rotating in turbine rotation direction $Fd = 0.214$ and initial water level $E0.50$. A very dominant peak can be identified at a frequency $f \approx 1.9 rad/s$ which is caused by the free surface oscillation. The other represented peaks are caused by harmonic frequencies.

The frequency of the free surface oscillation is also determined by using high speed camera recordings. This is done for some parameter settings to validate the previous described method, extracting the information f_{FSO} out of the pressure signal. As described in section 3.5 Measurement procedure the high speed camera recordings are post processed. Hence the recording is analysed and the timestamp t_i for each detected free surface peak in one recording is calculated for $i = 1...m$. i is the number of each free surface oscillation peak and m the total amount of peaks in related recording. The timestamp of each peak is calculated by

$$t_i = \frac{N_i}{R_{fps}} \tag{4.1}$$

where N_i is the number of the frame and R_{fps} the frame rate of the recording in frames per second. The frequency f_{FSOopt} determined by the optical method is the mean value of all inverse of periodic times T_j

$$T_j = t_{j+1} - t_j \tag{4.2}$$

$$f_{FSOopt} = \frac{1}{n} \sum_{j=1}^{n} T_j^{-1} = \frac{1}{n} \sum_{j=1}^{n} t_{j+1} - t_j^{-1} \tag{4.3}$$

for $j = 1...n$ with number of periodic times $n = m - 1$, respectively the number of angular frequencies or resulting time steps.
The results of both methods are compared and exemplarily shown at Figure 4.6 for initial water level $E.50$ and runner rotating in pump rotation direction. As one can see the frequencies of both methods match well. Therefore, by pressure signal and FFT determined frequencies are confirmed as frequencies of the free surface

oscillation f_{FSO}. Furthermore, the pressure signal method (method 1) avoids large deviations due to irregularities on the water surface as shown in the diagram at $F_d \approx 0.33$.
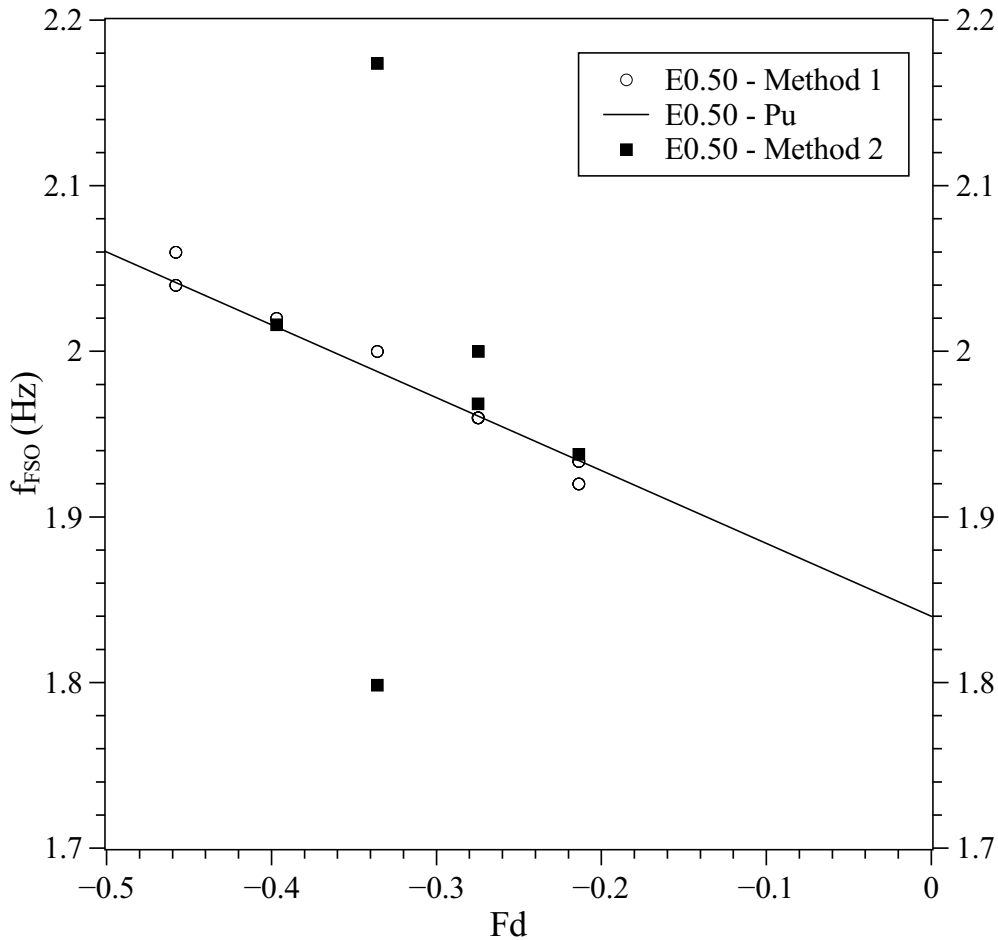

Figure 4.6: Exemplary comparison of detected frequency by means of method 1 (pressure signal) and 2 (optical) for initial water level $E0.50$

Figure 4.7 visualizes the results for the initial water levels $E0.50$ and $E1.00$. The frequency of the free surface oscillation is plotted on the ordinate and related densimetric Froude number Fd on abscissa. Positive values are arranged on top abscissa with runner rotating in turbine rotation direction ($Fd > 0$). In pump rotation direction negative values of Fd are plotted on bottom abscissa. This means that the results for $Fd < 0$ are applied inversely and superimposing the results for $Fd > 0$. The frequencies of free surface oscillation are identified by means of pressure measurements and FFT.
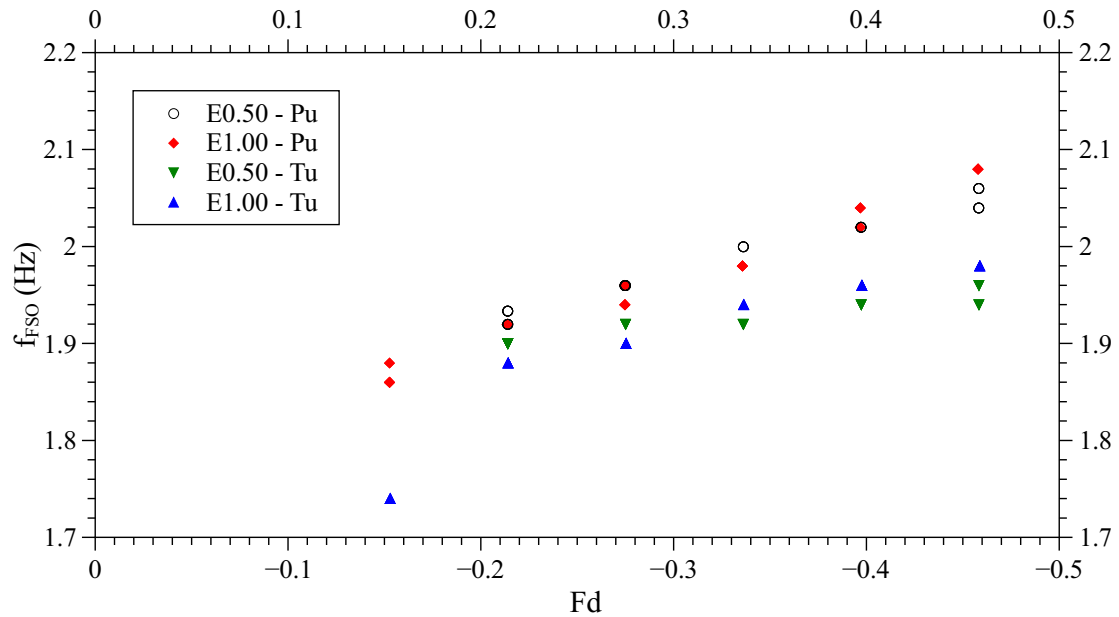
Figure 4.7: Determined frequency of free surface oscillation

Table 4.1: Intersection points and gradients of regression lines

	Pump	Turbine
	intersection point (Hz)	
E0.50	1.84	1.84
E1.00	1.77	1.78
	gradient of regression line	
E0.50	0.44	0.26
E1.00	0.66	0.44

An increase of the absolute value of densimetric Froude number $|Fd|$ results in an increasing frequency f_{FSO}. This correlation can be seen for all initial water levels and does not depend on the direction of runner rotation.

Following influence of the runner rotation direction can be recognized: f_{FSO} reaches higher values if runner rotates in pump rotation direction (E0.50-Pu and E1.00-Pu) than in turbine rotation direction.

Determined frequency shows a linear behaviour as pointed out by the regression lines illustrated in Figure 4.8. The extrapolation of the curves to $Fd = 0$ meet at the same intersection point for both rotation directions, but they depend on the initial water level. However this point is only theoretical, this is a very interesting fact which will be further discussed in chapter 5 Analytical modelling. The point of intersection with an initial water level $E0.50$ is clearly higher than with an initial water level $E1.00$. In contrast, the gradient of regression line is larger for $E1.00$ than $E0.50$. Furthermore the gradient depends on the direction of runner rotation. It is smaller with runner rotating in turbine rotation direction ($Fd > 0$) than for $Fd < 0$. All gradients and intersection points are listed in Table 4.1.
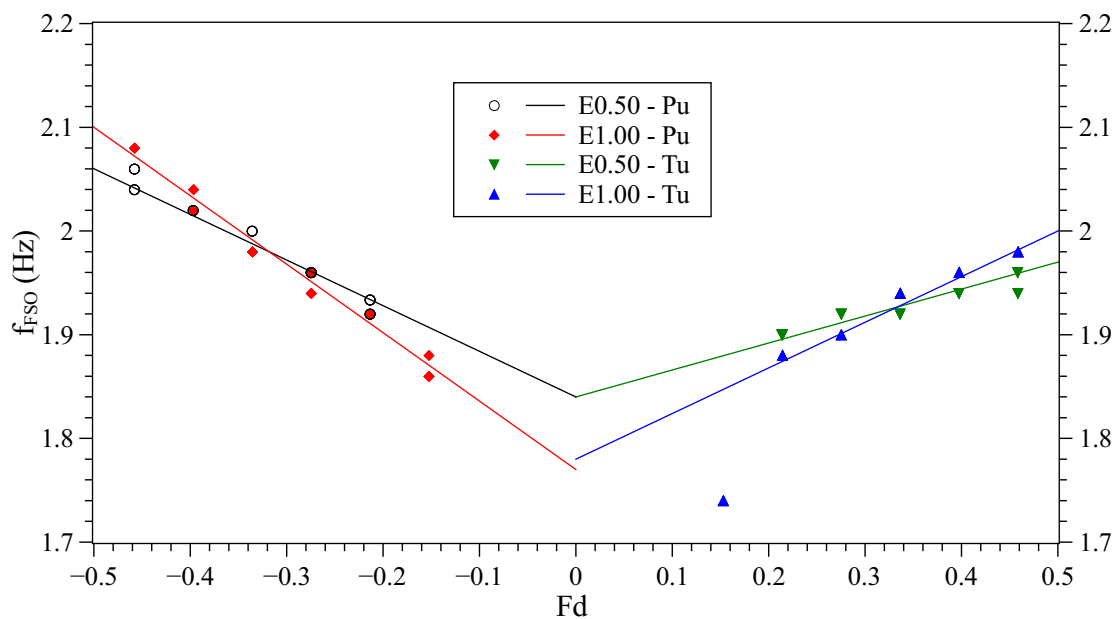

Figure 4.8: Frequencies of free surface oscillation and regarding regression lines

4.4   Amplitude of the free surface oscillation

The amplitude of the free surface oscillation A is the difference between the highest peak and the initial water level $E\kappa$ as defined in section 3.3 Experimental modelling (relations and simplifications). The highest peak respectively the highest reached level of water formation is determined optically (see 3.5 Measurement procedure). Therefore, high speed recordings are post-processed and analysed by using a *LabView* based program. The arrangement, technical data of the high speed camera and experimental setup is described in previous section 3.4 Instrumentation. Measurements are conducted with different densimetric Froude numbers Fd, three initial water levels ($\kappa = 0.25, 0.50$ and 1.00) and with runner rotating in turbine as well as in pump rotation direction.

The results are delineated in Figure 4.9 with amplitude A normalized by the runner low pressure side diameter D_2 as ordinate and corresponding densimetric Froude number Fd as abscissa. A negative speed n indicates runner rotating in pump rotation direction as defined in section 3.3 Experimental modelling (relations and simplifications). Due to this agreement and definition of Fd according to equation 2.12 the results for runner rotating in turbine rotation direction are shown at positive densimetric Froude number $Fd > 0$. At $Fd < 0$ the results for runner rotating in pump direction are illustrated.
For each measurement the mean value of all detected peaks per recording are calculated. Hence all presented measurement points are mean values of one recording and illustrated error bars correspond to the regarding standard deviation.

Generally the amplitude of the free surface oscillation increases with decreasing initial water level $E\kappa$. In other words the amplitude correlates to the difference between the runner low pressure section and the initial water level. As apparent from Figure 4.9 the amplitude reaches values between $0.4D_2$ and $0.7D_2$ with initial water level $E1.00$ (bottom graph). At $E0.25$ (top graph) the maximum amplitude is slightly higher than $0.2D_2$. Overall the amplitudes for same initial water level are in a similar range for both directions of runner rotation or maybe a little higher if the runner rotates in pump rotation direction.

In Figures 4.9 and 4.10, showing the results of different $E\kappa$, a region without free surface oscillation can be observed - so called flat state (see section 3.5 Measurement procedure). At these densimetric Froude numbers the water surface is in simple rotation and no oscillation is excited.

With runner rotating in pump rotation direction ($Fd < 0$), the shift between flat state and free surface oscillation is sharply delimited. In contrast a transition range can be observed for runner rotating in turbine rotation direction ($Fd > 0$). This applies to experiments conducted with initial water level $E0.50$ and $E1.00$.

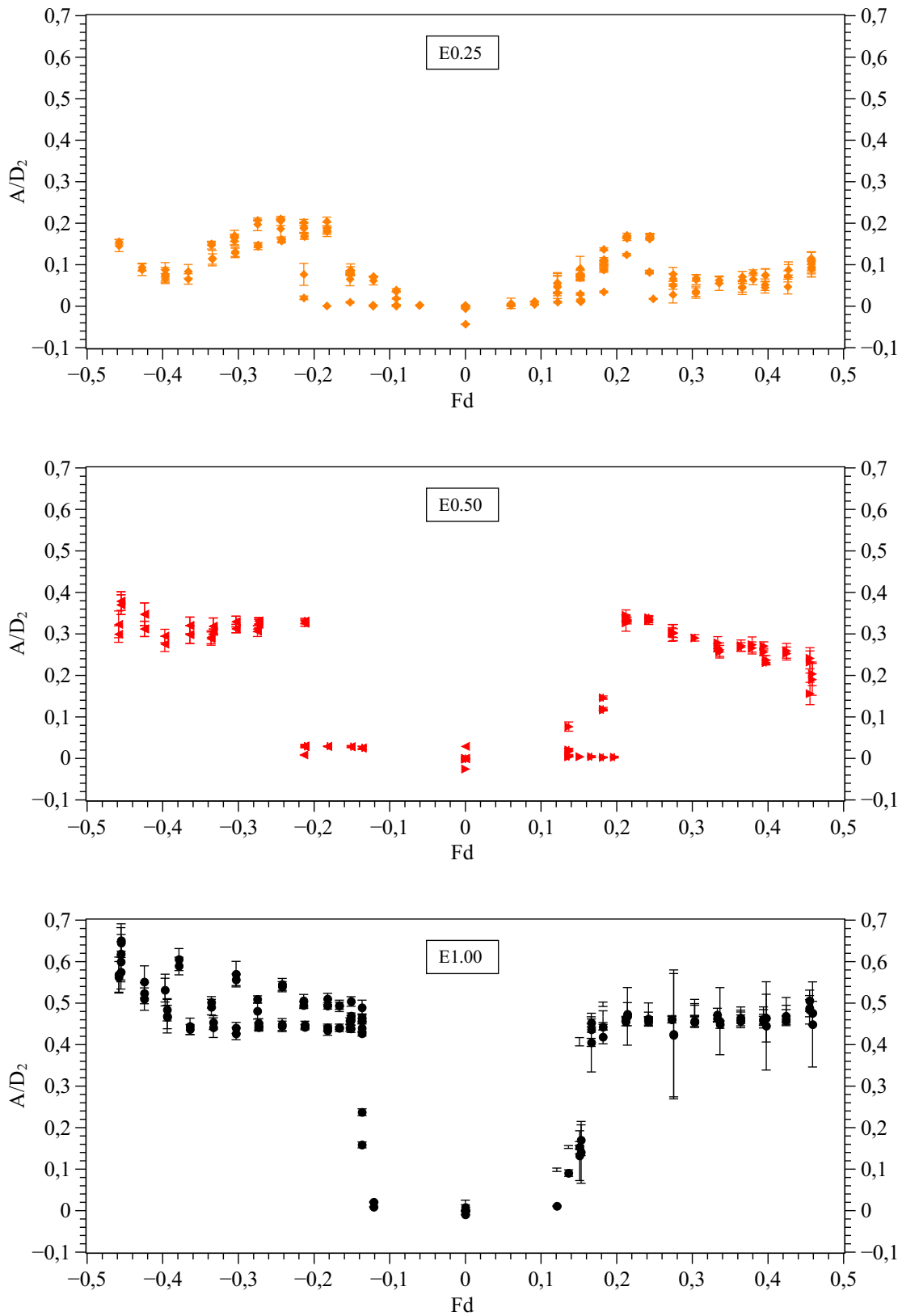Depending on initial water level and runner rotation direction a critical densi-

Figure 4.9: Normalized amplitude A of free surface oscillation as function of Fd with initial water level $E0.25$ (top), $E0.50$ (middle) and $E1.00$ (bottom)

metric Froude number Fd_{crit} can be identified for the investigated model machine. Critical densimetric Froude number tends to be greater the higher the initial water level $E\kappa$ is; with exception of $E0.25$. The results for this high initial water level show a wide transition zone starting at relatively low densimetric Froude number. This specificity is caused by small distance between the runner and the free surface oscillation and therefore boundary layers of base flows are close together. Transition area is discussed in section 4.1 General behaviour as well.

If $|Fd| > 0.22$, free surface oscillation occurs independent of $E\kappa$ and the runner rotation direction.

The curve characteristics show a different behaviour at the investigated water levels and the direction of runner rotation.

For densimetric Froude number $Fd > 0$ at initial water level $E1.00$ the amplitude of the free surface oscillation is nearly constant. A maximum in the range of $|Fd| = 0.2$ to 0.25 can be identified in both directions of runner rotation for initial water level $E0.50$ and $E0.25$. After this maximum an amplitude decrease can be clearly observed at $E0.50$ with runner rotating in turbine rotation direction ($Fd > 0$). The other three curves decrease after a local maximum, but seem to increase at higher Fd. For runner rotating in pump rotation direction ($Fd < 0$) at initial water level $E1.00$ the amplitude of the free surface oscillation is even slightly increasing. A decrease of amplitude as observed at $E0.50$ and $Fd > 0$ can be found in literature [57] for related water level.

The practical significance of the various reached levels of the free surface oscillation is pointed out by Figure 4.10. In these graphs the maximum reached free surface oscillation level is identifiable. z_{FSO} is the shortest distance measured from the runner low pressure side plane to the highest point reached by free water surface oscillation, as depicted in Figure 3.6. It is plotted on the ordinate normalized by runner low pressure side diameter D_2. Corresponding densimetric Froude number Fd is plotted on the abscissa. The rotation direction of the runner and the initial water level assignment are similar to Figure 4.9.

Nevertheless, the initial water level $E1.00$ results in highest amplitudes. The difference between the top peak of free surface oscillation and the runner low pressure side plane is the largest one, compared to other investigated initial water levels; as shown in Figure 4.10.

As identifiable the distance between the runner low pressure side and the peak of free surface oscillation decreases with increasing initial water level. However, a contact between the free surface oscillation and the runner is not determined. This is justifiable because amplitude A corresponds to κ and decreases too. Even with a level $E0.25$ the water peak doesn't reach the level of runner low pressure side D_2 ($\kappa = 0$). It should be noted at this point that even if the water shape is ruptured, the measured point is the highest point reached by water. This may
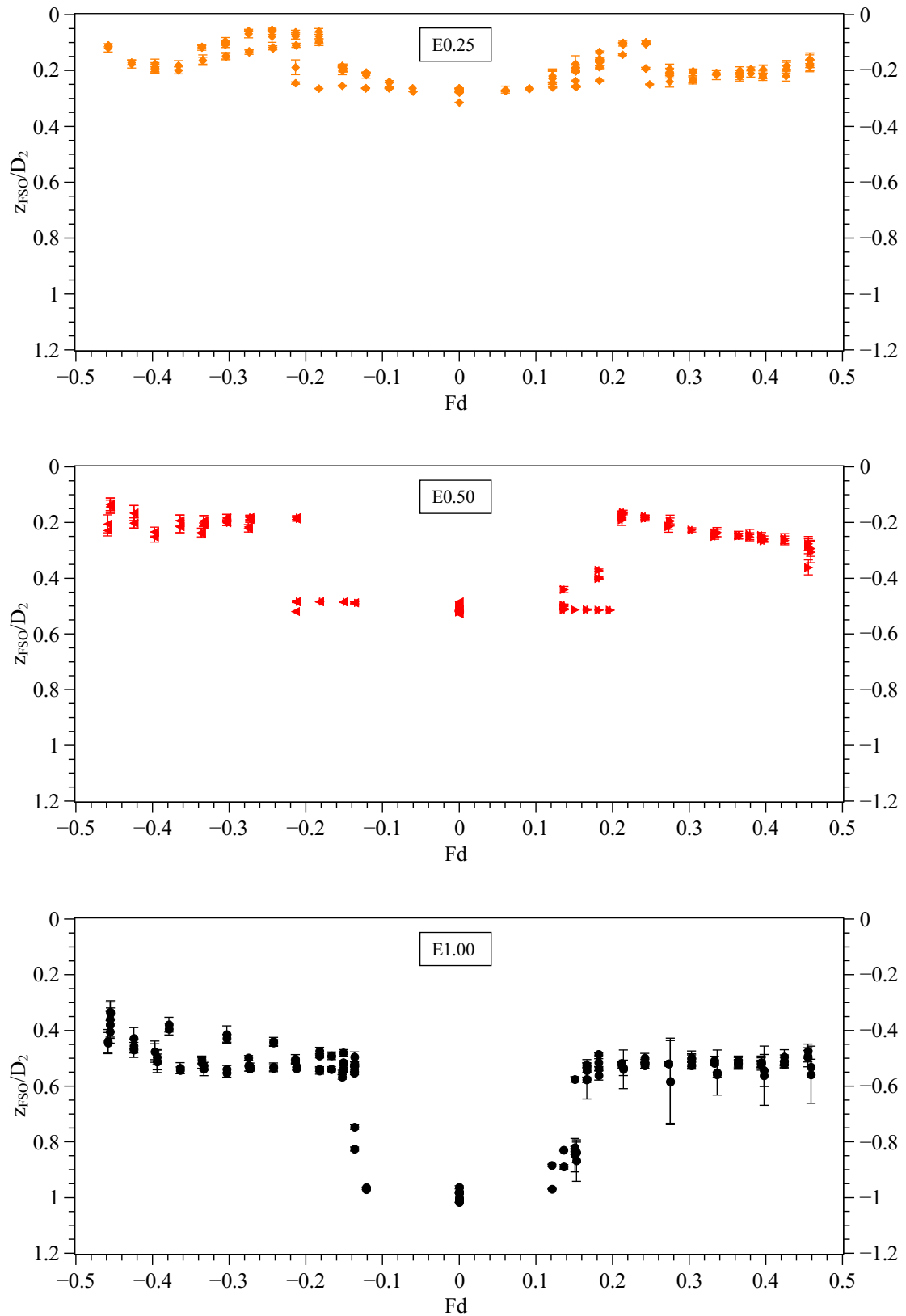
Figure 4.10: Normalized distance z_{FSO} as function of Fd with initial water level $E0.25$ (top), $E0.50$ (middle) and $E1.00$ (bottom)

cause the observed increase of some curves at higher densimetric Froude number; for example at $E0.25$. Unsnapped water drops are not mentioned in the measurement. Especially at higher densimetric Froude numbers water droplets break away (see section 4.1 General behaviour) and may hit the runner.

The curve characteristics, general behaviour and relations to Fd illustrated in Figure 4.10 are of course the same as explained and delineated in Figure 4.9. The maximum reached free surface oscillation level is in a similar range for $E0.25$ and $E0.50$ as presented in Figure 4.11. Especially if the runner rotates in turbine rotation direction ($Fd > 0$) no essential difference in maximal by free water surface reached level is achieved by lowering the initial water level from $E0.25$ to $E0.50$. At current state of investigation there is no need to lower the initial water level beneath $E0.25$ under the point of view about the maximum reached water level and the amplitude of free surface oscillation.
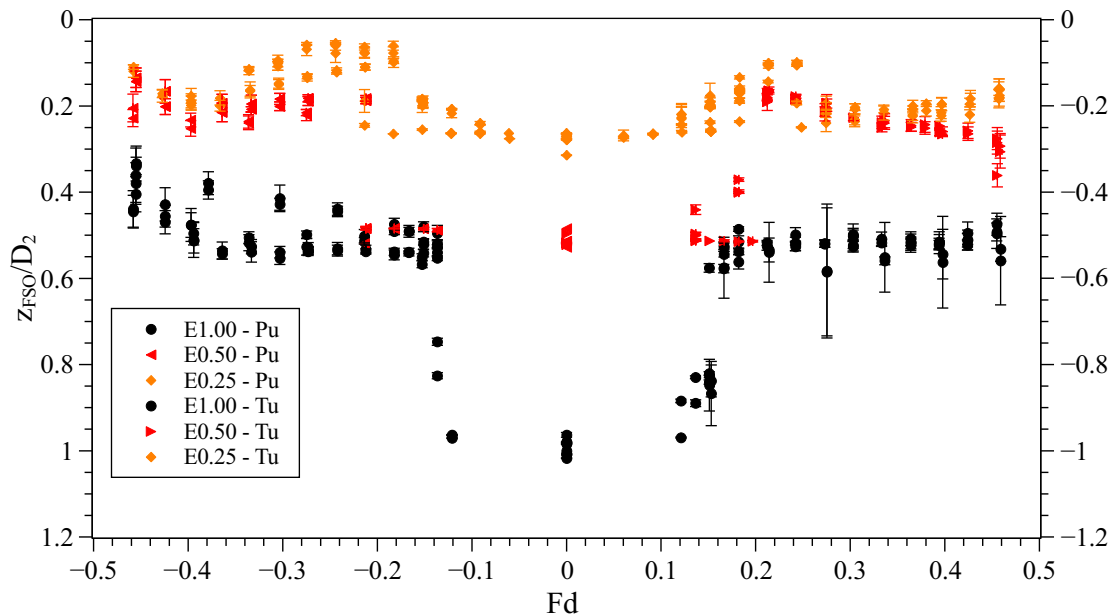
Figure 4.11: Normalized distance z_{FSO} as function of Fd - Comparison of investigated initial water levels

At Figure 4.12 the distance between the highest point of free surface oscillation and the runner low pressure side is illustrated in relation to the initial water level $E\kappa$. The presented points are mean values of all detected amplitudes for one initial water level, one direction of runner rotation and $Fd > Fd_{crit}$. The error bars visualize the standard deviation of the values.

The mean value of the shortest distance between runner low pressure side and highest point reached by the water surface $z_{FSOmean}$ correlates to the initial water level and a quite simple relation between these two parameters is noticeable. In a

rough approximation the illustrated distance is half as big as κ.
As already mentioned the distance z_{FSO} and respectively $z_{FSOmean}$ is higher for runner rotating in turbine rotation direction.

Figure 4.12: Mean values of normalized distance z_{FSO} in dependency of initial water level $E\kappa$
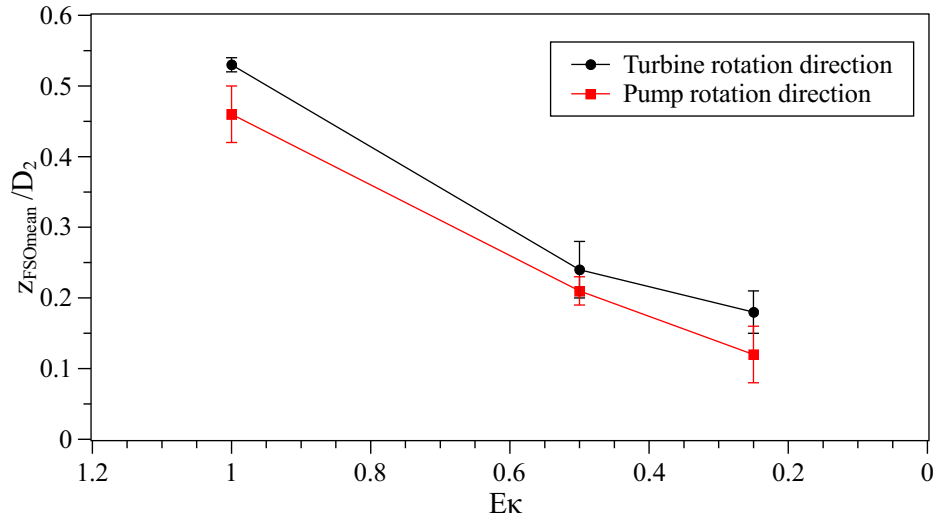
4.5   Measurements at draft tube cone 2

Vibrations of the draft tube wall are often presumed as excitation mechanism and reason for free surface oscillation. The following measurements shall achieve a contribution to this topic. Furthermore, additional parameters like draft tube material and wall condition are more similar to the prototype than draft tube cone 1 which is made of acrylic glass.

First of all, comparative experiments are executed with draft tube cone 2 mounted. The geometry of cone 2 is equal to cone 1, but it is made of steel. Further details about cone 2 are provided in chapter 3.
These measurements have been conducted at three different densimetric Froude numbers Fd and two initial water levels $E\kappa$ to ensure similarity of free surface oscillation. Same measurement procedure and modalities are used as for measurements with draft tube cone 1. They are described in section 3.3 and 3.5. The frequencies f_{FSO} and amplitudes A match very well as delineated by Figure 4.13. Thus, both cones lead to the same results and there is no recognizable influence of cone material. This reinforces also previous investigations with draft tube cone 1.

(a) f_{FSO} compared with cone 1 (E0.50)

(b) f_{FSO} compared with cone 1 (E1.00)

(c) z_{FSO} compared with cone 1 (E0.50

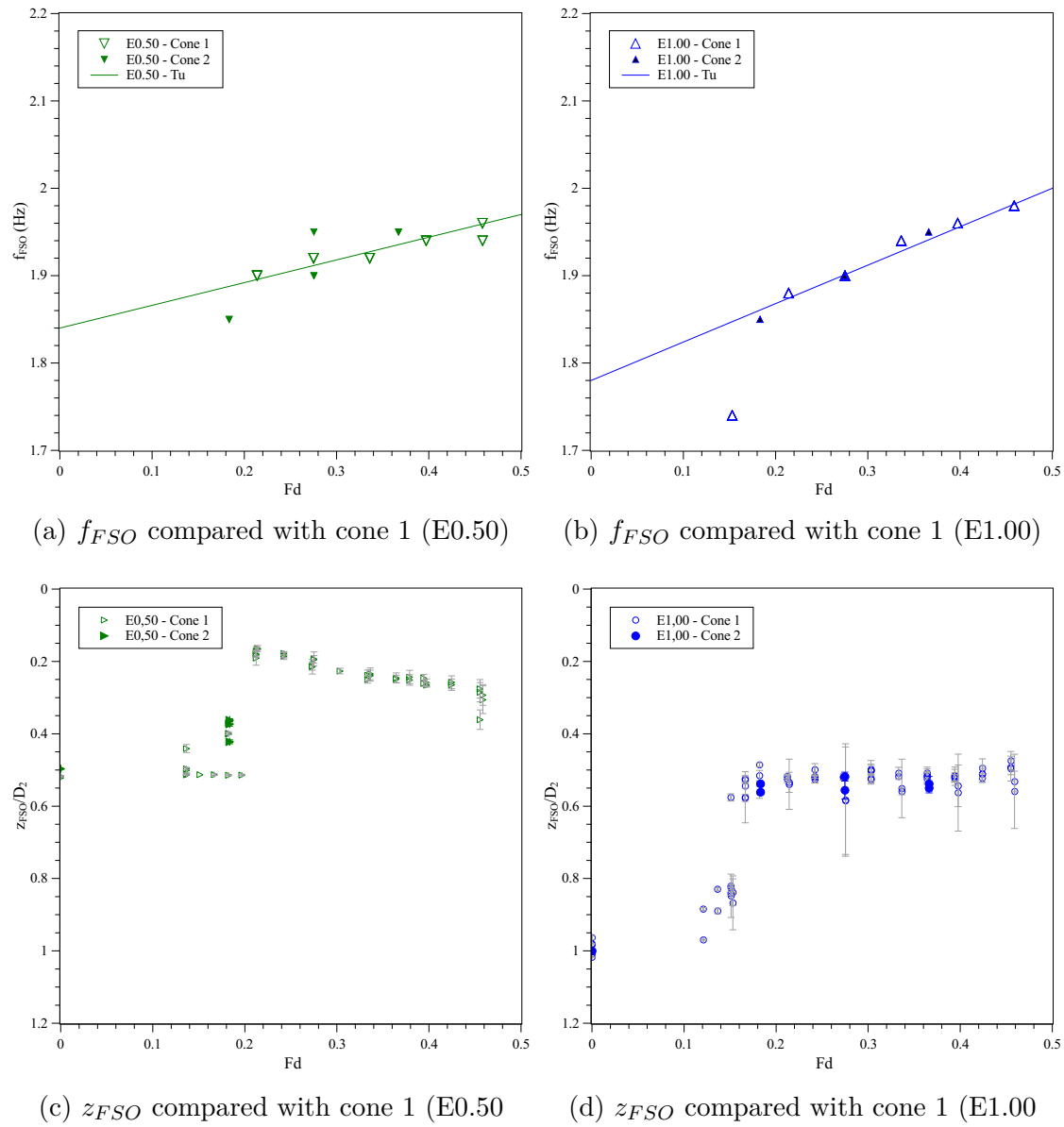(d) z_{FSO} compared with cone 1 (E1.00

Figure 4.13: Comparison of results for draft tube cone 1 and 2

In the next step draft tube cone 2 is modified by adding a 3mm steel plate. Hence runner and draft tube are fluidic uncoupled. A cross section of the runner and the draft tube cone region is illustrated in Figure 4.14. The steel plate is flush mounted at the top of cone 2. It is pegged at four points evenly spaced around the circumference and sealed by silicon. This is done to prevent flow interactions and fix the plate but do not force too much changes in structure.
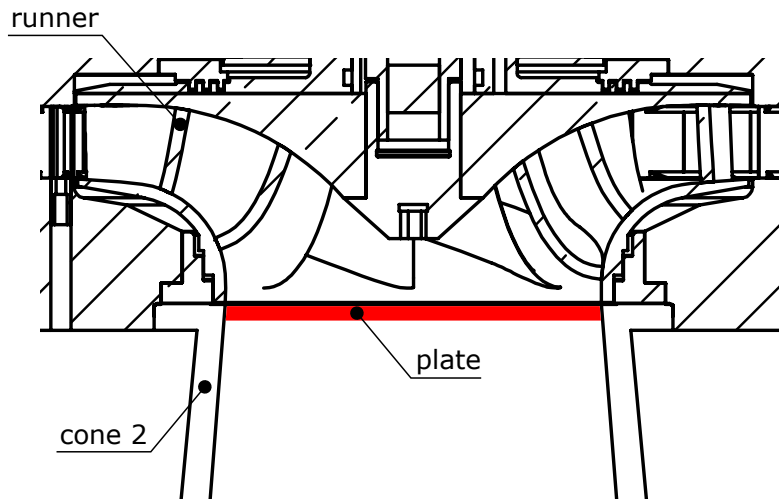
Figure 4.14: Draft tube cone 2 with mounted steel plate

Afterwards measurements are conducted with modified draft tube cone 2 under same conditions as competitive experiments. They are carried out to investigate or delimit the influence of draft tube wall and structure vibrations.

Figure 4.15 shows a visual comparison of the unmodified (top) and modified, respectively closed draft tube cone 2 (bottom). On the left side the runner stands still ($Fd = 0$) and the whole test rig is in resting state. Images on the right side display the free surface behaviour with runner rotating in turbine rotation direction and $Fd = 0.22$. As easily recognizable no free surface oscillation occurs at closed draft tube cone (bottom-right). Not even small air bubbles at the wall are in motion or moving. The results are the same for all investigated initial water levels and densimetric Froude numbers. Without fluidic connection between runner and draft tube no free surface oscillation appears. Summing up, free surface oscillation is apparently not induced due to wall vibrations. Due to this experiment the excitation seems to stem from the runner region and its origin is of a fluidic nature.
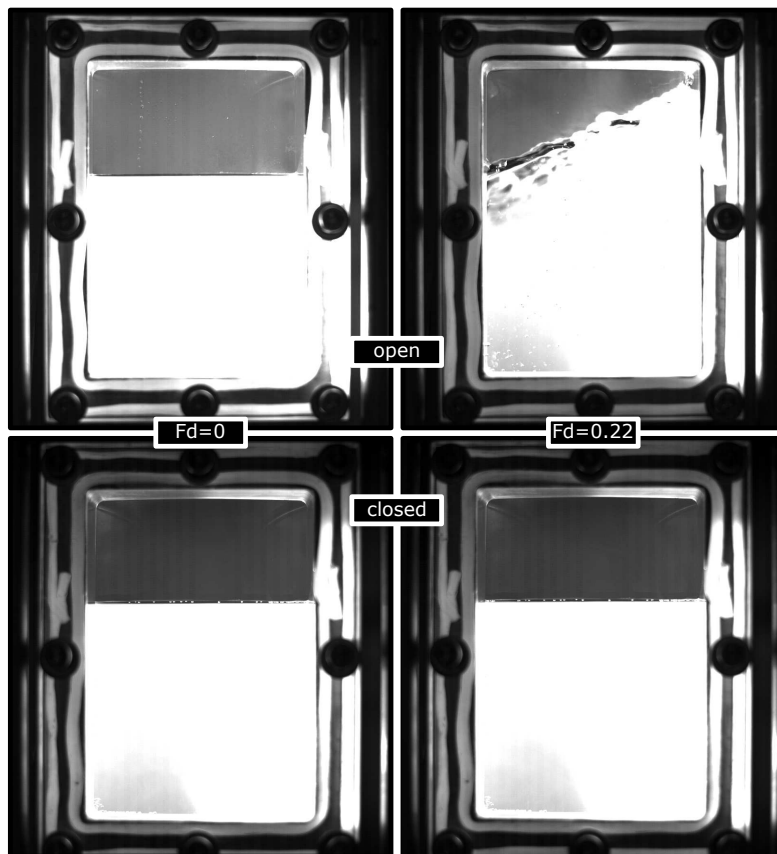
Figure 4.15: Qualitative comparison of surface motion at cone 2 (open vs. closed)

4.6 Influence of parameters

Observed behaviour of the free surface oscillation and characteristics depend on the changed parameters. The dependencies and identified influences of each parameter are recapitulated and summed up below.

4.6.1 Influence of runner rotation direction

- As observed in the conducted model test, the rotation direction of the free surface motion is equal to the runner rotation direction.

- The shape of the water surface is influenced by the rotation direction of the runner. If the runner rotates in pump rotation direction, the surface tends to be rougher. Additional the water shape is more ruptured and more water drops are unsnapped.

- In contrast to runner rotating in turbine rotation direction, the shift between flat state and free surface oscillation is clearly delimited for runner rotating in pump rotation direction. Only at high water level a transition area can be observed independent of the runner rotation direction.

- The frequency of the free surface oscillation depends on the runner rotation direction as well. It reaches higher values, if the runner rotates in pump rotation direction than in turbine rotation direction.

- Another influence of the rotation direction on f_{FSO} is identified: A steeper gradient of the regression line of detected frequencies is determined, if the runner rotates in pump rotation direction.

4.6.2 Influence of initial water level

- The initial water level is represented by κ, which is the z-coordinate normalized by the runner low pressure side diameter D_2.

- At high initial water level $E0.25$ the free surface oscillation is very chaotic. In contrast, a well developed free surface oscillation appears at other investigated initial water levels.

- The amplitude A of free surface oscillation is mainly influenced by the initial water level. A decrease of the amplitude is detected with increasing initial water level $E\kappa$. Basically, the amplitudes of the free surface oscillation are in a similar range for same initial water level.

- Determined frequencies show a linear behaviour. The theoretical intersection point of the regression line and the ordinate depends on the initial water level. The point of intersection for $E.50$ is higher than for initial water level $E1.00$.

4.6.3 Influence of densimetric Froude number Fd

- Different states of motion are observed in the executed experiments. They depend on the densimetric Froude number Fd. Starting with flat state, passing through transition states and finally reaching the periodic free surface oscillation. Increasing the densimetric Froude number continually, causes a ruptured surface and increases the break away of water droplet.

- The frequency of the free surface oscillation f_{FSO} depends on the densimteric Froude number. Increasing Fd results in an increase of the frequency f_{FSO} and a significant correlation is identified.

CHAPTER 5

Analytical modelling

This chapter shall be deemed to be an interpretation and continual discussion of the results obtained by conducted model tests.

First, general aspects and taken simplifications are described. A simple physical model is presented describing the angular velocity and frequency of the free surface oscillation at periodic state. Based on this an analytical approach is compiled and results in an equation characterising the observed motion. The aim of these considerations is to separate single processes and enable an interpretation of measurement results. Torque transmission and dependencies are treated to be used in an analytical model. The crossover between runner and fluids is estimated by means of torque equilibrium.

In the last section of this chapter experimental achieved data are compared to analytical approximation trying to represent qualitative behaviour and dependencies on different influencing factors.

5.1 Base flows

Under real conditions the runner rotates in air above a free water surface situated in the draft tube. Resulting there are two base flows:

- **Air flow:**
  The air flow between runner and free water surface is driven by the rotating runner. As a consequence the main flow is rotating around the runner rotation axis (respectively symmetry axis of draft tube cone) in sense of the runner rotation. Due to centrifugal forces secondary flow appears. It is directed radially outwards at the runner low pressure side level and radially inwards at the water surface level. In the rotation axis (center) the flow is directed axially upwards and downwards at the draft tube wall as simulated and confirmed in [45].

  Air is a compressible fluid with density $\rho = f(p, \vartheta)$ depending on pressure p and temperature ϑ. Due to very small Mach numbers ($Ma_{max} < 0.2$) the fluid is treated as incompressible. Essential numbers for characterisation of the air flow are:

  - **Reynolds number**
    According to general Reynolds number, defined by equation 2.3, the Reynolds number for the air flow Re_A is

    $$Re_A = \frac{\Omega_A D^2}{\nu_A} \tag{5.1}$$

    with Ω_A the angular velocity in air, diameter D and ν_A the kinematic viscosity of air.

  - **Ekman number**
    The Ekman number is described in 2.3 Dimensionless numbers in general notation (see equation 2.4). For air flow the Ekman number Ek_A is defined as

    $$Ek_A = \frac{\nu_A}{\Omega_A D^2} = \frac{1}{Re_A} \tag{5.2}$$

    and can be interpreted as the inverse of Reynolds number Re_A

- **Water flow:**
  The main water flow is in rotation. It is driven by the air flow due to shear stresses at the boundary layers of the fluids. Under specified experiment

conditions a free surface oscillation is excited as described in previous chapters. The excitation mechanism is not explicitly identified at this stage of investigation.

Dimensionless numbers, which characterise the main water flow are Reynolds number and Froude number as defined below.

– **Reynolds number**
The Reynolds number for the water flow Re_W is based on equation 2.3. It is defined as

$$Re_W = \frac{\Omega_W D^2}{\nu_W} \tag{5.3}$$

with the angular velocity of water Ω_W, the characteristic diameter D and the kinematic viscosity of water ν_W.

– **Froude number**
Basing on general definition (see equation 2.5) the Froude number of the water flow Fr_W is

$$Fr_W = \frac{\Omega_W D}{\sqrt{gh}} \tag{5.4}$$

where Ω_W is the angular velocity of the water, D the characteristic diameter, h the depth of water and g the gravity constant. The water depth h and the used value is discussed in section 5.6.

– **Ekman number**
According to general equation 2.4 the Ekman number Ek_W for the water flow is defined as

$$Ek_W = \frac{\nu_W}{\Omega_W D^2} = \frac{1}{Re_W} \tag{5.5}$$

and is the inverse of Re_W.

5.2 Simplifications

Following simplifications have been taken into account:

- **First simplification:** First of all, rigid body rotation is assumed and the whole system is reduced to three angular velocities in rad/s.

- Angular velocity of runner Ω_R
- Angular velocity of the air-volume Ω_A
- Angular velocity of the water-volume Ω_W

Hereinafter angular velocities of rigid body rotations are named by Ω and angular frequencies by ω. The simplifications are illustrated in Figure 5.1

- **Second simplification:** The draft tube of the model pump-turbine (and generally of all hydraulic machines) is rotationally axis symmetric around the runner rotational axis and conical for length h_1. At h_2 the flow is redirected by the draft tube elbow and ends into the tailwater. An illustration of the draft tube geometry is shown in Figure 3.3. For simplification reasons this kind of water reservoir is modelled as cylindrical tank with the runner low pressure side diameter D_2.

- **Third simplification:** The radial runner consists of seven runner blades. In the following approach it is reduced to a rotating disc. As a result the secondary flow at runner blade channels and the influence of runner blade number is neglected.
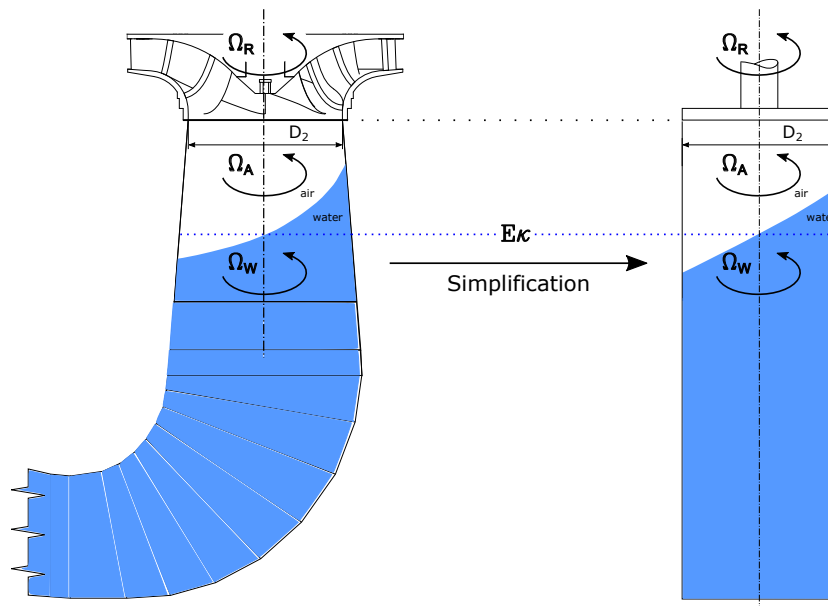

Figure 5.1: Appearing angular velocities and simplifications

5.3 Physical model

Real conditions are very complex and many impact factors are either not detectable or not considerable at the actual state of investigation. Due to this fact the reality is reduced to a practicable physical model which is described hereinafter.

The physical modelling is based on observations during the experiments. The observed states are described and discussed in previous sections 3.5 Measurement procedure and 4.1 General behaviour.

The crucial state for modelling is the unimposing flat state. In flat state no motion of free surface in z-axis appears, but even at very low densimetric Froude number Fd a rotational motion of water is visible. This leads to the basic concept of the water base flow rotating with angular velocity Ω_W defined as

$$\Omega_W = \frac{d\phi}{dt} \tag{5.6}$$

with angle ϕ as illustrated in Figure 3.7.

As we assume rigid body rotation, the free water surface and whole water base flow rotates in the flat state with velocity

$$u = \Omega_W \frac{D}{2} \tag{5.7}$$

where u is the circumferential velocity at $r = D/2$.

Hereinafter this motion is interpreted as the velocity of the rotating frame of reference. The oscillation of the free surface is composed of two parts: on the one hand the velocity of the rotating frame of reference and on the other hand the excited motion of the free surface.

According to equation 5.8 absolute velocity c consists of the circumferential velocity of the rotating frame of reference u and the relative velocity of excited water mass w.

$$c = u + w \tag{5.8}$$

c is the absolute velocity from the point of view of a stationary observer. At flat state the relative velocity $w = 0$ and consequently $c = u$. At the periodic state of free surface oscillation $w \neq 0$ and c is the velocity of free water surface.

This modelling is supposed to reproduce the physical dependencies, separate the main processes and qualitatively describe the behaviours observed in the experiments. An analytical approach aiming on these goals and trying to calculate the absolute velocity c is presented in the next sections 5.4 and 5.5.

5.4 Analytical approach

Key issues for characterisation of the velocity of free surface oscillation as defined in equation 5.8 are the rotating frame of reference and the approach describing the relative motion of excited water mass.

The wave motion at free fluid surface is described in [3]. Considerations are restricted to plane waves under conditions of potential flow as defined in [43]. Fluid density is assumed as constant and at $z = -h$ a wall is expected as boundary condition as one can see in Figure 5.2.
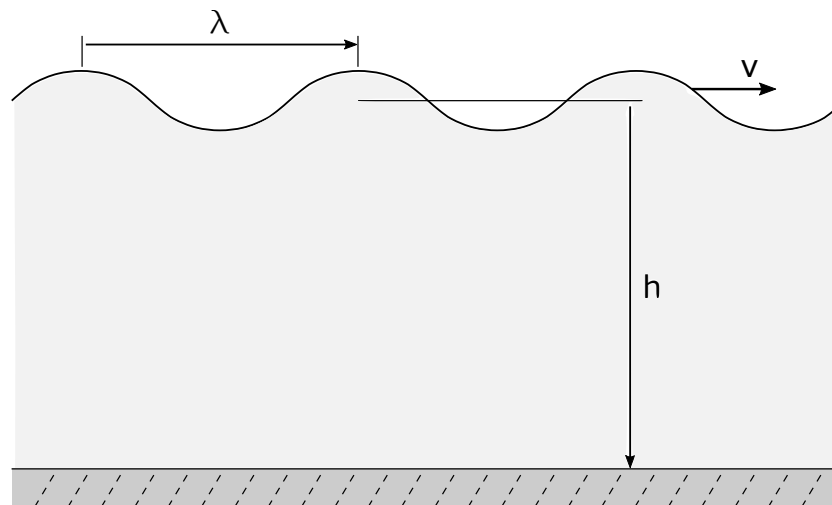
Figure 5.2: Plane wave motion following [3]

According to [3] the velocity of wave propagation v is

$$v = \sqrt{\frac{\lambda g}{2\pi} \tanh\left(\frac{2\pi h}{\lambda}\right)} \tag{5.9}$$

with wavelength λ, gravitational constant g and water depth h. Time for passing through one wavelength is

$$T = \frac{\lambda}{v} \tag{5.10}$$

Basing on this equations the relative motion w is described.

As already mentioned equation 5.9 applies to plane waves, but actual investigated flow appears in a rotationally symmetric tank. Therefore it has to be unwounded on the shell surface. Due to periodicity reasons the wave number has to be integer. Above critical densimetric Froude number Fd_{crit} azimuthal wave number is $m = 1$ which is known from experiments and confirmed by literature [57], [47] and [10].

Small humps or wave crest breaking are neglected.
As only one wave appears the wavelength is equal to circumference:

$$\lambda = D\pi \tag{5.11}$$

Using this limiting condition for equation 5.9 the relative velocity of free water surface can be described as

$$w = \sqrt{\frac{Dg}{2} \tanh\left(\frac{2h}{D}\right)} \tag{5.12}$$

with diameter D at initial water level $E\kappa$, gravitational constant g and water depth h. The relative wave motion is a periodic process. Due to this fact a frequency can be defined as

$$f = \frac{\omega}{2\pi} \tag{5.13}$$

where ω is the angular frequency of the relative wave motion.
Passing through time T can be interpreted as periodic time coupled with the frequency of a periodic motion by

$$f = \frac{1}{T} \tag{5.14}$$

Combining equation 5.13 and 5.14 with equation 5.10 leads to

$$v = \lambda \frac{\omega}{2\pi} \tag{5.15}$$

in general notation. Using equation 5.11 of the wavelength λ for previously described special case with azimuthal wave number $m = 1$ the relative velocity can be described in special form

$$w = \frac{D}{2}\omega \tag{5.16}$$

Now the angular frequency of relative wave motion can be calculated by modified equation 5.12 as

$$\omega = \sqrt{\frac{2g}{D} \tanh\left(\frac{2h}{D}\right)} \tag{5.17}$$

where D is the tank diameter at initial water level $E\kappa$, g the gravitational constant and h the depth of water volume.

Thinking back to physical modelling and basically approach the absolute velocity of free surface oscillation c_{FSO} at diameter D is the sum of the velocity of rotating frame of reference and the relative velocity of wave motion (see equation 5.8). Absolute velocity of free surface oscillation c_{FSO} can be calculated by

$$c_{FSO} = \Omega_W \frac{D}{2} + \sqrt{\frac{Dg}{2} \tanh\left(\frac{2h}{D}\right)} \tag{5.18}$$

with special form of relative velocity of wave motion w defined in equation 5.12 and circumferential velocity u according to equation 5.7. Following the same line of argumentation as previously for relative velocity, the relation between absolute velocity and frequency of free surface oscillation is

$$c_{FSO} = D\pi f_{FSO} \tag{5.19}$$

Hence the angular frequency of free surface oscillation ω_{FSO} for wavelength as defined in equation 5.11 is

$$\omega_{FSO} = \Omega_W + \omega \tag{5.20}$$

with angular velocity of rotating frame of reference, respectively base flow, Ω_W and angular frequency of relative wave motion according to equation 5.17. Thus ω_{FSO} depends on the one hand on rotation of base flow Ω_W and on ω on the other hand. Considering equation 5.17 of angular velocity ω, the value of angular frequency depends only on geometric parameters. Therefore it is a constant offset only changing for different initial water levels $E\kappa$.

The influence of wave motion is even more clarified, if equation 5.20 is normalized by ω.

$$\frac{\omega_{FSO}}{\omega} = \frac{\Omega_W}{\omega} + 1 \tag{5.21}$$

Thus the ratio of angular frequencies ω_{FSO}/ω is expressed by a linear equation where Ω_W/ω can be interpreted as gradient of the curve with ordinate intersection point depending on ω. Symbolic linear characteristic following equation 5.21 is illustrated in Figure 5.3.

Figure 4.7 and 4.8 show the results of measurements (see section 4.3). Comparing with Figure 5.3 the similarity in curve characteristic can clearly be seen. Therefore the analytical approach is a satisfying qualitative description of characteristic and free surface oscillation is separated in main components regarding angular frequency ω_{FSO} and velocity c_{FSO}.
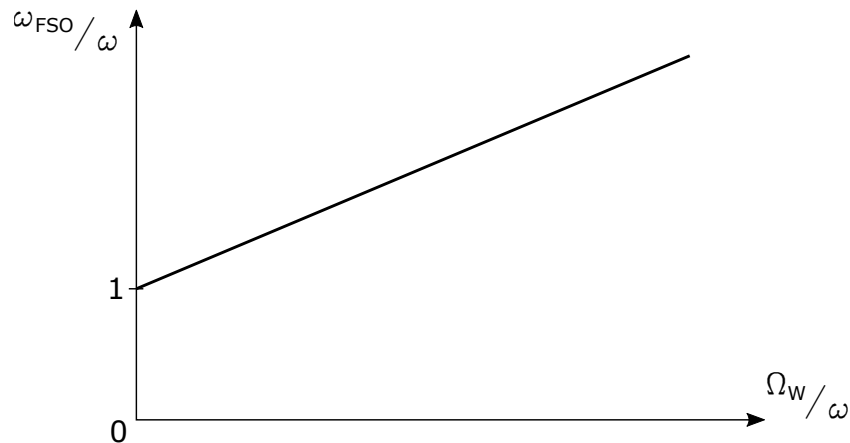
Figure 5.3: Symbolic characteristic of angular frequency ratio ω_{FSO}/ω

Recapitulating the dependencies of first main component ω are discussed and analysed in this section. Second main component Ω_W, obviously responsible for the increase of angular frequency of free surface oscillation, is treated in following section 5.5.

5.5 Torque transmission

This section deals with the analytical approach of the driving mechanism of the base flow rotating with Ω_W. The water flow is driven by the air flow due to shear stresses. Therefore the torque transmission from runner to air and next air to water flow is considered. Dependencies and main influence parameters shall be identified. Finally an estimation for Ω_W should be achieved. It is used in equation 5.21 and respectively in equation 5.20.

The conceptual starting point is the approach for a rotating disc in resting fluid (angular velocity of fluid $\Omega_f = 0$) [9]. Accordingly the friction force acting on a infinite small part ring of the disc is calculated by

$$dF = c_F \rho_f \frac{U^2}{2} dO \tag{5.22}$$

with friction coefficient c_F, density of the fluid ρ_f, circumferential velocity of the disc U at radius r and related surface dO. The surface of a small part ring is defined as

$$dO = 2r\pi dr \tag{5.23}$$

In the actual approach the fluid is not in rest ($\Omega_f \neq 0$). Instead it rotates with an angular velocity Ω_f and is driven by the disc. In actual case it is driven by

the runner, rotating with Ω_R. For the sake of completeness it is remarked that $\Omega_R > \Omega_f$. Thus the circumferential velocity at radius r is

$$U = (\Omega_R - \Omega_f)r \tag{5.24}$$

which is decisive for friction. Taking these two equations (5.23 and 5.24) into account in equation 5.22 the force due to friction for this approach results in following equation

$$dF = c_F \rho_f r^3 \pi (\Omega_R - \Omega_f)^2 dr \tag{5.25}$$

where c_F is the friction coefficient, ρ_f the fluid density, Ω_R the angular velocity of runner and Ω_f of fluid. r is the radius and dr the infinite small width of ring part as illustrated in Figure 5.4.
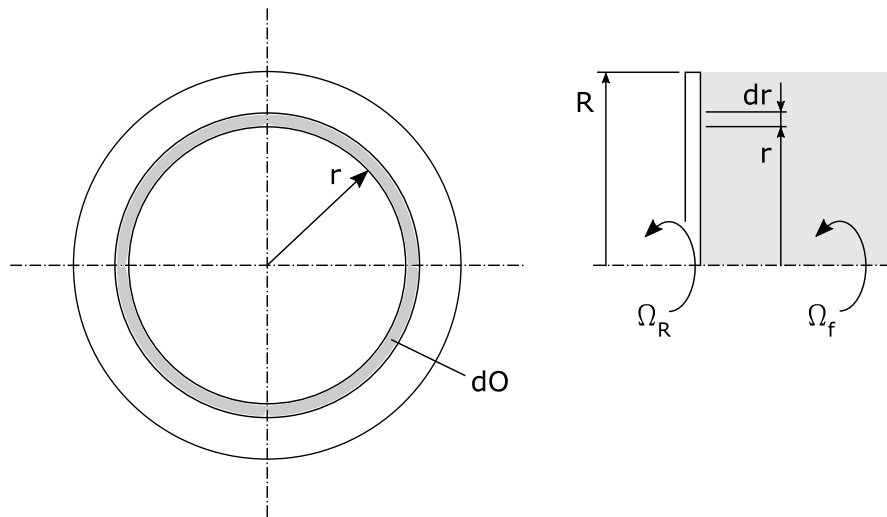
Figure 5.4: Rotating disc (Ω_R) with rotating fluid (Ω_f) at one side and infinite small part dO at radius r

The torque between one side of the disc or rather runner and fluid is calculated as following:

$$T = \int_0^R r \cdot dF \tag{5.26}$$

Restricting $c_F \neq f(r)$, or in other words c_F as constant for all radii r, the torque is consequently

$$T = c_F \rho_f \pi (\Omega_R - \Omega_f)^2 \frac{R^5}{5} \tag{5.27}$$

Exchanging friction number c_F by torque coefficient c_M which is defined in [9]

$$c_M = \frac{4\pi}{5}c_F \tag{5.28}$$

leads to finally used equation for transmitted torque

$$T = \frac{c_M}{4}\rho_f(\Omega_R - \Omega_f)^2 R^5 \tag{5.29}$$

As already mentioned rigid body rotation is assumed. Hence the analytical model consists of three rigid bodies:

- by motor generator driven **runner**

- **air** driven by rotating runner

- and due to shear stresses by air flow driven **water** volume

Additional the Ekman numbers Ek as defined in equations 5.2 and 5.5 are very small ($Ek_A < 7.6 \cdot 10^{-6}$, $Ek_W < 3.8 \cdot 10^{-4}$). Hence, a distinctly and well developed flow core is assumed for each flow. The resulting schematic profile of the angular velocity is outlined in Figure 5.5.

Because of simple illustration and for qualitative description the special profile for $c_M = const.$ is depicted. As a result the velocity gradients are the same at all crossover passages. For different torque coefficients c_M, the gradients in each boundary layers are different. The analytical model is simplified by defining flat and solid wall at $y = 0$ as boundary condition.

The transmitted torque T_{12} due to shear stress for rigid body 1 to rigid body 2 expressed by friction number c_F and c_M is

$$T_{12} = \frac{c_F\rho\pi}{5}(\Omega_1 - \Omega_2)^2 R^5 \tag{5.30}$$

$$T_{12} = \frac{c_M\rho}{4}(\Omega_1 - \Omega_2)^2 R^5 \tag{5.31}$$

with angular velocity of rigid body 1 Ω_1 and of rigid body 2 Ω_2; where $\Omega_1 > \Omega_2$. For simplified model with cylindrical tank and outer radius $R = D_2/2$ the transmitted torque by previously listed and in Figure 5.5 depicted components is consequently:

$$T_{RA} = \frac{c_{RA}\rho_A}{4}(\Omega_R - \Omega_A)^2 \left(\frac{D_2}{2}\right)^5 \tag{5.32}$$
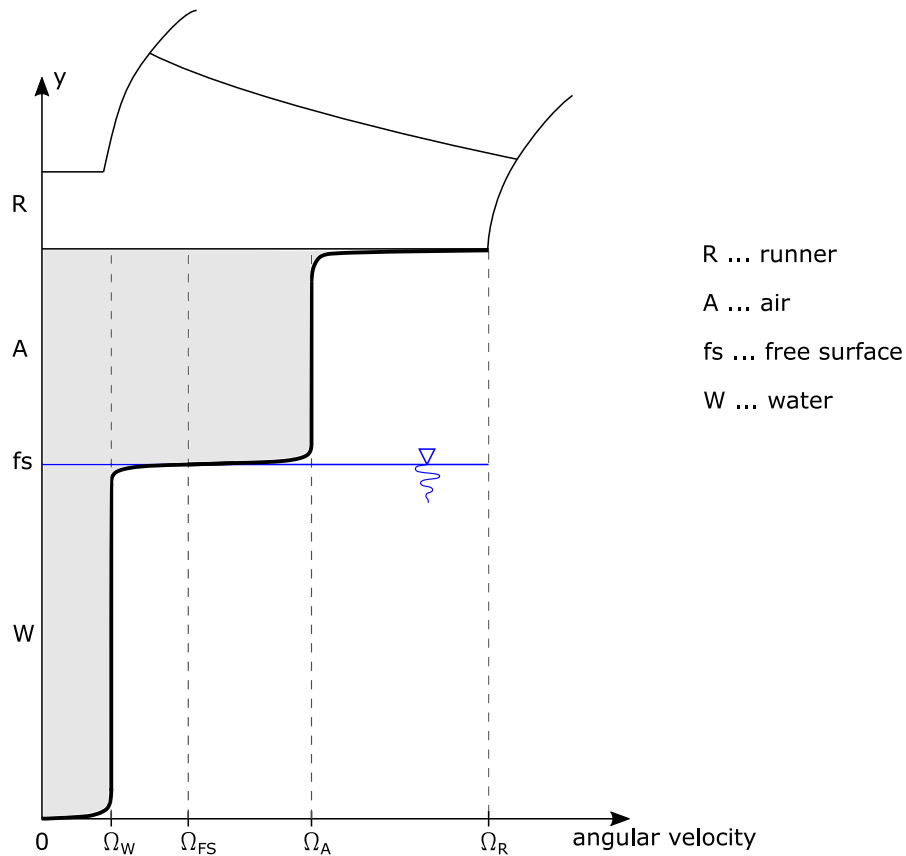
Figure 5.5: Schematic illustration of rigid body rotation and angular velocity profile

$$T_{Afs} = \frac{c_{Afs}\rho_A}{4}(\Omega_A - \Omega_{fs})^2 \left(\frac{D_2}{2}\right)^5 \tag{5.33}$$

$$T_{fsW} = \frac{c_{fsW}\rho_W}{4}(\Omega_{fs} - \Omega_W)^2 \left(\frac{D_2}{2}\right)^5 \tag{5.34}$$

$$T_W = \frac{c_W\rho_W}{4}\Omega_W^2 \left(\frac{D_2}{2}\right)^5 \tag{5.35}$$

with air density ρ_A, water density ρ_W and runner low pressure side diameter D_2.

The transmitted torques are named after the interacting components; R stands for runner, A for air, fs for free surface and W for water. Consequently T_{RA} is the transmitted torque from the runner to the air volume and c_{RA} the related torque coefficient. T_W is the torque between rotating water volume and resting bottom. Due to boundary condition of solid wall and $\Omega = 0$ at $y = 0$ equation 5.35 has only one angular velocity without a velocity difference.

Neglecting the friction at the tank walls, the equilibrium of torque results from equating input and output torque of each component:

$$c_{RA}\rho_A(\Omega_R - \Omega_A)^2 = c_{Afs}\rho_A(\Omega_A - \Omega_{fs})^2 \tag{5.36}$$

$$c_{Afs}\rho_A(\Omega_A - \Omega_{fs})^2 = c_{fsW}\rho_W(\Omega_{fs} - \Omega_W)^2 \tag{5.37}$$

$$c_{fsW}\rho_W(\Omega_{fs} - \Omega_W)^2 = c_W\rho_W\Omega_W^2 \tag{5.38}$$

Equation 5.36 belongs to the air volume, equation 5.37 to the free surface and equation 5.38 to the water volume.

These three equations build an equation system. The solution results in following ratios of angular velocities:

$$\frac{\Omega_R}{\Omega_A} = 1 + \sqrt{\frac{c_W\rho_W}{c_{RA}\rho_A}}\left(1 + \sqrt{\frac{c_W}{c_{fsW}}} + \sqrt{\frac{c_W\rho_W}{c_{Afs}\rho_A}}\right)^{-1} \tag{5.39}$$

$$\frac{\Omega_A}{\Omega_W} = 1 + \sqrt{\frac{c_W}{c_{fsW}}} + \sqrt{\frac{c_W\rho_W}{c_{Afs}\rho_A}} \tag{5.40}$$

$$\frac{\Omega_R}{\Omega_W} = 1 + \sqrt{\frac{c_W}{c_{fsW}}} + \sqrt{\frac{c_W\rho_W}{c_{Afs}\rho_A}} + \sqrt{\frac{c_W\rho_W}{c_{RA}\rho_A}} \tag{5.41}$$

Angular velocity ratios of runner Ω_R, air Ω_A and water Ω_W depend on density ratio ρ_W/ρ_A and on torque coefficients. Because of simplifications the geometry parameters do not affect the angular velocity ratio.

To make equations more readable the constant factor k is introduced as

$$k = 1 + \sqrt{\frac{c_W}{c_{fsW}}} + \sqrt{\frac{c_W \rho_W}{c_{Afs} \rho_A}} \tag{5.42}$$

and by means of k equations 5.39, 5.40 and 5.41 can be expressed by

$$\frac{\Omega_R}{\Omega_A} = 1 + k^{-1} \sqrt{\frac{c_W \rho_W}{c_{RA} \rho_A}} \tag{5.43}$$

$$\frac{\Omega_A}{\Omega_W} = k \tag{5.44}$$

$$\frac{\Omega_R}{\Omega_W} = k + \sqrt{\frac{c_W \rho_W}{c_{RA} \rho_A}} \tag{5.45}$$

These equations of angular velocity ratios, basing on the approach of torque transmission, are used for the determination of the angular frequency of free surface oscillation ω_{FSO}; which is calculated according to equations 5.20 or 5.21.
An estimation of main parameters and interpretation of presented equations is done in section 5.6 Comparison to experimental results afterwards.

5.6 Comparison to experimental results

Basing on linear equation 5.21 the analytical approach and experimental results presented in section 4.3 Frequency of the free surface oscillation shall be compared. Crucial mechanism for measured behaviour will be determined and experimental results and observed behaviour interpreted.

Linear equation 5.21 describes the characteristic of angular frequency ω_{FSO} depending on angular velocity Ω_W - both normalized by angular frequency ω. At the end of section 5.4, ω is identified as depending on geometrical parameters; only changing for different initial water levels $E\kappa$. Hence, this variable of equation can be calculated, but angular velocity of water base flow Ω_W is unknown. The angular velocity of runner Ω_R is well known, because it is a measured parameter. Therefore equation 5.21 is extended by Ω_R leading to

$$\frac{\omega_{FSO}}{\omega} = \frac{\Omega_R}{\omega} \frac{\Omega_W}{\Omega_R} + 1 \tag{5.46}$$

which is more usable. The relation of Ω_W and Ω_R is the reciprocal of equation 5.45 derived in section 5.5 Torque transmission. Using equation 5.17 of angular frequency ω and equation 5.45 to 5.46 results in

$$\frac{\omega_{FSO}}{\omega} = \frac{\Omega_R \sqrt{D}}{\sqrt{2g}\sqrt{\tanh\left(\frac{2h}{D}\right)}}\frac{1}{k} + 1 \tag{5.47}$$

with tank diameter D at initial water level, gravity constant g, water depth h and density ratio of water and air flow. Factor k is defined in equation 5.42 and depends on the torque coefficients and the density ratio. Using this equation, an estimation of ω_{FSO} is already possible.

To be more comparable to experimental results presented in Figure 4.8 and to clarify dependencies some additional conversions are done. Therefore Ω_R can be expressed by

$$\Omega_R = \frac{2u_2}{D_2} \tag{5.48}$$

where u_2 is the circumferential velocity of runner low pressure side at diameter D_2. Extending equation 5.47 by $\sqrt{D_2}$ and using equation 5.48 of runner angular velocity Ω_R leads to

$$\frac{\omega_{FSO}}{\omega} = \sqrt{\frac{2D}{D_2}}\frac{u_2}{\sqrt{gD_2}}\frac{1}{k\sqrt{\tanh\left(\frac{2h}{D}\right)}} + 1 \tag{5.49}$$

Constant factor k is defined by equation 5.42. Using this definition and extending equation 5.49 with density ratio ρ_A/ρ_W the following equation is achieved:

$$\frac{\omega_{FSO}}{\omega} = \frac{\sqrt{\frac{2D}{D_2}}\sqrt{\frac{\rho_A}{\rho_W}}\frac{u_2}{\sqrt{gD_2}}}{\left[\sqrt{\frac{\rho_A}{\rho_W}}\left(1+\sqrt{\frac{c_W}{c_{fsW}}}\right)+\sqrt{\frac{c_W}{c_{Afs}}}+\sqrt{\frac{c_W}{c_{RA}}}\right]\sqrt{\tanh\left(\frac{2h}{D}\right)}} + 1 \tag{5.50}$$

with the diameter of tank D at initial water level $E\kappa$, diameter of runner low pressure side D_2, h the depth of water volume and torque coefficients c_W, c_{fsW}, c_{Afs}, c_{RA} named after interacting components as described in section 5.5 and Figure 5.5.

Due to the reason of clarity, factor K is introduced as

$$K = \frac{1}{\sqrt{\frac{\rho_A}{\rho_W}}\left(1+\sqrt{\frac{c_W}{c_{fsW}}}\right)+\sqrt{\frac{c_W}{c_{Afs}}}+\sqrt{\frac{c_W}{c_{RA}}}} \tag{5.51}$$

and the definition of densimetric Froude number Fd according equation 2.12 is

73

used. Finally the angular frequency of free surface oscillation ω_{FSO} normalized by ω can be calculated and expressed with

$$\frac{\omega_{FSO}}{\omega} = K\sqrt{\frac{2D}{D_2}}\frac{1}{\sqrt{\tanh\left(\frac{2h}{D}\right)}}Fd + 1 \qquad (5.52)$$

This equation describes a curve characteristic comparable with the results of measurements presented in Figure 4.8 (section 4.3 Frequency of the free surface oscillation).

Equation 5.52 resulting from analytical approach and curve characteristics determined by experiments show linear behaviour. Due to analytical considerations the intersection points depicted in Figure 4.8 are interpreted as angular frequency. Converting the detected frequencies f_{FSO} into angular frequencies ω_{FSO} (using equation 5.13) and normalizing the measurement results by belonging intersection points (summed up in Table 5.2) results in diagram as shown in Figure 5.6. The angular frequency of free surface oscillation ω_{FSO} normalized by ω is used as ordinate and corresponding densimetric Froude number as abscissa.
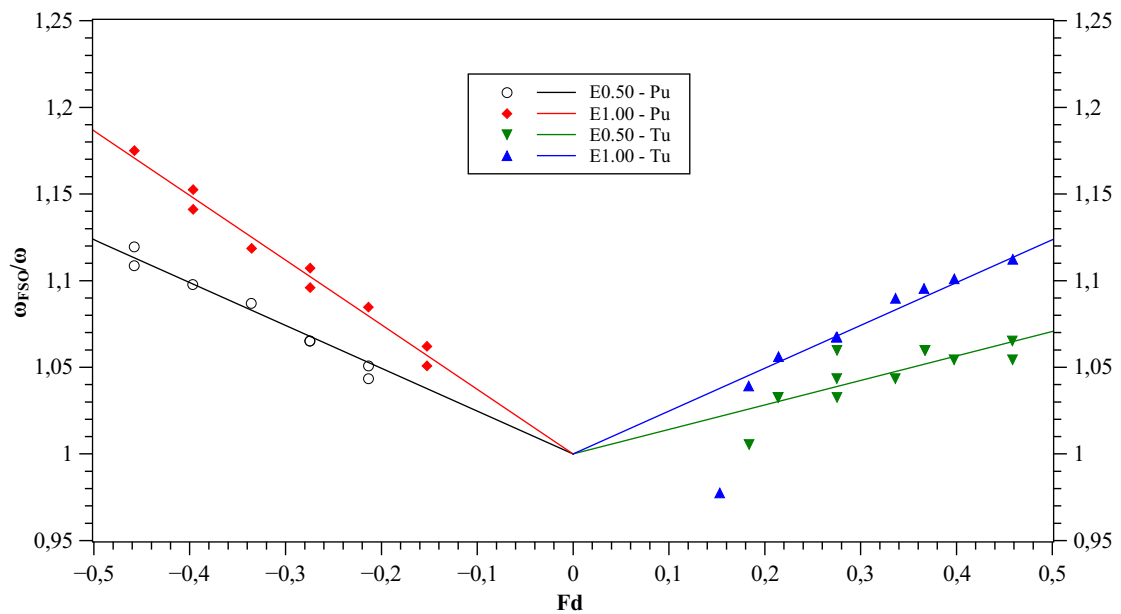
Figure 5.6: Normalized characteristic of ω_{FSO} determined by experiments

Term $K\sqrt{\frac{2D}{D_2}}\frac{1}{\sqrt{\tanh(2hD^{-1})}}$ is clarified to be responsible for the increase of angular frequency ω_{FSO}, respectively frequency f_{FSO} of free surface oscillation, by comparing Figure 5.6 and equation 5.52. Resulting from conducted experiments, the gradient of frequency characteristic is higher for runner rotating in pump rotation

direction than in turbine rotation direction. Moreover the gradient increases with increasing κ, which is the normalized distance between runner and initial water level.

Both effects are qualitatively represented by the analytical approach. Firstly the torque coefficient with runner rotating in pump direction is higher than in turbine rotation direction. Consequently the amount of factor K is higher. Secondly increasing κ, meaning lowering initial water level in conical draft tube, results in increasing diameter D. Therefore the value of the described term, representing the gradient of characteristics, increases.

Regarding hyperbolic tangent term it is worthy of discussion how water depth h is defined. Dimensions and geometry of investigated draft tube are illustrated in Figure 3.3 and described in section 3.2. The draft tube is conical till $h_1 = 1.49D_2$ - which is minimal reference level, but the water column is much deeper. The other possibilities are: considering total height h_2 of draft tube or even total streamline till tail water. Considering total height of draft tube h_2 causes water depth $h_{E0.50} = 2.66D_2$ and $h_{E1.00} = 2.16D_2$ for initial water level $E0.50$ and $E1.00$. Applying these values the hyperbolic tangent is

$$\tanh\left(\frac{5.32D_2}{D_{E0.50}}\right) = 0.9999 \tag{5.53}$$

$$\tanh\left(\frac{4.32D_2}{D_{E1.00}}\right) = 0.9994 \tag{5.54}$$

where $D_{E0.50}$ and $D_{E1.00}$ are diameter of the draft tube cone at level $E0.50$ and $E1.00$. Hence the hyperbolic tangent term does not essentially affect the results, because of the investigated draft tube geometry.

The torque coefficients need to be estimated to get an order of magnitude of the gradients calculated by the analytical approach by means of equation 5.52. [9] deals with torque coefficients for free rotating disc, [13] deals with enclosed rotating discs and [39] deals with torque coefficients for free and enclosed rotating disc. According c_M depends on Reynolds number Re defined as

$$Re = \frac{R^2\Omega}{\nu} \tag{5.55}$$

with radius R and angular velocity Ω of the driving component. ν is the kinematic viscosity of driven fluid.
Due to reciprocal dependencies the calculation of torque coefficients is an iterative process:

- First torque coefficients have to be assumed. Chosen value for all coefficients

is $c_M = 0.0015$.

- Next the angular velocities are calculated using equations 5.43, 5.44 and 5.45 resulting from the torque transmission approach. The angular velocity of runner Ω_R is a measured value known from the experiments.

- Afterwards Re for each crossover passage is determined with data for kinematic viscosity listed in [60].

- The resulting values indicate laminar boundary layers according criterion [38], [9]

$$Re < Re_{crit} = 2...3 \cdot 10^5 \tag{5.56}$$

Hence the torque coefficient for enclosed rotating disc is defined in [39] as

$$c_M = \frac{1}{Re}\frac{D}{2s} \tag{5.57}$$

for gap s smaller than boundary layer and if gap s is a multiple of boundary layer c_M is calculated by

$$c_M = \frac{0.64}{\sqrt{Re}}\left(1 - 0.31e^{-12s/R}\right) \tag{5.58}$$

The torque coefficients c_{RA} and c_{fsW} are calculated by equation 5.58. An estimation of coefficients c_{Afs} and c_W is done by means of equation 5.57. Due to the very thin free surface and very thin wall regime gap, no secondary flow is expected.

- After calculating the values for the torque coefficients c_{RA}, c_{Afs}, c_{fsW} and c_W next iteration step starts.

- After a view iterations ($n = 6$) the values of the torque coefficients do not change in 4th decimal place - which is decided to be sufficient.

Final results of torque coefficients for all crossover sections are listed in Table 5.1. Three different cases are considered. At *rotating disc case* the runner is assumed as smooth rotating disc and c_{RA} results from previously described equation. For *pump case* the fluid interaction is inadequate described by a smooth disc, because of flow interaction between runner blades and air. Taking this into account the torque coefficient c_{RA} for pump case is increased by one order of magnitude. In *turbine case* the runner blades and the air flow interact in a smaller extent. Hence the values of torque coefficient c_{RA} are assumed roughly same as in rotating disc case.

Using the achieved values for torque coefficients (Table 5.1) it is possible to calculate factor K. Therefore equation 5.51 is applied. Of course the results depend on

Table 5.1: Applied torque coefficients and resulting factor K

	Rotating disc		Pump		Turbine	
	E0.50	E1.00	E0.50	E1.00	E0.50	E1.00
c_{RA}	0.00177	0.00177	0.02000	0.02000	0.00200	0.00200
c_{Afs}	0.05431	0.05069	0.05431	0.05069	0.05431	0.05069
c_{fsW}	0.00256	0.00239	0.00256	0.00239	0.00256	0.00239
c_W	0.21476	0.21476	0.21476	0.21476	0.21476	0.21476
K	0.07491	0.07446	0.17807	0.17554	0.07873	0.07823

the assumed case and on initial water level. Gap s interpreted as height of fluid volume correlates to $E\kappa$ and Reynolds number depends on diameter D.

After determining all previously unknown terms it is possible to apply the values in normalized characteristic equation 5.52. The gradients of trend line are listed in Table 5.2 determined by experiments and by analytical approach. The order of magnitude fits well and general trends are represented by the approach. Trend lines and gradients are delineated in Figure 5.7. It shows the results for runner rotating in turbine rotation direction in first quadrant and pump rotation direction in second. Illustrated points are measurement data and corresponding trend lines are dotted. The other trend lines are calculated by means of analytical approach.
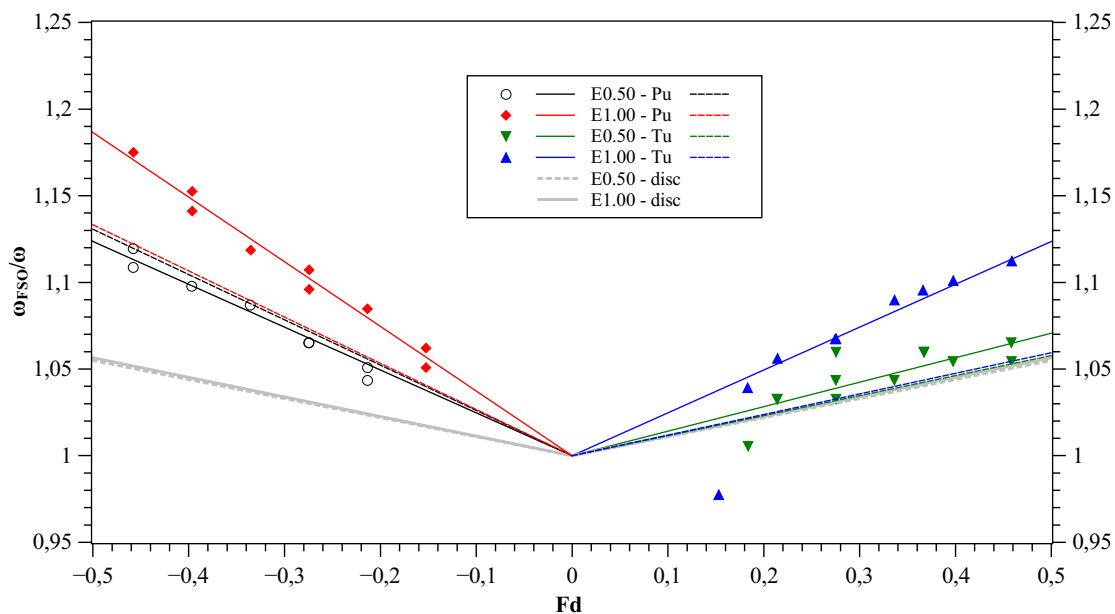

Figure 5.7: Normalized characteristic of ω_{FSO} determined by experiments and gradients estimated by analytical approach

Table 5.2: Comparison of experimental and analytical determined values

	Experiments		Analytical approach			
	Pump	Turbine				
	intersection point		ω	f	ω_{nat}	f_{nat}
	(Hz)	(Hz)	(rad/s)	(Hz)	(rad/s)	(Hz)
E0.50	1.84	1.84	8.118	1.292	11.016	1.753
E1.00	1.77	1.78	7.839	1.248	10.642	1.694
	gradient ω_{FSO}/ω vs. Fd		gradient ω_{FSO}/ω vs. Fd			
	Pump	Turbine	Disc	Pump	Turbine	
E0.50	0.239	0.141	0.1099	0.2613	0.1155	
E1.00	0.373	0.247	0.1130	0.2665	0.1188	

The dependency of torque coefficient c_{RA} is clearly shown, as trend lines of rotating smooth disc have smallest gradient and trend line of pump highest gradient. The influence of initial water level is represented as well, but not in the same extension as detected in the experiments.

So far, discussion of experimental results is done using results normalized by angular frequency ω. Subsequently an estimation for ω and discussion of absolute values is done. ω is calculated by equation 5.17, which is described in detail in section 5.4. According previously discussed topic the water depth h is defined from initial water level to the bottom of the draft tube with total height h_2. Consequently hyperbolic tangent has no influence on the result, as pointed out in equations 5.53 and 5.54. For each initial water level diameter D changes and same as in experiments ω decreases by lowering initial water level $E\kappa$. The calculated values are shown in Table 5.2 and illustrated in Figure 5.8.

As discussed, ω depends only on geometrical parameters. Thus it is predefined by the design of the components.
[26] deals with modal analysis of fluids in rigid containers. Among other topics an equation of natural frequencies of free surface in upright cylindrical tanks is presented. Of course it depends on the dimensions of the components too. Although approach is different, it finally leads to

$$\omega_{mn}^2 = \frac{\zeta_{mn}g}{R} \tanh\left(\frac{\zeta_{mn}h}{R}\right) \tag{5.59}$$

where R is radius of cylindrical tank, h depth of water and ζ_{mn} the roots of dJ_m/dr. J_m is the *Bessel function* and in actual case $\zeta = 1.841$. More documentation, values and graphs are provided in [6] and [1].

Replacing R by half diameter D of the initial water level, substitute value of ζ and square root extraction results in

$$\omega_{nat} = \sqrt{1.841\frac{2g}{D}\tanh\left(1.841\frac{2h}{D}\right)} \tag{5.60}$$

Mentioning equation 5.17, which is defining ω, one can notice that terms are similar except constant factor $\zeta = 1.841$. Calculated values for natural angular frequency according equation 5.60 [26] are also listed in Table 5.2. Moreover, they are depicted in Figure 5.8 converted by equation 5.13.
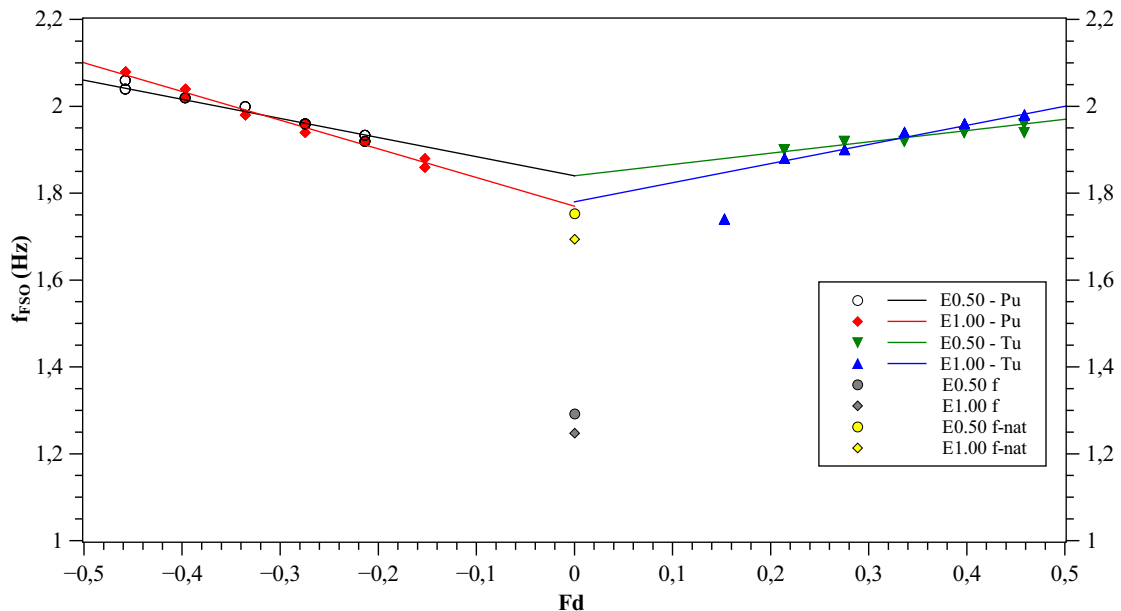

Figure 5.8: Measurement results and estimated intersection points by means of equation 5.17 and 5.60

As apparent in Figure 5.8 the intersection point for initial water level $E = 0.50$ is higher than $E1.00$. Equations 5.17 and 5.60 achieve the same behaviour. The differences between the values for initial water levels are in the same range. Even if the values are in similar order of magnitude, both equations underestimate the intersection point frequency. Equation 5.17 basing on [3] is derived from the equations applied to plane waves and described in section 5.4. As a result the absolute values show deviations to the measured values. Equation 5.60 [26] provides a better approximation. The differences are justifiable by the conical draft tube.

Summing up, the trend represented by the analytical approach and obtained by the experimental results is the same. Decreasing the initial water level $E\kappa$ results in an increases gradient of trend line and intersection point, respectively angular frequency ω, decreases. The angular frequency of free surface oscillation ω_{FSO} depends on the draft tube geometry, on densimetric Froude number Fd and on the torque coefficients. Last two parameters influence the rotation of the frame of reference Ω_W. The gradient of frequency rises, but seems not to affect the relative motion of water volume, which only depends on geometry.

One restriction has to be taken into account: the considerations and the approach are only valid for azimuthal wave number $m = 1$. Therefore densimetric Froude number is higher than the critical densimetric Froude number Fd_{crit} achieved by experiments. The intersection point is used for description of characteristic and only theoretical as no motion occurs at $Fd = 0$.

An interesting fact is, that almost similar equations are achieved for estimation of angular frequency ω by two different basic ideas. The analytical approach is not claimed to approximate real conditions and behaviour best. Main goal is the interpretation and discussion of experimental results as well as the identification of main processes, impact factors and dependencies onto the frequency of free surface oscillation. Therefore the approach is suitable and a basis for further investigations.

CHAPTER 6

Conclusions

Present thesis deals with the experimental investigation of the free surface oscillation at the draft tube cone of hydraulic machines.

Investigated model pump-turbine has a speed factor $N_{QE} = 0.126$ ($n_q = 41.8 rpm$) in turbine mode and $N_{QE} = 0.125$ ($n_q = 41.6 rpm$) in pump mode. It is equipped with a draft tube cone made of acrylic glass for optical investigations. In addition to the standard instrumentation the machine is equipped with fast response pressure transducers at different planes and positions.

The experiments are conducted for both runner rotation directions, for different densimetric Froude numbers Fd and for three initial water levels at the draft tube with a distance of 0.25, 0.75 and $1.00 D_2$ to runner low pressure side. The densimetric Froude number is a dimensionless number providing a similarity condition to prototype.

The amplitude of the free surface oscillation is determined by post-processing of high speed camera recordings. As a result the characteristics and a critical densimetric Froude number are determined. The amplitude mainly depends on the initial water level and the densimetric Froude number Fd.

For characterisation of the free surface oscillation the frequency f_{FSO} is detected by means of pressure signals. The detected frequencies are confirmed as frequency of the free surface oscillation by an additional optical method using the captured high speed camera recordings. A general trend and dependencies are identified by using acquired data.

Furthermore, the signal characteristic of the free surface oscillation is discussed and general behaviour as well as the circumferential propagation are described. In addition, the measurements are repeated with a second draft tube cone, which is made of steel. This is done for comparison reasons and to investigate the influence of wall vibrations on the excitation of the free surface oscillation.

Finally an analytical model is presented based on some simplifications. It aims at the separation of the single processes and representing the qualitative behaviour and dependencies. The model is used to identify and describe the main components of the free surface oscillation. It results in an equation, which qualitatively describes the frequency characteristic and behaviour observed at the model test. The main influencing parameters on the angular velocity and the frequency of the free surface oscillation are identified and discussed.

CHAPTER 7

Future challenges and work

The synchronous condenser mode and dewatered operation in general hold a lot of scientific challenges. Focusing on the free surface oscillation there are additional scientific challenges and supplementary issues.

The first and maybe most interesting task is the identification of the excitation mechanism. Present thesis provides a basis for this investigation. As the analytical model bases on the theory of air flow exciting the free surface motion, which is comparable with the excitation of plane ocean waves. The comparison measurements and investigations carried out with draft tube cone 2 mounted, reinforce this theory. In that context non-invasive flow measurements of the air flow as well as the water flow for $Fd < Fd_{crit}$ can provide more data.

The analytical model describes the frequency of the free surface oscillation qualitatively well, but some simplifications had to be taken into account. Hence there is scope for improvements. First of all the determination and investigation regarding the different torque coefficients depending on the runner design would be very interesting. An extension of the equation, estimating the angular frequency ω of the relative motion for conical tanks may be useful.

Next task for future investigations is the numerical simulation of the free surface oscillation investigated in the course of this thesis. Actually no literature dealing with this issue can be found. Data acquired by the present thesis can be used for validation. Based on this, the base flow, the propagation of free surface oscillation and the prediction of the flow phenomenon may be final goals.

An investigation of the water droplets and spray unsnapping from the water surface is another scientific challenge for the future. The amount of water sucked into the runner and its effects are quite unexplored.

Of course the acquired data can be extended to higher densimetric Froude number, different water levels and other model machines as well as different draft tube geometries.

Finally, another task could be the investigation and comparison of mechanism or practicable changes in design in order to prevent the excitation or rising of a free surface oscillation.

Bibliography

[1] Abramowitz G. L. and Segun I. A. Handbook of Mathematical Functions. Dover Publications, New York, 1968.

[2] Adunka F. Messunsicherheiten: Theorie und Praxis. Vulkan-Verlag, Essen, 3 edition, 2007.

[3] Albring W. Angewandte Strömungslehre. Theodor Steinkopf, Dresden, 4 edition, 1970.

[4] Andersson G., Donalek P., Farmer R., Hatziargyriou N., Kamwa I., Kundur P., Martins N., Paserba J., Pourbeik P., Sanchez-Gasca J., Schulz R., Stankovic A., Taylor C., and Vittal V. Causes of the 2003 major grid blackouts in North America and Europe, and recommended means to improve system dynamic performance. IEEE Transactions on Power Systems, (20):1922–1928, 2005.

[5] Austrian Power Grid AG. Netzentwicklungsplan 2018 für das Übertragungsnetz der Austrian Power Grid AG (APG) Planungszeitraum 2019 - 2028.

[6] Bauer H. F. Tables and graphs of zero of cross product Bessel functions. Mathematics of Computation, 1964(18):128–135.

[7] Berizzi A. The Italian 2003 blackout. In IEEE Power Engineering Society General Meeting, pages 1673–1679, 2004.

[8] Bhatt N. B. August 14, 2003 U.S.-Canada blackout, 2004.

[9] Bohl W. Technische Strömungslehre: Stoffeigenschaften von Flüssigkeiten und Gasen, Hydrostatik, Aerostatik, Inkompressible Strömungen, Kompressible Strömungen, Strömungsmeßtechnik. Kamprath-Reihe Technik. Vogel-Buchverlag, Würzburg, 5 edition, 1982.

[10] Ceravola O., Fanelli M., and Lazzaro B. The behaviour of the free level below the runner of Francis turbines and pump-turbines in operation as synchronous condenser. In IAHR Symposium, pages 765–775, 1980.

[11] Childs P. R. N. Rotating Flow. Butterworth-Heinemann, 2011.

BIBLIOGRAPHY

[12] Corsi S. and Sabelli C. General blackout in Italy Sunday September 28, 2003, h. 03:28:00. In IEEE Power Engineering Society General Meeting, pages 1691–1702, 2004.

[13] Daily J. W. and Nece R. E. Chamber Dimension Effects on Induced Flow and Frictional Resistance of Enclosed Rotating Disks. Journal of Basic Engineering, 1960:217–230.

[14] Deutsches Institut für Normen. DIN 1319-1: Grundlagen der Messtechnik-Grundbegriffe, 1995.

[15] Deutsches Institut für Normen. DIN 1319-3: Grundlagen der Messtechnik-Auswertung von Messungen einer einzelnen Messgröße Messunsicherheit, 1996.

[16] Deutsches Institut für Normen. DIN 1319-4: Grundlagen der Messtechnik-Auswertung von Messungen Messunsicherheit, 1999.

[17] Edinger G. Experimentelle Untersuchungen zum tiefen Teillastbetrieb von Pumpturbinen. Doctoral thesis, TU Wien, Vienna, Austria, 2014.

[18] Eichhorn M. Fatigue Analysis of Prototype Francis Turbines Using Numerical Simulations and Site Measurements. Doctoral thesis, TU Wien, Vienna, Austria, 2017.

[19] Eswaran M. and Saha Ujjwal K. Sloshing of liquids in partially filled tanks – a review of experimental investigations. Ocean Systems Engineering, (1):131–155.

[20] European Commission. Energy roadmap 2050.

[21] Gavrilyuk I. P., Lukovsky I. A., and Timokha A. N. Linear and nonlinear sloshing in a circular conical tank. Fluid Dynamics Research, 2005(37):399–429.

[22] Gers J. et al and Working Group J13. Modeling of Generator Controls for Coordinating Generator Relays: Special Report.

[23] Gieseke J., Heimerl St., and Mosonyi E. Wasserkraftanlagen - Planung, Bau und Betrieb. Springer Vieweg, 6 edition, 2014.

[24] Greitzer E. M., Tan C. S., and Graf M. B. Internal Flow: Concepts and Applications. Cambridge University Press, Cambridge, 2004.

[25] Hendry M. L. and McGough J. C. Synchronous Condensing Using the Generator of Peak Load Plant. In ASME - American Society of Mechanical Engineering, editor, Turbo Expo: Power for Land, Sea, and Air, 1995.

[26] Ibrahim R. A. Liquid Sloshing Dynamics. Cambridge University Press, Cambridge, 2005.

[27] International Electrotechnical Commission. IEC 60193: Hydraulic turbines, storage pumps and pump-turbines – Model acceptance tests, 1999.

[28] International Energy Agency. World Energy Outlook 2018 - Executive Summary.

[29] International Energy Agency. Statistics data browser, 2019.

[30] Kuschel M. and Seume J. Influence of Unsteady Turbine Flow on the Performance of an Exhaust Diffuser. Proceedings of the ASME Turbo Expo, 2011(7), 2011.

[31] Lamb H. Hydrodynamics. Dover Publications, New York, 6 edition, 1932.

[32] Lenarcic M. Investigation of S-shape instabilities in reversible pump-turbines and systematic development of countermeasures. Doctoral thesis, TU Wien, Vienna, Austria, 2016.

[33] Quantz L. and Meerwarth K. Wasserkraftmaschinen, Eine Einführung in Wesen, Bau und Berechnung von Wasserkraftmaschinen und Wasserkraftanlagen. Springer Vieweg, 1963.

[34] Raabe J. Hydraulische Maschinen und Anlagen. VDI - Verlag, Düsseldorf, 2 edition, 1989.

[35] Royon-Lebeaud A., Hopfinger E. J., and Cartellier A. Liquid sloshing and wave breaking in circular and square-base cylindrical containers. Journal of Fluid Mechanics, 2007(577):467–494.

[36] Ruppert L. Pumped-storage implementation in order to balance volatile renewable energy generation. Doctoral thesis, TU Wien, Vienna, Austria, 2017.

[37] Rychkov S. I. Reactive power control services based on a generator operating as a synchronous condenser. Power Technology and Engineering, (46):405–409, 2013.

[38] Schlichting H. G. Grenzschichttheorie. G. Braun, 5 edition, 1965.

[39] Sigloch H. Technische Fluidmechanik. Springer Vieweg, 9 edition, 2014.

[40] Smirnov A. M. "High"-pressure air system for converting units to a synchronous capacitor regime. Hydrotechnical Construction, (17):113–120, 1983.

[41] Smirnov A. M. and Ustalov V. A. Conversion of turbogenerator units to synchronous condenser regime. Énergiya, Moscow, 1974.

[42] Smirnov A. M. and Ustalov V. A. Expulsion of water from the turbine runner on switching a turbo-generator to a synchronous condenser regime. Hydrotechnical Construction, (8):241–246, 1974.

[43] Sommerfeld A. Mechanik der deformierbaren Medien. Akademische Verlags-gesellschaft Becker & Erler, Leipzig, 1945.

[44] Song Y. K., Chang K.-A., Ryu Y., and Kwon S. H. Experimental study on flow kinematics and impact pressure in liquid sloshing. Experiments in Fluids, 2013.

[45] Steinrück H. and Maly A. Experimental and asymptotic investigation of a rotary wave in a cylindrical container. In 88th Meeting of the International Association of Applied Mathematics and Mechanics, pages 667–668, 2017.

[46] Steinrück H. and Maly A. The growth of a rotary gravity wave in a cylindrical container. In 20th International Seminar on Hydropower Plants, pages 775–788, 2018.

[47] Tanaka H., Matsumoto K., and Yamamoto K. Sloshing motion of the de-pressed water in the draft tube in dewatered operation of high head pump-turbines. In XVII IAHR Symposium, pages 121–130, 1994.

[48] Tanaka H. and Toshiba Cooperation. Some technical review and advanced technologies based on operating experiences of high head pump-turbines. In Beijing 89 Symposium: International Symposium on Large Hydraulic Machinery & Associated Equipments, pages 410–421, 1989.

[49] Taylor G. An Experimental Study of Standing Waves. Proceedings of the Royal Society of London. Series A, Mathematical and Physical Sciences, 1953(218):44–59.

[50] Transmission System Operators of AT BE CH DE FR LU NL. 2nd Report on generation adequacy assessment within PLEF region.

[51] UCTE - Union for the Co-ordination of Transmission of Electricity. Final Report of the Investigation Committee on the 28 September 2003 Blackout in Italy.

[52] U.S.-Canada Power System Outage Task Force. Final Report on the August 14, 2003 Blackout in the United States and Canada: Causes and Recommen-dations.

[53] Vagnoni E. Two-phase flow phenomena in hydraulic turbines and pump-turbines operating in synchronous condenser mode. Doctoral thesis, Ecole Polytechnique Federale de Lausanne, Lausanne, Switzerland, 2018.

[54] Vagnoni E., Andolfatto L., and Avellan F. On the sloshing free surface in the draft tube cone of a Francis turbine operating in synchronous condenser mode: IOP Publishing. Journal of Physics - Conf. Series, (813:012034), 2017.

[55] Vagnoni E., Andolfatto L., Guillaume R., Leroy P., and Avellan F. Air-Water Ring in the Vaneless Gap of a Reversible Pump-Turbine Operating in Condenser Mode. In ASME Press, editor, Proceedings of the 10th International Symposium on Cavitation (CAV2018), 2018.

[56] Vagnoni E., Andolfatto L., Guillaume R., Leroy P., and Avellan F. Rotating air-water ring in the vaneless gap of a pump-turbine operating in condenser mode. International Journal of Multiphase Flow, (105):112–121, 2018.

[57] Vagnoni E., Arthur F., Andolfatto L., and Avellan F. Experimental investigation of the sloshing motion of the water free surface in the draft tube of a Francis turbine operating in synchronous condenser mode. Experiments in Fluids, (59:95), 2018.

[58] Valentine D. T. and Frandsen J. B. Nonlinear Free-Surface and Viscous-Internal Sloshing. Journal of Offshore Mechanics and Arctic Engineering, 2005(127):141–149.

[59] Valentín D., Presas A., Valero C., Egusquiza M., and Egusquiza E. Synchronous condenser operation in francis turbines: Effects in the runner stress and machine vibration. Renewable Energy, 146:890 – 900, 2019.

[60] Verein Deutscher Ingenieure VDI-Gesellschaft Verfahrenstechnik und Chemieingenieurwesen. VDI-Wärmeatlas. Springer Vieweg, Berlin Heidelberg, 11 edition.

[61] Yang W., Chergui J., Fraigneau Y., Delbende I., and Witkowski L. M. Free surface flow driven by a rotating end wall in a stationary cylinder: Structure of the axisymmetric baseflow. In 23ème Congrès Français de Mécanique 2017. 2017.

[62] Yang W., Delbende I., Fraigneau Y., and Witkowski L. M. Axisymmetric rotating with free surface in a cylindrical tank. Journal of Fluid Mechanics, (861):796–814, 2019.

[63] Zanetti V. and Rossi G. Synchronous condenser operation and running up in air of a medium characteristic speed pump-turbine: model tests. In IX IAHR Joint symposium on design and operation of fluid machinery, pages 337–352, 1978.